UNIVERSITAT DE BARCELONA

Paper-based bateries as key enablers for self-powered conductivity sensing

Laura Ortega Tañá

ADVERTIMENT. La consulta d'aquesta tesi queda condicionada a l'acceptació de les següents condicions d'ús: La difusió d'aquesta tesi per mitjà del servei TDX (**www.tdx.cat**) i a través del Dipòsit Digital de la UB (**diposit.ub.edu**) ha estat autoritzada pels titulars dels drets de propietat intel·lectual únicament per a usos privats emmarcats en activitats d'investigació i docència. No s'autoritza la seva reproducció amb finalitats de lucre ni la seva difusió i posada a disposició des d'un lloc aliè al servei TDX ni al Dipòsit Digital de la UB. No s'autoritza la presentació del seu contingut en una finestra o marc aliè a TDX o al Dipòsit Digital de la UB (framing). Aquesta reserva de drets afecta tant al resum de presentació de la tesi com als seus continguts. En la utilització o cita de parts de la tesi és obligat indicar el nom de la persona autora.

ADVERTENCIA. La consulta de esta tesis queda condicionada a la aceptación de las siguientes condiciones de uso: La difusión de esta tesis por medio del servicio TDR (**www.tdx.cat**) y a través del Repositorio Digital de la UB (**diposit.ub.edu**) ha sido autorizada por los titulares de los derechos de propiedad intelectual únicamente para usos privados enmarcados en actividades de investigación y docencia. No se autoriza su reproducción con finalidades de lucro ni su difusión y puesta a disposición desde un sitio ajeno al servicio TDR o al Repositorio Digital de la UB. No se autoriza la presentación de su contenido en una ventana o marco ajeno a TDR o al Repositorio Digital de la UB (framing). Esta reserva de derechos afecta tanto al resumen de presentación de la tesis como a sus contenidos. En la utilización o cita de partes de la tesis es obligado indicar el nombre de la persona autora.

WARNING. On having consulted this thesis you're accepting the following use conditions: Spreading this thesis by the TDX (**www.tdx.cat**) service and by the UB Digital Repository (**diposit.ub.edu**) has been authorized by the titular of the intellectual property rights only for private uses placed in investigation and teaching activities. Reproduction with lucrative aims is not authorized nor its spreading and availability from a site foreign to the TDX service or to the UB Digital Repository. Introducing its content in a window or frame foreign to the TDX service or to the UB Digital Repository is not authorized (framing). Those rights affect to the presentation summary of the thesis as well as to its contents. In the using or citation of parts of the thesis it's obliged to indicate the name of the author.

Tesi doctoral

Paper-based batteries as key enablers for self-powered conductivity sensing

Autora: Laura Ortega Tañá

Directors: Neus Sabaté Vizcarra
Juan Pablo Esquivel Bojórquez

UNIVERSITAT DE BARCELONA

Paper-based bateries as key enablers for self-powered conductivity sensing

Programa de doctorat en Enginyeria i Ciències Aplicades

Autora: Laura Ortega Tañá

Directors: Neus Sabaté Vizcarra

Juan Pablo Esquivel Bojórquez

Tutor: Pere Lluís Miribel Català

Institut de Microelectrònica de Barcelona (IMB-CNM, CSIC)

LAURA ORTEGA TAÑÁ - DNI 53298818K

Firmado digitalmente por LAURA ORTEGA TAÑÁ - DNI 53298818K
Fecha: 2021.02.14 21:41:26 +01'00'

UNIVERSITAT DE BARCELONA

ICREA Professor Neus Sabaté Vizcarra and Dr. Juan Pablo Esquivel Bojórquez at the Institute of Microelectronics of Barcelona IMB-CNM (CSIC), certify that the thesis entitled: "*Paper-based batteries as key enablers for self-powered conductivity sensing*" was carried out under their supervision within IMB-CNM.

In witness whereof for the Department of Electronic and Biomedical Engineering of University of Barcelona, they herby sign this present certification.

Bellaterra, November 2020

ICREA Professor Neus Sabaté Vizcarra

(Director)

SABATE VIZCARRA NEUS - 39726249M

Firmado digitalmente por SABATE VIZCARRA NEUS - 39726249M
Fecha: 2021.02.15 08:31:47 +01'00'

Dr. Juan Pablo Esquivel Bojórquez

(Director)

ESQUIVEL BOJORQUEZ JUAN PABLO - DNI X7260006X

Firmado digitalmente por ESQUIVEL BOJORQUEZ JUAN PABLO - DNI X7260006X
Fecha: 2021.02.15 10:26:45 +01'00'

Dr. Pere Lluís Miribel Català

(Tutor)

PEDRO LUIS MIRIBEL CATALA - DNI 38835188x

Firmado digitalmente por PEDRO LUIS MIRIBEL CATALA - DNI 38835188x
Fecha: 2021.02.15 15:45:43 +01'00'

A mis padres
y a mis Avis

Agradecimientos

Primero de todo, me gustaría agradecer todo el apoyo recibido durante estos últimos años a todas aquellas personas que han formado parte de este largo viaje.

En especial a mi directora de tesis Neus Sabaté, que, aparte de enseñarme qué es la ciencia, siempre me ha apoyado, tanto en mi desarrollo personal como profesional, confiando en mí y ofreciéndome infinitas oportunidades de crecimiento. También a Juan Pablo Esquivel, quien me ha enseñado que el continente es igual de importante que el contenido.

También a Pere, Jordi e Ivón, unos profesores que se convirtieron en amigos, que me bridaron la oportunidad de empezar mi etapa investigadora y sin los que no sería la persona que soy ahora.

A mis amigos del IMB, Javi, Amparo, Sergi, Mar, Dmitry, Mireia, Meritxell, Josune, Augusto, Gonzalo con los que he compartido horas de café, cervezas y risas. A mi grupo, SPEED, con el que he pasado penas de laboratorio, pero también muchas alegrías. A mis últimas estudiantes, Núria Rueda y Cèlia Vicens, que, con su trabajo, esfuerzo y proactividad me han ayudado a acabar la tesis. A Anna, que se ha convertido en una de mis mejores amigas, con la que he compartido tantas cosas que se ha convertido en mi grupo burbuja y espero que siga a mi lado por muchos años porque, juntas, todo es posible.

Por último, mi agradecimiento más especial es para mi familia. A mis padres, que siempre me han apoyado, inculcándome con cariño el esfuerzo y la perseverancia. A mis hermanas, con las que siempre he podido contar para todo. Y por supuesto para Marcos, mi otra mitad, por hacerme más fácil este camino, aguantándome largos fines de semana trabajando, ofreciéndome una sonrisa, una broma un consejo o un abrazo cuando lo necesitaba.

Contents

INTRODUCTION **1**
Digitalization of ASSURED devices 2
Key enablers of Digital ASSURED devices 3
Self-powered electrochemical sensors as key enablers of future Digital ASSURED devices 6
Summary 11
References 13
BASICS OF THE CONDUCTIVITY PAPER BATTERY-SENSOR **19**
Overview 19
Introduction 20
Results and discussion 25
Battery performance and characterization 25
Paper-battery as self-powered conductivity sensor 27
Conclusions 40
References 42
CONDUCTIVITY APPLICATION 1: DEVELOPMENT OF A SELF-POWERED SCALE-BAR CONDUCTOMETER **45**
Overview 45
Introduction 46
Results and discussion 48
Battery stack sensing capabilities 48
Circuit design, implementation and characterization 54
Conductometer fabrication and validation 61
Conclusions 66
References 67

CONDUCTIVITY APPLICATION 2: DEVELOPMENT OF A SELF-POWERED SKIN PATCH FOR THE SCREENING OF CYSTIC FIBROSIS **69**

Overview 69

Introduction 70

Results and discussion 73

Device design and operation 73

Calibration of battery-sensor for cystic fibrosis screening application 74

Electronic circuit design and characterization 79

Self-powered sweat patch fabrication 82

Self-powered sweat patch performance validation 84

Outlook: pre-clinical testing 89

Conclusions 90

References 91

CONDUCTIVITY APPLICATION 3: IMPLEMENTATION OF A SINGLE USE DEHYDRATION MONITOR FOR ATHLETES **93**

Overview 93

Introduction 94

Results and discussion 95

Sweat absorbent patch design, implementation and calibration 95

Sweat absorbent patch testing in a relevant environment 102

Self-powered sweat sensor, study of two different designs to maximize the device performance 108

Testing of the self-powered sensor with artificial eccrine perspiration and real sweat 116

Conclusions 123

References 124

CONCLUSIONS **129**

SCIENTIFIC CONTRIBUTIONS **131**

Journal articles 131

Patent 131

Workshops and Conferences 131

SUMMARY **133**

RESUMEN **135**

ANNEX 1: Approval of the Clinical Research Ethics Committee (CEIm) of Sant Joan de Déu Hospital **137**

ANNEX 2: Approval of the *Agencia Española del Medicamento y Productos Sanitarios* (AEMPS) **141**

ANNEX 3: Approval of the Ethics Committee of the *Consejo Superior de Investigaciones Científicas* (CSIC) **145**

ANNEX 4: Informed consent for sample donation and participation in an investigation **149**

1.

INTRODUCTION

The traditional definition of Point of Care devices (PoC) consists of bringing the technology necessary for medical care close to the patient, entailing a wide variety of services and techniques that range from vital signs monitoring to on-site laboratory testing. PoC devices offer the opportunity to perform a more decentralized diagnostic analysis, providing significant advantages such as portability, automation and fast diagnostic results at reduced cost. These benefits suggest that PoC devices could have a decisive impact in resource-limited regions where the access to quality medical care is a challenge[1].

With the aim of providing portable solutions to perform laboratory analysis, the arrival of micro Total Analysis Systems (µTAS) or Lab-on-Chip (LoC) devices[2] in the 1990's opened the opportunity to develop portable diagnostic devices with superior capabilities that would allow to overcome the limitations of traditional lateral flow immunochromatographic test strips.

These LoC devices have been under study and development for the last 30 years, presenting different advantages in comparison to the traditional laboratory testing, such as small sample and reagent quantity to perform the test, smart capabilities as separation and detection with high resolution and sensitivity at short times. However, these LoC devices present three main drawbacks that hinder their wide adoption in consumer applications, such as difficulty in the fabrication processes, the requirement to be used in combination with costly peripherals and the need of specific training for their operation. These particular aspects have limited their applicability to large laboratories, operated by skilled technical specialists in the form of cartridges to be inserted in larger analysers, such as CHEM8+ or EG6+ cartridges of the i-STAT from Abbott, shown in Figure 1.

In parallel to the LoC research, lateral flow-based devices entered the market in the 1970's with the pregnancy test. Traditionally, these single-use tests aimed to perform a qualitative detection of an antigen-antibody interaction and provide a result to the user with a single

Figure 1. CHEM8+ and EG6+ cartridges from Abbott[3].

or a double colour line, indicating a negative or a positive result[4]. Their simplicity and affordability when compared to the complex LoC alternatives have originated a wide adoption of lateral flow tests in many areas that range from woman health, drugs of abuse, and cardiac biomarkers to infectious diseases. These devices can perform a rapid test in places where there are no clinical capabilities and provide a rapid result that allows for easy interpretation with the appropriate instructions of use. Despite their evident advantages, these devices present also limitations that are susceptible to human error. These constraints include the necessity of adding a primary or even a secondary buffer to perform the antigen-antibody linking process, the subjective interpretation of results due to the low sensitivity of these lateral flow colorimetric-based assays under visual inspection which provide a non-clear visualization of the control and test lines indicators, or the lack of time control when performing time-dependent measurements[5,6].

With the objective of unifying criteria and setting the features required from a point-of-care test to ensure a successful deployment, the World Health Organization (WHO) defined the guidelines for the development of diagnostics for rapid tests as ASSURED[7] (Affordable, Sensitive, Specific, User-friendly, Rapid and Robust, Equipment-free and Delivered to those who need it). The obtaining of these ASSURED devices, would allow an earlier disease diagnosis, patient stratification and/or prognosis of diseases leading to improved clinical decisions and health outcomes that contribute to the sustainability of the healthcare system both in first-world countries and in resource-limited settings.

Digitalization of ASSURED devices

In addition to the desirable features of ASSURED devices, the scientific community has been making efforts to achieve the digitalization of ASSURED devices that can help to

remove ambiguities in the interpretation of the result and at the same time, unfold the possibility of data tracking and analysis at large scales. Different strategies have been followed to achieve this objective[8]: i) the use of handheld or small benchtop instrumentation, ii) the employment of smartphones as colorimetric readers[9] and iii) the incorporation of dedicated electronic modules to perform the optical measurement and display of results to the user. The use of smartphones as optical readers seems to be the most straightforward and cost-effective solution. For this reason, several companies are nowadays focused on solving the uncertainties introduced by the influence of ambient light, the image capture distance and orientation, and the variability introduced by the particular properties of the phone camera. Besides, the introduction of dedicated electronic components in a rapid test eliminates the current uncertainty provided by the colorimetric assays. However, it increases the complexity of fabrication and cost per test, which turns to be particularly acute in single-use applications. They also require the integration of a power source, which needs to be handled properly and potentially increases the environmental impact of the device.

Key enablers of Digital ASSURED devices

In order to solve the previously mentioned issues, three main technological drivers have been identified as enablers of digital ASSURED devices, i.e. printed electronics, paper microfluidics and self-powering, as shown in Figure 2.

The first technological driver, printed electronics, aims to solve the complexity of fabrication of ASSURED digital devices. Printed electronics offer different advantages compared to

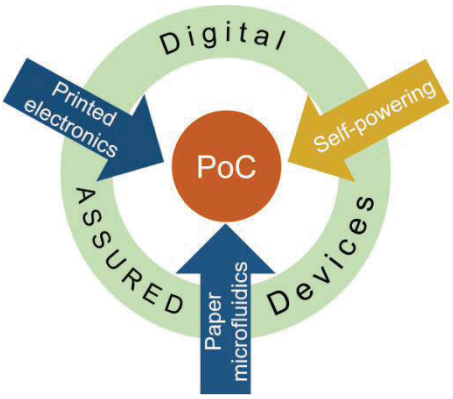

Figure 2. Technological drivers for the development of digital ASSURED devices.

traditional silicon electronics, such as fast on-demand production, fabrication at room temperatures and large area production. Due to its additive nature, it permits the fabrication of structures in a continuous manner. This technology provides the opportunity to develop fast prototypes that can be easily scalable to large production with roll-to-roll (R2R) processes (Figure 3). These techniques simplify radically the manufacturing process with very high process speeds[10]. Two of the most used printed electronic techniques are inkjet printing and screen-printing. Inkjet printing allows the deposition of conductive inks in the form of small droplets through a micrometre nozzle head. This technique allows obtaining elements of 10 μm but the speed production is low compared to other printed electronic techniques as screen-printed or gravure[11]. It is the perfect printed technique for prototyping small volumes of devices and when the production is necessary to be higher it can be easily transferred to high volume techniques as screen-printing.

Screen-printing is the most widely used technique to manufacture printed electronic components. This method relies on the deposition of a thin film of a conductive or insulating paste with a controlled pattern defined in a mesh, which defines the object to be transferred and its thickness. This method is a very mature printing technology; it is very compatible with different substrates such as paper, plastic or textile and can achieve resolutions of 100 μm[12]. Due to its versatility and scalability it has been integrated in R2R machines offering high-volume and large-scale productions.

Due to its additive nature, the development of printed electronic products has been typically related to the implementation of flexible electronics, which have enabled the production of new products in industries such as automotive, packaging, IoT, healthcare

Figure 3. Roll-to-roll machine from Techprint Inc for screen-printing and lamination[13].

and wellbeing, consumer electronics and smart buildings. Specifically in healthcare and wellbeing there is a lot of research done regarding the implementation of printed sensors for health monitoring by using high throughput techniques as gravure or screen printing for measuring sweat ion composition[14], pulse rate[15,16] or respiratory monitoring[17]. Apart from sensors, printed electronics have been used to manufacture electronic components like resistors[18], diodes[19], capacitors[20] or transistors[21]. Although organic printed electronic components entail a promising future, in terms of performance there is still much to do in order to reach the reliability and tolerances achieved by traditional silicon electronic components.

The second technological driver to be considered in the development of ASSURED digital devices is paper microfluidics. With the lateral flow-based devices, the paper matrices have been proven as very suitable substrates to analyse biological samples. Paper microfluidics provide a suitable solution to perform more complex sample analysis. This technological driver allows distributing the sample into multiple regions that enable multiplexing assays on a single device, move the sample by capillarity removing the need of pumps, require small volumes of sample and the elimination of hazardous waste becomes simple as can be disposed by incineration. During the last ten years, many works have reported different devices where microchannels were patterned onto paper matrices using wax printing[22], CO_2 laser cut[23] or flexographic printing of polystyrene[24] among others. By folding these two-dimensional microchannels, three-dimensional paper-based microfluidic devices can also be obtained[21]. In addition, inside the cavities defined by the patterned channels different capabilities can be introduced, such as mixing or heating the sample, as well as reading or transmitting the results to an external device[25–27].

Due to its versatility, paper can be also used as the matrix to perform quantitative electrochemical measurements. Electrodes can be patterned using printed electronic methods such as screen-printing or inkjet printing (first driver) over a patterned paper-based matrix (second driver) to implement paper based electrochemical devices. Electrochemical paper-based analytical devices have the benefit of providing more stable and quantifiable result than colorimetric devices. They usually present high sensitivity and selectivity by modifying the sensing electrodes with biorecognition elements, enzymes and nanomaterials, among others[28]. Traditionally, these electrochemical paper-based analytical devices have been connected to a potentiostat enabling the quantification of analytes by means of amperometry, voltammetry, potentiometry, electrochemical impedance and capacitance[29]. Even though potentiostats have been miniaturized and implemented in single-use devices, it is a fact that the need of a detection instrument

increases the complexity and cost per test, which limits the accessibility of these devices for single-use applications[30]. Furthermore, there are some unsolved challenges to achieve fully functional systems, such as system integration, data management and power autonomy. To solve this last challenge, the integration of electrochemical power sources, like fuel cells or paper-based batteries, together with paper-based electrochemical devices can provide a viable solution to finally achieve fully functional autonomous devices. With this concept the third technological driver to develop digital ASSURED devices is introduced: the self-powered sensing approach.

Self-powered electrochemical sensors as key enablers of future Digital ASSURED devices

One of the sustainability principles of circular economy is the reduction of materials to minimize waste. In diagnostics, this translates into an efficient use of materials and the minimization of the number of electronic components (i.e.*minimal electronics* approach) as the most optimal pathway to decrease the environmental impact of the single-use point-of-care devices, while providing the required functionalities to make them fully functional. One key step to minimize the electronic elements of a portable sensing system is offered by the implementation of self-powered strategies. Self-powered devices consist on power sources that interact with a specific physical or chemical parameter and whose power performance is directly related to the intensity or the amount of said parameter. In this way, the power source becomes a sensor and thus, both elements merge into a single one and allow reducing the number of components of the overall system while rendering it energetically autonomous. In particular, electrochemical power sources have proven to be promising candidates to implement self-powered electrochemical sensors. Specifically, fuel cells – that generate electrical energy from the oxidation of chemical compounds – have arisen as self-powered sensors of chemical analytes. Fuel cells were first reported in 1802, when Humphry Davy described a rudimental fuel cell constructed by using a carbon fuel in the anodic compartment and aqueous nitric acid as reactant in the cathodic compartment[31]. After more than a century of research, fuel cells have reached maturity as power supplies for both stationary and transportation applications being the main fuel methanol or hydrogen. However, the quest of sustainable alternatives to these main chemical energy sources led to the exploration of ubiquitous fuels, such as glucose, and the appearance of the so-called biofuel cells, in which enzymes substituted metal-based catalysts to oxidize biomolecules (like glucose or ethanol). The development of this kind of fuel cells[32,33] has been particularly intense since the turn of the 21st century, as it promises

on one side, electrical power generation from an abundant organic molecules and on the other, the availability of a continuous power supply for implantable devices. Nevertheless, the reliability and stability of enzymes over time has hindered so far the applicability of biofuel cells as power sources in real-case scenarios. In the last years, biofuel cells have found a promising arena as self-powered sensing devices and, several works that use either direct or mediated electron transfer electrocatalysis to generate an amount of power directly related with the amount of analyte present in the fuel solution have been presented[34–39]. In these studies, glucose, ethylenediaminetetraacetic acid (EDTA), ethanol, lactate and cholesterol are used as fuel for self-quantification. Most of the reports show the relationship of the power generated by the biofuel cell and the analyte concentrations of the feeding fuel to demonstrate the self-powered concept. On the way to standalone self-powered devices, different works present the implementation of systems where the self-quantification of the fuel is performed but the power output provided (which if directly related to the concentration of the fuel) is read by an external apparatus that requires its own external power supply. This approach has been followed in many different works where voltage[40], current[40] or frequency[41] demonstrated to be directly proportional to the fuel concentration. An interesting example was developed by Choi et. al. in 2017, who presented a biofuel cell to measure sweat glucose concentration following a minimal electronics approach. By using a single resistive load and a handheld multimeter the resultant output current was shown to be directly proportional to the glucose concentration[42].However, none of the cited examples attains to power a standalone electronic device and in the end, only the amount of power directly related with the fuel concentration is reported. One of the main challenges to be overcome when designing a standalone system capable to quantify the energy provided by a biofuel cell is that traditional silicon electronics require a positive voltage larger than 0.4 V to operate and operational potentials of such fuel cells are typically lower[33]. To solve this problem, some recent approaches have explored the integration of voltage boosters to increase the voltage provided by the fuel cell to values able to be managed with a traditional electronic module[43,44]. Another interesting solution presented in the literature is the introduction of a charge pump in combination with a capacitor and the sensing fuel cell to achieve high voltages with sufficient transient currents to operate an electronic device[45,46].

As already mentioned, due to the low power outputs of biofuel cells, the first approach for the obtaining digital ASSURED and energetically autonomous devices is use the fuel cells to extract the energy from the sample to power an electronic circuit that quantifies an analyte of that same sample by means of an additional biosensor. The first work following this approach was Atanassov et.al.[47], in which a glucose biofuel cell is used to obtain the

energy required to power a lactate biosensor. This strategy allowed to use high concentration of glucose fuel to produce enough power to measure much lower concentrations of lactate measured by the biosensors. In this case, the system required a potentiostat circuit to drive the measurement. With a similar approach in 2018 a self-powered electronic reader analytical device was developed by Esquivel et al. In this case a disposable test strip containing a paper-based battery and a glucose biofuel cell were used to obtain the power required to drive the electronic circuit and to measure the glucose concentration respectively[48]. In this paper, despite the quantification of glucose was performed with energy provided by the auxiliary paper-based battery; the sustainable approach of the reader is remarkable. With a similar approach, Sabaté et al. developed in 2020 an autonomous system, which powered an HIV-1 EGOFET (electrolyte-gated field-effect transistor) by the energy generated from the glucose of a drop of blood[49]. This work demonstrated the feasibility of powering minimal electronic circuits for the detection of HIV-1 in the fM range. Finally, Rogers et.al, developed an autonomous system which used a sweat-activated primary battery to power a flexible device which incorporated a heart rate monitor, sweat chloride sensor and a pH sensor[3].

The final implementation of truly self-powered digital ASSURED devices has been achieved by the use of the same biofuel cells as both power source and sensor and performing analyte quantification and results display to the user. Wang et al. developed in 2016 stretchable glucose and lactate biofuel cells able to produce power from sweat when performing physical activity. The biofuel cells were fabricated by screen-printing with stretchable printed electrodes and integrated in a sock. This device was capable to produce an amount of power directly related with the amount of sweat lactate and glucose selectively and the result was shown to the user by few different light emitting diodes (LEDs) integrated in the sock[50]. The same group also developed a high-power density biofuel cell, which also used lactate as fuel to power a LED and a Bluetooth Low Energy (BLE) radio. By using screen-printed three-dimensional carbon-nanotube-based bioanode and a metallic cathode array arranged in an “island-bridge” configuration combined with a DC-DC converter and a 2.2 mF capacitor the powering of the BLE was achieved. With this skin-based device, they demonstrated the feasibility of combining printed electronic techniques and the approach of using a limited number of electronic components to develop self-powered devices[51]. With a similar approach, in 2019 another carbon-based lactate biofuel cell was implemented. In this case, the lactate produced during exercise was being monitored by oxidising it in the anode and an air-breathing cathode allowed the reduction of oxygen and the final evaporation of the sweat already measured. The generated power was first being displayed by a blinking LED and also stored inside a

capacitor and when the capacitor was sufficiently charged, the information was sent wirelessly to a receiver without the need of an additional power source. In this case, the output voltage of a single device produced voltages up to 0.16 V, so to drive the wireless transmitter different lactate biofuel cells had to be connected in series to attain the required output voltage for data transmission. The paper showed that an intensive biking activity of 60 minutes allowed to charge the capacitor to send a single lactate measurement[52]. Although many promising seed works have been reported to date, electrochemical self-powered devices are still far from fulfilling a practical application. Challenges regarding reliability and robustness must be solved in order to produce solutions that lead to the effective deployment of self-powered digital ASSURED devices.

Summary

This thesis introduces paper-based batteries as a new kind of self-powered electrochemical sensor that allows quantification of ionic conductivity of liquid samples. Particularly, this work explores the main features of this new approach and shows its capabilities to develop truly operative digital ASSURED devices in three different practical applications where a single use PoC device allowing for conductivity is of high interest.

The development of the prototypes presented here make use of the three main technological drivers - printed electronics, paper microfluidics and self-powering strategies – and go a step further using manufacturing processes that can be easily scaled up. The presented devices have been manufactured using rapid prototyping and low cost techniques such as laser cutting, screen-printing, inkjet printing and lamination of substrates. At the same time, the implementation of engineering strategies that follow the minimal electronics approach to minimize both cost and environmental impact in the disposability of the devices has been intensively assessed. In addition, due to its purpose to be used in real environments, robustness and reliability have been key features that have been taken into account in the implemented devices. The work is organized in five chapters: the current introductory chapter, a second chapter that sets the basis of the new self-powered sensor and three additional chapters in which operative devices for particular applications are designed, fabricated and characterized, organized so that it increases in complexity and impact. Figure 4 shows a graphical representation of the thesis organization.

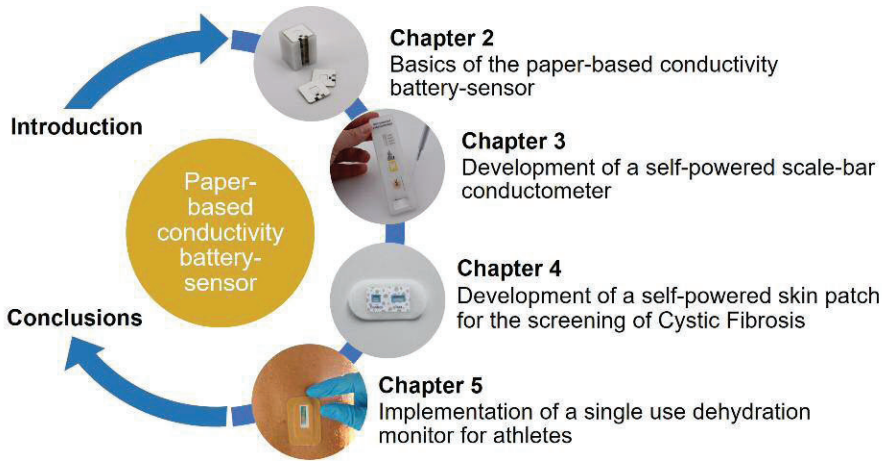

Figure 4. Graphical overview of the thesis contents.

After the current introductory chapter, the thesis starts by laying the fundamentals of the paper-based conductivity battery sensor that is the cornerstone of the self-powered devices developed in this thesis. An introduction to paper-based batteries is followed by detailed descriptions of the basic chemistry, materials and the fabrication process of a single battery unit. The sensing principle and the battery measuring range in a self-powered mode is explored.

The thesis follows with the realization of three different self-powered prototypes that make use of the battery to deliver a digital result of a conductivity measurement. In particular, the third chapter uses a stack of two paper-based conductivity battery-sensors to implement a self-powered scale-bar conductometer that is specifically designed to analyse water samples. The power output of the battery is discretized in four different levels that correspond to four relevant conductivity levels. The single use self-powered conductometer provides a visual output with a four-segment electrochromic display. Finally, real samples of tap water, lake water and sea water are used to validate the performance of the device.

In the fourth chapter, the fabrication and validation of a medical device aiming to screen Cystic Fibrosis disease is presented. In this case, the paper-based conductivity battery-sensor is integrated into a self-powered skin patch that measures sweat conductivity and detects whether a specific threshold value is surpassed. Again, in this chapter, the implementation of a stack of two paper-based batteries is required to turn on two different electrochromic displays showing a positive or a negative result to the user. The self-powered skin patch is finally validated using artificial eccrine perspiration samples. Lastly, an introduction of the first clinical trial performed with this device is presented.

The last chapter introduces the implementation of a self-powered skin patch to assess dehydration in athletes. This development aims to validate he hypothesis that sweat conductivity increases upon dehydration of individuals. The chapter presents sweat conductivity measurements of volunteers during a mountain race with a commercial impedimetric sensors that allowed to determine the expected conductivity ranges. Then, the battery paper core was optimized to maximize the linear output voltage in the range of interest. Finally, the optimized battery-sensor performance was validated using real sweat samples from volunteers submitted to a moderate intensity physical activity. Results were compared with a commercial portable conductometer, which validated the conductivity results performed by our paper-based conductivity battery-sensor.

References

(1) Choi, S. Powering Point-of-Care Diagnostic Devices. *Biotechnology Advances*. May 1, 2016, pp. 321–330. https://doi.org/10.1016/j.biotechadv.2015.11.004.

(2) Sia, S. K.; Kricka, L. J. Microfluidics and Point-of-Care Testing. *Lab on a Chip.* November 4, 2008, pp. 1982–1983. https://doi.org/10.1039/b817915h.

(3) Bandodkar, A. J.; Lee, S. P.; Huang, I.; Li, W.; Wang, S.; Su, C. J.; Jeang, W. J.; Hang, T.; Mehta, S.; Nyberg, N.; et al. Sweat-Activated Biocompatible Batteries for Epidermal Electronic and Microfluidic Systems. *Nature Electronics.* July 13, 2020, pp. 554–562. https://doi.org/10.1038/s41928-020-0443-7.

(4) Yetisen, A. K.; Akram, M. S.; Lowe, C. R. Paper-Based Microfluidic Point-of-Care Diagnostic Devices. *Lab on a Chip*. June 21, 2013, pp. 2210–2251. https://doi.org/10.1039/c3lc50169h.

(5) Pollock, N. R.; Rolland, J. P.; Kumar, S.; Beattie, P. D.; Jain, S.; Noubary, F.; Wong, V. L.; Pohlmann, R. A.; Ryan, U. S.; Whitesides, G. M. A Paper-Based Multiplexed Transaminase Test for Low-Cost, Point-of-Care Liver Function Testing. *Science Translational Medicine.* September 19, 2012, pp. 152ra129. https://doi.org/10.1126/scitranslmed.3003981.

(6) Han, K. N.; Choi, J. S.; Kwon, J. Three-Dimensional Paper-Based Slip Device for One-Step Point-of-Care Testing. *Scientific Report.* May 13, 2016. pp. 1-7. https://doi.org/10.1038/srep25710.

(7) Peeling, R. W.; Holmes, K. K.; Mabey, D.; Ronald, A. Rapid Tests for Sexually Transmitted Infections (STIs): The Way Forward. *Sexually Transmitted Infections*. December 6, 2006, pp. 1-6. https://doi.org/10.1136/sti.2006.024265.

(8) Vashist, S. K.; Luppa, P. B.; Yeo, L. Y.; Ozcan, A.; Luong, J. H. T. Emerging Technologies for Next-Generation Point-of-Care Testing. *Trends in Biotechnology*. November 1, 2015, pp. 692–705. https://doi.org/10.1016/j.tibtech.2015.09.001.

(9) Vashist, S. K.; Mudanyali, O.; Schneider, E. M.; Zengerle, R.; Ozcan, A. Cellphone-Based Devices for Bioanalytical Sciences Multiplex Platforms in Diagnostics and Bioanalytics. *Analytical and Bioanalytical Chemistry*. May 1, 2014. pp. 3263–3277. https://doi.org/10.1007/s00216-013-7473-1.

(10) Sreenilayam, S. P.; Ahad, I. U.; Nicolosi, V.; Acinas Garzon, V.; Brabazon, D.

Advanced Materials of Printed Wearables for Physiological Parameter Monitoring. *Materials Today*. January 1, 2020, pp. 147–177. https://doi.org/10.1016/j.mattod.2019.08.005.

(11) Khan, S.; Lorenzelli, L.; Dahiya, R. S. Technologies for Printing Sensors and Electronics over Large Flexible Substrates: A Review. *IEEE Sensors Journal.* December 4, 2014. pp. 3164–3185. https://doi.org/10.1109/JSEN.2014.2375203.

(12) Andersson Ersman, P.; Lassnig, R.; Strandberg, J.; Dyreklev, P. Flexible Active Matrix Addressed Displays Manufactured by Screen Printing. *Advanced Engineering Materials.* September 9, 2020. pp. 2000771 (1-7). https://doi.org/10.1002/adem.202000771.

(13) Printed Electronics | Techprint, Inc. https://www.techprintinc.com/product/printed-electronics/ (accessed Nov 2, 2020).

(14) Bariya, M.; Shahpar, Z.; Park, H.; Sun, J.; Jung, Y.; Gao, W.; Nyein, H. Y. Y.; Liaw, T. S.; Tai, L. C.; Ngo, Q. P.; et al. Roll-to-Roll Gravure Printed Electrochemical Sensors for Wearable and Medical Devices. *ACS Nano.* June 20, 2018. pp. 6978–6987. https://doi.org/10.1021/acsnano.8b02505.

(15) Sekine, T.; Sugano, R.; Tashiro, T.; Sato, J.; Takeda, Y.; Matsui, H.; Kumaki, D.; Dos Santos, F. D.; Miyabo, A.; Tokito, S. Fully Printed Wearable Vital Sensor for Human Pulse Rate Monitoring Using Ferroelectric Polymer. *Scientific. Reports.* March 13, 2018. pp. 1–10. https://doi.org/10.1038/s41598-018-22746-3.

(16) Chen, S.; Song, Y.; Xu, F. Flexible and Highly Sensitive Resistive Pressure Sensor Based on Carbonized Crepe Paper with Corrugated Structure. *ACS Applied Materials Interfaces.* September 18, 2018. pp. 34646–34654. https://doi.org/10.1021/acsami.8b13535.

(17) Cao, R.; Wang, J.; Zhao, S.; Yang, W.; Yuan, Z.; Yin, Y.; Du, X.; Li, N. W.; Zhang, X.; Li, X.; et al. Self-Powered Nanofiber-Based Screen-Print Triboelectric Sensors for Respiratory Monitoring. *Nano Research.* August 2, 2018, pp. 3771–3779. https://doi.org/10.1007/s12274-017-1951-2.

(18) Jung, S.; Sou, A.; Gili, E.; Sirringhaus, H. Inkjet-Printed Resistors with a Wide Resistance Range for Printed Read-Only Memory Applications. *Organic Electronics.* March 2013. pp. 699–702. https://doi.org/10.1016/j.orgel.2012.12.034.

(19) Preinfalk, J. B.; Eiselt, T.; Wehlus, T.; Rohnacher, V.; Hanemann, T.; Gomard, G.;

Lemmer, U. Large-Area Screen-Printed Internal Extraction Layers for Organic Light-Emitting Diodes. *ACS Photonics.* February 24, 2017. pp. 928–933. https://doi.org/10.1021/acsphotonics.6b01027.

(20) Mikolajek, M.; Reinheimer, T.; Bohn, N.; Kohler, C.; Hoffmann, M. J.; Binder, J. R. Fabrication and Characterization of Fully Inkjet Printed Capacitors Based on Ceramic/Polymer Composite Dielectrics on Flexible Substrates. *Scientific Reports.* September 16, 2019. pp. 1–13. https://doi.org/10.1038/s41598-019-49639-3.

(21) Liu, H.; Crooks, R. M. Three-Dimensional Paper Microfluidic Devices Assembled Using the Principles of Origami. *Journal of American Chemical Society.* October 17, 2011. pp. 17564–17566. https://doi.org/10.1021/ja2071779.

(22) Hamedi, M. M.; Ainla, A.; Güder, F.; Christodouleas, D. C.; Fernández-Abedul, M. T.; Whitesides, G. M. Integrating Electronics and Microfluidics on Paper. *Advanced Materials.* May 2, 2016. pp. 5054–5063. https://doi.org/10.1002/adma.201505823.

(23) Fu, E.; Lutz, B.; Kauffman, P.; Yager, P. Controlled Reagent Transport in Disposable 2D Paper Networks. *Lab on a Chip.* January 15, 2010. pp. 918–920. https://doi.org/10.1039/b919614e.

(24) Olkkonen, J.; Lehtinen, K.; Erho, T. Flexographically Printed Fluidic Structures in Paper. *Analitical Chemistry.* November 13, 2010. pp. 10246–10250. https://doi.org/10.1021/ac1027066.

(25) Wang, S. Q.; Chinnasamy, T.; Lifson, M. A.; Inci, F.; Demirci, U. Flexible Substrate-Based Devices for Point-of-Care Diagnostics. *Trends in Biotechnology*. November 1, 2016. pp. 909–921. https://doi.org/10.1016/j.tibtech.2016.05.009.

(26) Tian, T.; Wei, X.; Jia, S.; Zhang, R.; Li, J.; Zhu, Z.; Zhang, H.; Ma, Y.; Lin, Z.; Yang, C. J. Integration of Target Responsive Hydrogel with Cascaded Enzymatic Reactions and Microfluidic Paper-Based Analytic Devices (MPADs) for Point-of-Care Testing (POCT). *Biosensors and Bioelectronics.* March 15, 2016. pp. 537–542. https://doi.org/10.1016/j.bios.2015.09.049.

(27) Hu, J.; Wang, S. Q.; Wang, L.; Li, F.; Pingguan-Murphy, B.; Lu, T. J.; Xu, F. Advances in Paper-Based Point-of-Care Diagnostics. *Biosensors and Bioelectronics*. April 15, 2014. pp. 585–597. https://doi.org/10.1016/j.bios.2013.10.075.

(28) Noviana, E.; Henry, C. S. Simultaneous Electrochemical Detection in Paper-Based Analytical Devices. *Current Opinion in Electrochemistry*. October 1, 2020. pp. 1–6. https://doi.org/10.1016/j.coelec.2020.02.013.

(29) Yang, Y.; Noviana, E.; Nguyen, M. P.; Geiss, B. J.; Dandy, D. S.; Henry, C. S. Paper-Based Microfluidic Devices: Emerging Themes and Applications. *Analytical Chemistry.* December 7, 2016. pp. 71-91. https://doi.org/10.1021/acs.analchem.6b04581.

(30) Akyazi, T.; Basabe-Desmonts, L.; Benito-Lopez, F. Review on Microfluidic Paper-Based Analytical Devices towards Commercialisation. *Analytica Chimica Acta*. February 25, 2018. pp. 1–17. https://doi.org/10.1016/j.aca.2017.11.010.

(31) Katz, E.; Bollella, P. Fuel Cells and Biofuel Cells: From Past to Perspectives. *Israel Journal of Chemistry.* May 19, 2020, ijch.202000039. https://doi.org/10.1002/ijch.202000039.

(32) Nasar, A.; Perveen, R. Applications of Enzymatic Biofuel Cells in Bioelectronic Devices – A Review. *International Journal of Hydrogen Energy*. June 7, 2019. pp. 15287–15312. https://doi.org/10.1016/j.ijhydene.2019.04.182.

(33) Grattieri, M.; Minteer, S. D. Self-Powered Biosensors. *ACS Sensors*. November 21, 2018. pp. 44–53. https://doi.org/10.1021/acssensors.7b00818.

(34) Liu, Z.; Cho, B.; Ouyang, T.; Feldman, B. Miniature Amperometric Self-Powered Continuous Glucose Sensor with Linear Response. *Analytical* Chemistry. March 14, 2012. pp. 3403–3409. https://doi.org/10.1021/ac300217p.

(35) Cheng, H.; Yu, P.; Lu, X.; Lin, Y.; Ohsaka, T. Biofuel Cell-Based Self-Powered Biogenerators for Online Continuous Monitoring of Neurochemicals in Rat Brain. *Analyst*. October 23, 2012. pp. 179–185. https://doi.org/10.1039/c2an36385b.

(36) Zhang, L.; Zhou, M.; Dong, S. A Self-Powered Acetaldehyde Sensor Based on Biofuel Cell. *Analytical Chemistry.* November 5, 2012, pp. 10345–10349. https://doi.org/10.1021/ac302414a.

(37) Meredith, M. T.; Minteer, S. D. Inhibition and Activation of Glucose Oxidase Bioanodes for Use in a Self-Powered EDTA Sensor. *Analytical Chemistry.* May 31, 2011. pp. 5436–5441. https://doi.org/10.1021/ac2011087.

(38) Hickey, D. P.; Reid, R. C.; Milton, R. D.; Minteer, S. D. A Self-Powered Amperometric Lactate Biosensor Based on Lactate Oxidase Immobilized in

Dimethylferrocene-Modified LPEI. *Biosensors and Bioelectronics.* March 15. pp. 26–31. https://doi.org/10.1016/j.bios.2015.09.013.

(39) Sekretaryova, A. N.; Beni, V.; Eriksson, M.; Karyakin, A. A.; Turner, A. P. F.; Vagin, M. Y. Cholesterol Self-Powered Biosensor. *Analytical Chemistry.* August 28, 2014. pp. 9540–9547. https://doi.org/10.1021/ac501699p.

(40) Kim, J.; Jeerapan, I.; Imani, S.; Cho, T. N.; Bandodkar, A.; Cinti, S.; Mercier, P. P.; Wang, J. Noninvasive Alcohol Monitoring Using a Wearable Tattoo-Based Iontophoretic-Biosensing System. *ACS Sensors*. July 12, 2016. pp. 1011–1019. https://doi.org/10.1021/acssensors.6b00356.

(41) Xu, Z.; Liu, Y.; Williams, I.; Li, Y.; Qian, F.; Wang, L.; Lei, Y.; Li, B. Flat Enzyme-Based Lactate Biofuel Cell Integrated with Power Management System: Towards Long Term in Situ Power Supply for Wearable Sensors. *Applied Energy.* May 15, 2017. pp. 71–80. https://doi.org/10.1016/j.apenergy.2017.01.104.

(42) Cho, E.; Mohammadifar, M.; Choi, S. A Self-Powered Sensor Patch for Glucose Monitoring in Sweat. In *Proceedings of the IEEE International Conference on Micro Electro Mechanical Systems (MEMS)*. 2017. pp 366–369. https://doi.org/10.1109/MEMSYS.2017.7863417.

(43) Mohammadifar, M.; Tahernia, M.; Yang, J.; Koh, A.; Choi, S. A Skin-Mountable Bacteria-Powered Battery System for Self-Powered Medical Devices. In *Proceedings of the IEEE International Conference on Micro Electro Mechanical Systems (MEMS)*. 2020; pp 72–75. https://doi.org/10.1109/MEMS46641.2020.9056174.

(44) Baingane, A.; Slaughter, G. Self-Powered Electrochemical Lactate Biosensing. *Energies*. October 12 2017. pp. 1582 (1-9). https://doi.org/10.3390/en10101582.

(45) Sode, K.; Yamazaki, T.; Lee, I.; Hanashi, T.; Tsugawa, W. BioCapacitor: A Novel Principle for Biosensors. *Biosensors and Bioelectronics.* February 15, 2016. pp. 20–28. https://doi.org/10.1016/j.bios.2015.07.065.

(46) Hanashi, T.; Yamazaki, T.; Tsugawa, W.; Ferri, S.; Nakayama, D.; Tomiyama, M.; Ikebukuro, K.; Sode, K. BioCapacitor-A Novel Category of Biosensor. *Biosensors and Bioelectronics.* March 15, 2009. pp. 1837–1842. https://doi.org/10.1016/j.bios.2008.09.014.

(47) Garcia, S. O.; Ulyanova, Y. V.; Figueroa-Teran, R.; Bhatt, K. H.; Singhal, S.; Atanassov, P. Wearable Sensor System Powered by a Biofuel Cell for Detection

of Lactate Levels in Sweat. *ECS Journal of Solid State Science and Technology.* May 4, 2016. pp. M3075–M3081. https://doi.org/10.1149/2.0131608jss.

(48) Montes-Cebrián, Y.; del Torno-de Román, L.; Álvarez-Carulla, A.; Colomer-Farrarons, J.; Minteer, S. D.; Sabaté, N.; Miribel-Català, P. L.; Esquivel, J. P. 'Plug-and-Power' Point-of-Care Diagnostics: A Novel Approach for Self-Powered Electronic Reader-Based Portable Analytical Devices. *Biosensors and Bioelectronics.* October 30, 2018. pp. 88–96. https://doi.org/10.1016/j.bios.2018.07.034.

(49) Sailapu, S. K.; Macchia, E.; Merino-Jimenez, I.; Esquivel, J. P.; Sarcina, L.; Scamarcio, G.; Minteer, S. D.; Torsi, L.; Sabaté, N. Standalone Operation of an EGOFET for Ultra-Sensitive Detection of HIV. *Biosensors and Bioelectronics.* May 15, 2020. pp. 112103. https://doi.org/10.1016/j.bios.2020.112103.

(50) Jeerapan, I.; Sempionatto, J. R.; Pavinatto, A.; You, J. M.; Wang, J. Stretchable Biofuel Cells as Wearable Textile-Based Self-Powered Sensors. *Journal of Materials Chemistry A*. 2016. pp. 18342–18353. https://doi.org/10.1039/C6TA08358G.

(51) Bandodkar, A. J.; You, J.-M.; Kim, N.-H.; Gu, Y.; Kumar, R.; Vinu Mohan, A. M.; Kurniawan, J.; Imani, S.; Nakagawa, T.; Parish, B.; et al. Soft, Stretchable, High Power Density Electronic Skin-Based Biofuel Cells for Scavenging Energy from Human Sweat. *Energy and Environmental Science.* June 15*,* 2017. pp. 1581–1589. https://doi.org/10.1039/c7ee00865a/02/2018.

(52) Guan, H.; Zhong, T.; He, H.; Zhao, T.; Xing, L.; Zhang, Y.; Xue, X. A Self-Powered Wearable Sweat-Evaporation-Biosensing Analyzer for Building Sports Big Data. *Nano Energy.* March 12, 2019. pp. 754–761. https://doi.org/10.1016/j.nanoen.2019.03.026.

2.

BASICS OF THE CONDUCTIVITY PAPER BATTERY-SENSOR

Overview

In this chapter we introduce the operating principle of a paper-based battery and its application to a novel approach of performing a measure of ionic conductivity with a self-powered strategy. The battery sensor unit, which is the cornerstone of the present thesis, consists of two electrodes placed side-by-side and covered by a piece of hydrophilic paper strip. The electrodes are externally connected to a resistive element. The addition of the fluid to be sensed, which acts as electrolyte, activates the battery, which generates an output voltage that is dependent on the conductivity of the liquid sample. The device, which is conceived as a single use disposable sensor, has been tested with different synthetic and biological liquid samples. The battery sensor effectiveness has been assessed by comparing its performance with a commercial laboratory conductometer.

Introduction

Batteries are electrochemical devices that convert stored chemical energy into electrical energy. There are two main types of batteries: primary and secondary batteries. Primary batteries are those in which the electrochemical reactions are irreversible, that is, after the battery has been discharged it cannot recover its initial state and be reused again. In secondary batteries, the electrochemical reaction is reversible and the battery can be recharged by supplying direct current from an external source and reused multiple times.

Primary batteries generate electrical energy by coupling two redox reactions of different sign (i.e. oxidation and reduction reactions) and generally consist of two metals connected by an ion-conducting media, typically a salt bridge or an ion exchange membrane. The main function of the salt bridge or the ion exchange membrane is to provide ionic contact between the electrodes and if required, prevent the solutions surrounding one of the electrodes (electrolytes) from mixing and causing unwanted side reactions in the other. Figure 1 depicts a schematic representation of a primary battery. A big variety of primary battery chemistries and architectures has been reported over the last century and extensive literature about the subject can be found elsewhere[1].

In the last fifty years, primary batteries have found a prolific niche of application in small-sized portable devices and their chemistries and formats have been fixed to a limited assortment of choices. Some of the most common commercial primary battery chemistries are listed in Table 1[2], whereas their portable formats are mainly cylindrical (e.g. A, AA, AAA), rectangular (generally for battery stacking) or coin-shaped (very small appliances). In the last decade, card-shaped battery formats have appeared to fulfill the needs of printed electronic devices[3].

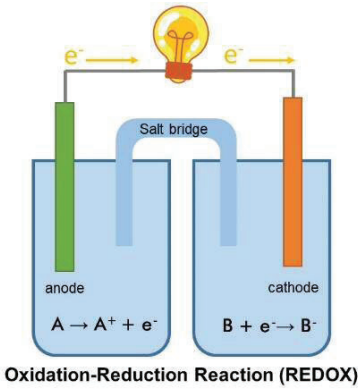

Figure 1: Basic scheme of a primary battery.

Table 1. Description of the most common chemistries used in small-sized commercial primary battery

Battery system	Cell reaction	Potential (V)
Leclanché	$Zn + 2MnO_2 + 2NH_4Cl \rightarrow ZnNH_3Cl_2 + Mn_2O_3$	1.5
Manganese alkaline	$Zn + 2MnO_2 + 2H_2O \rightarrow ZnO + Mn_2O_3$	1.5
Silver oxide/zinc	$Zn + Ag_2O + H_2O \rightarrow Zn(OH)_2 + 2Ag$	1.6
Air/zinc (alkaline)	$2Zn + O_2 \rightarrow 2ZnO$	1.45
Lithium/manganese dioxide	$Li + Mn^{4+}O_2 \rightarrow Mn^{3+}O_2 + (Li^+)$	3.5

Despite the maturity of portable primary batteries, the rising of a new generation of paper-based devices, that require power sources compatible with their structural materials, operating principles and disposability, have originated the quest for new and flexible formats of batteries that use paper as the main structural material. Indeed, paper-based batteries are generally fabricated on paper (or paper-like) substrates by depositing electrodes on the paper and/or by introducing electrolytes in a dry state into a whole paper or hydrophilic regions patterned within the paper. The first paper-based prototype was presented in 2005[3] and consisted on a magnesium film and a copper layer connected by an absorbent paper doped with copper chloride. The battery operation was activated by the addition of urine, that allowed the copper chloride to dissolve and act as the battery electrolyte. Since then, a variety of paper-based battery prototypes that make use of different chemistry combinations have been reported. Generally, most of these devices are galvanic cells that use aluminum, magnesium or zinc as anodic material. These three main anodic components are then combined with a wide assortment of cathodic choices that range from carbon for oxygen reduction to redox polymers, metals and metal oxides. Hilder et al. presented a flexible paper-based zinc-carbon battery that delivered 500 μA at 0.8 V for two days[4]. Later on, Wang and coworkers improved slightly the battery performance by adding multiwalled carbon nanotubes (MWCNTs) into the cathode[5]. The combination of Zn electrodes with a Fe_3O_4 cathode in highly alkaline water-based electrolytes has allowed to demonstrate superior performances (2.2 V open circuit potentials and up to 7 mA of maximum output currents). However, its 3D format together with the 6 M KOH content of the electrolyte, limit severely its applicability to paper-based disposable devices[6]. Besides, the use of aluminum as anodic material has attracted broader attention of paper-based developers due to its noteworthy high theoretical voltage (2.7 V) and an energy density (8.1 kWh kg^{-1}). Moreover, it is a ubiquitous low-cost material, which makes it ideal for single use applications. Remarkable implementation examples in

the literature are cited in the following. Ferreira et al. reported a simple Al-Cu battery that yielded 0.7 V and current densities up to 0.5 mA cm^{-2} depending on the paper composition, thickness and the degree of OH_x species adsorbed in the paper matrix that acted as electrolyte recipient[7]. F.A. Gomez has recently presented two battery developments that combined an Al anode with a carbon-based cathode for oxygen reduction in alkaline media and an AgO/Ag cathode. Both approaches require the presence of KOH electrolytic salts and delivered 1.2 V and 1.6 V for a period of approximately 10 min respectively[8,9]. The performance of Al-air paper batteries can be significantly improved by making use of the unique features provided by fluid capillarity, that allows to remove the side products of reacted species and provides better access to oxygen in the cathode[10,11]. Despite its interesting features regarding performance and biocompatibility/biodegradability, magnesium has been scarcely used in paper devices. Y. Koo and coworkers reported a battery that combined a magnesium anode and a silver cathode and showed its capability to power a LED component. The battery was activated upon the addition of 160 μl of fluid, which dissolved the silver nitrate and the magnesium chloride salts stored in the paper that acted as electrolytes for each of the half-cell reactions[12]. In fact, examples of liquid-activated batteries in which the battery starts to function upon the addition of a fluid that acts as the aqueous support of the battery electrolyte had raised some attention in the last years. Their limited operating time and simplicity in terms of structure and materials used make them particularly suitable for short-term applications such as diagnostics or wearable devices. A paper-based electrochemical sensing platform with an integrated Al/Ag battery showed the viability of integrating the power source on the same paper substrate than the assay[13]. A similar chemistry had been also used to power a surface-mount UV LED on a paper and conduct an on-chip fluorescence assay after the sample addition[14]. A more sustainable alternative to the use of $Ag/AgNO_3$ cathodic chemistry is presented when using the Carbon/$FeCl_3$, which also allows to decrease the overall cost of the device without limiting the performance[15].

The basic electrochemistry used in the paper-based batteries developed in the present thesis is well-known and reported, especially in the domain of the so-called seawater-activated batteries[16,17]. We have chosen magnesium in front of other suitable candidates described before (zinc or aluminum) due to its low oxidation potential and its capability of operating at neutral media. Besides, the chemistry chosen at the cathode consists on the reduction of AgCl to Ag. This reaction takes place without the assistance of any additional electrolytic salt and its low cost and commercial availability of printable inks determined our choice. The experimental open circuit potential (V_{OCP}) of Mg - Ag/AgCl batteries is set around 1.5-1.7 V[18]. The reactions involved in the paper battery are as follows:

The battery unit that constitutes the key element of the present thesis consists of two electrodes, anode and cathode, placed side-by-side and covered by a piece of hydrophilic paper strip. More precisely, the battery-sensor explored in this thesis, consists of a magnesium anode and a silver/silver chloride cathode of dimensions 2.5 x 5 mm^2 located side by side onto a pressure sensitive adhesive layer, used as a structural substrate, at a distance of 1.5 mm. The electrodes are covered and connected with two layers of glass fiber-based paper with a total thickness of 0.5 mm and an area of 60 mm^2. The glass-fiber paper is a highly hydrophilic material that holds a liquid volume of 15 µL. The paper-like material connects both electrodes and creates a cavity that will play the role of electrolyte. In this sense, the battery remains inactive until an ion-conducting fluid is poured onto the paper. Figure 2 shows a picture taken to a ready-to-use paper battery and the moment in which a liquid is dropped onto the battery paper core.

The battery fabrication process starts with the screen printing process of the cathode. A manual screen-printer (PAYMSER, Barcelona, Spain) is used for that purpose. The screen-printing process starts with the patterning of a collector track on a PET substrate (polyethylene terephthalate) that provides electrical conductivity to the electrode. The track is printed with the Ag ink LOCTITE ECI 1011 E&C (Henkel, Düsseldorf, Germany) and

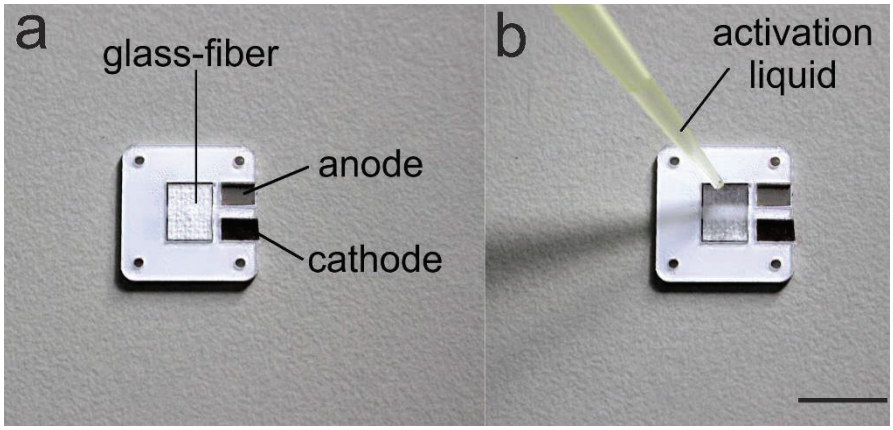

Figure 2. Fabricated paper-based battery unit a) in dry form and b) introducing an activation liquid (scale bar = 1 cm).

cured at 150ºC for 15 minutes. Then, the working electrode area is defined with the same technique on top of the previous track with the Ag/AgCl ink C2140310D1 (Gwent Electronic Materials Ltd., Pontypool, Wales) and cured at 60 ºC for 30 minutes. Figure 3a shows a picture of one of the laminated substrates after the whole printing process. Then, the Mg anode was cut from a 10 x 10 cm sheet of 50 µm thickness obtained from GalliumSource LLC (Scotts Valley, CA, USA). Figure 3b displays a detail of a magnesium foil used as anodic material. Both paper LF1 Glass Fiber Filter from General Electric, Boston, MA, USA) and pressure sensitive adhesives (from Adhesive Research, Glen Rock, PA, USA) geometries were designed with CorelDraw (Corel, Ottawa, ON, Canada) and cut with a CO_2 laser (Mini 24, Epilog Laser, Golden, CO, USA). The device was then manually mounted. Alignment jigs were used to ensure the accurate assembly of all the battery components. Figure 4 shows an exploded view of all the materials and layers used in the battery fabrication process.

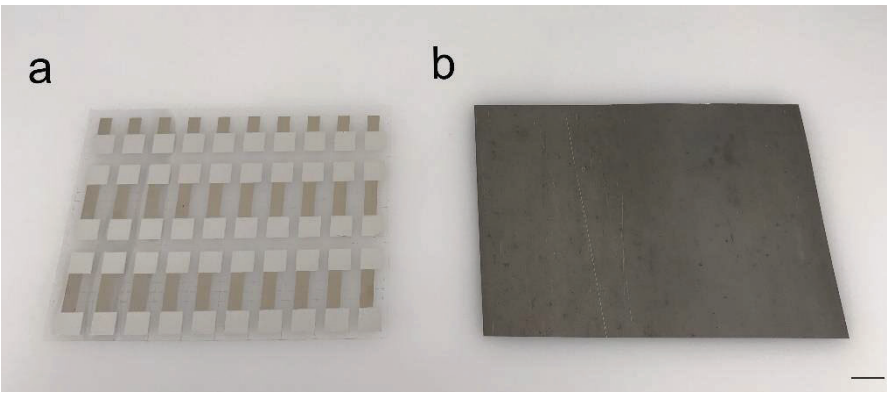

Figure 3. a) Substrate of Ag/AgCl screen printed electrodes b) Magnesium foil (scale bar = 1 cm).

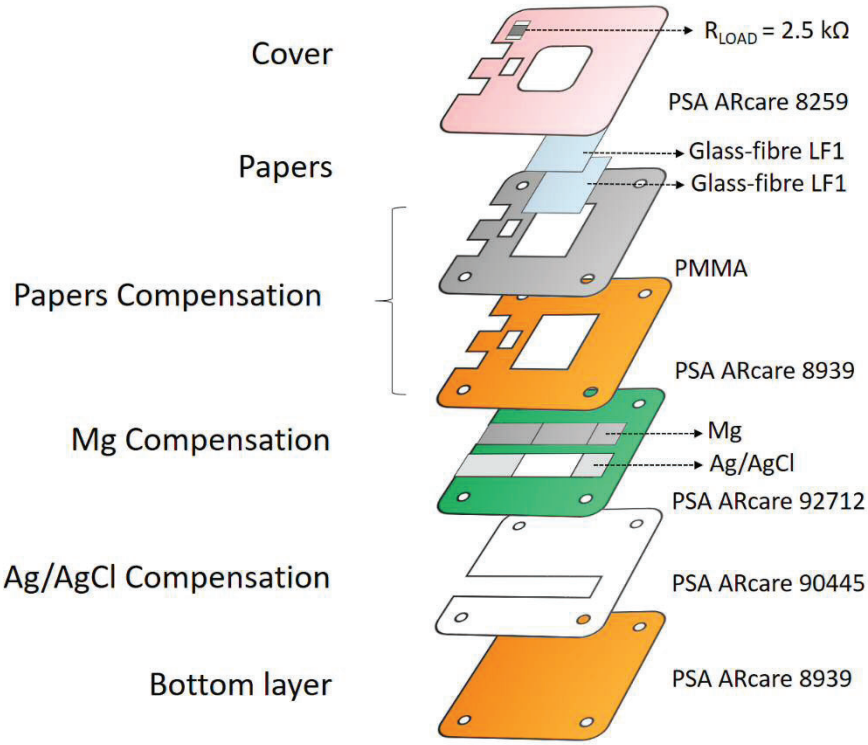

Figure 4. Exploded vision of layers and materials inside the battery.

Results and discussion

Battery performance and characterization

Polarization curves provide information about the voltage generated by the cell depending on the current demand. Figure 5 depicts a scheme of a generic polarization curve. Departing from its open circuit potential (V_{OCP}) that depends on the battery chemistry and the electrolyte pH, batteries experience voltage losses that can be attributed to different physical-chemical phenomena:

(1) Activation losses due to limitations on the rate of the electrochemical reactions at the electrodes;

(2) Ohmic losses due to limitations of the ionic and electronic conduction across the different elements of the battery (electrodes, connecting wires, electrolyte);

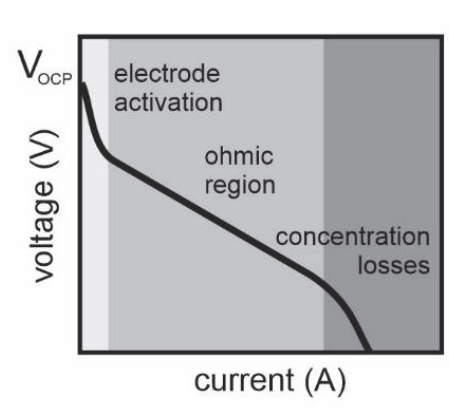

Figure 5. I-V characteristic polarization curve of the paper-battery where the different contributions to voltage losses are identified with different grey tones.

(3) Concentration losses due to limitations on the diffusion of the electrolytic solutions and/or the current density that the electrodes are able to provide.

According to the polarization curve presented herein, the electrode material choice and the selected pH of the activation liquid will determine the activation losses, whereas the geometrical configuration of the battery (paper type and thickness, electrode area, thickness and separation) and the ionic conductivity of the liquid will determine the magnitude of the ohmic losses. Concentration losses will depend on one side on the specific materials chosen to fabricate the electrodes and the ionic conductivity of the activation fluid.

A preliminary characterization of the battery I-V characteristics was performed by activating the device with a water solution containing 1M NaCl. The electrochemical characterization of the battery was performed with an Autolab Potentiostat PGSTAT204 (Metrohm AG, Herisau, Switzerland) that, departing from a zero-current situation, monitored the current delivered by the battery at different output voltages. The voltage scan was performed at 10 $mV \cdot s^{-1}$. Figure 6 shows the polarization curve obtained together with the output power delivered by the device.

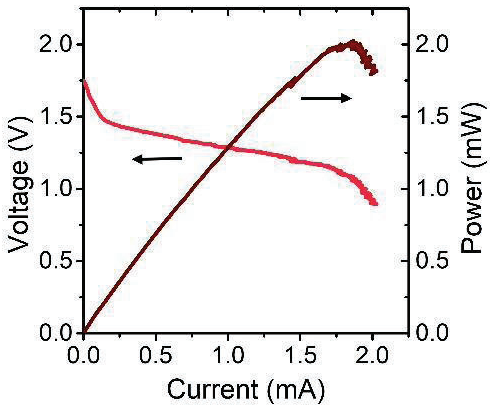

Figure 6: Voltage and power outputs recorded from the paper-based battery unit after its activation with 15 µl of 1M NaCl solution.

Paper-battery as self-powered conductivity sensor

In order to turn the paper battery into a conductivity sensor, special emphasis has to be placed on the ohmic losses region of the battery. In this operating region, the performance of the battery is directly driven by the magnitude of its internal resistance[19], which is composed by the faradaic resistance of the electrodes (R_F), the ionic resistivity of the electrolyte (R_E) and ohmic resistance of the electrodes and the electrical contacts of the battery (R_C). Figure 7 shows a scheme that identifies all the resistive contributions that can be attributed to the different components of the battery.

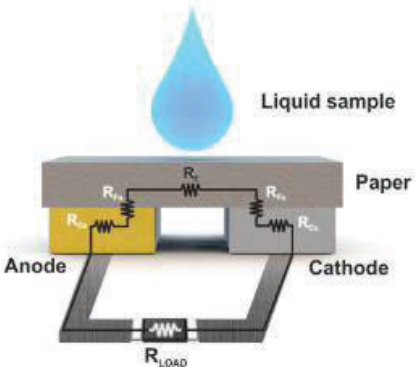

Figure 7. Scheme of the paper battery-sensor showing all the resistive contributions governing the performance of the battery. (Reprinted with permission from[19]. Copyright 2020 American Chemical Society).

Whereas R_F has a significant effect on voltage losses at low current ranges and becomes practically negligible at moderate currents, ionic and electronic resistivity are constant along the whole operating range of the battery. In particular, the ionic resistivity of the electrolyte depends on the geometrical dimensions of the paper, its porosity and the ionic conductivity of the fluid used to activate its operation. Therefore, if the battery features are kept unaltered regarding component materials and geometry, the internal resistivity of the battery will solely change upon variations in the conductivity of the fluid, which will have an impact in the slope of the ohmic region of its polarization curve. This turns the battery into a self-powered conductivity sensor, as its output voltage and current will directly depend on the ionic conductivity of the activation liquid.

One simple way to operate the battery sensor is to connect a resistor (R_{LOAD}) in series to the battery electrodes. Under this resistive load, the voltage output of the battery (V_σ) will correspond to the value set by the intersection of the polarization curve at a given activation liquid conductivity and the loading resistor, as shown in Figure 8. In this configuration, the output voltage of the battery can be derived from equations 1 and 2, where V_{OCP} corresponds to the open circuit voltage of the battery, R_σ to the internal resistance of the battery at a given liquid electrolyte conductivity (σ) and i_σ and V_σ correspond to the current and voltage output of the battery when connected to the external resistor.

$$V_\sigma = V_{OCP} - i_\sigma R_\sigma = i_\sigma R_{LOAD} \quad (1)$$

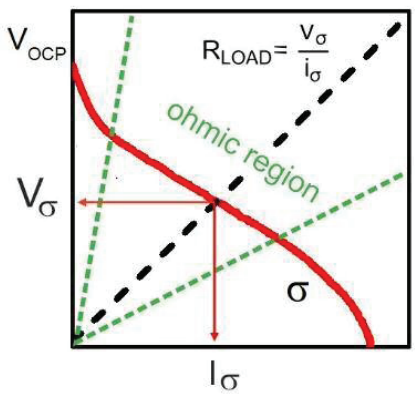

Figure 8. I-V characteristic polarization curve of the paper-battery (solid line). External resistive load R_{LOAD} connected to the battery (dashed line) intersects I-V curve in the ohmic region so battery operates at Vσ and iσ, values directly related with the internal resistance of the paper battery-sensor.

$$V_\sigma = \frac{V_{OCP} \cdot R_{LOAD}}{R_\sigma + R_{LOAD}} \quad (2)$$

It can be seen that according to (2), the voltage delivered by the battery depends on the value of its internal resistance whereas the value of the external resistance connected to it, modulates the battery response. In order to find out which is the value of R_{LOAD} that provides the maximum sensitivity to internal resistivity changes, we calculated the sensitivity (equation 3).

$$S = \frac{\partial V_\sigma}{\partial R_\sigma}\frac{\partial R_\sigma}{\partial \sigma} = \frac{-V_{OCP} R_{LOAD}}{(R_\sigma + R_{LOAD})^2}\frac{\partial R_\sigma}{\partial \sigma} \quad (3)$$

From this expression, it can be seen that the battery sensitivity to conductivity changes of the electrolyte diminishes at increasing conductivity values. Moreover, it is easy to derive that the maximum sensitivity to internal resistance changes takes place when R_{LOAD} equals R_σ, that is, when the external resistance equals the value of the internal resistance of the battery. This means that selecting the loading resistor is a key step in the implementation of the conductivity battery sensor device, as for a particular conductivity range of interest, the maximum attainable sensitivity will be equal to:

$$S_{max} = \frac{V_{OCP}}{4R_\sigma}\frac{\partial R_\sigma}{\partial \sigma} \quad (4)$$

where R_σ is a particular value of the internal resistivity of the battery previously selected.

In the case where ohmic losses attributed to electrical contacts are minimized and the internal resistivity of the battery is dominated by the paper electrolyte resistivity, the internal resistance can be expressed as:

$$R_\sigma = R_{electrolyte} = \frac{k}{\sigma} \quad (5)$$

where k corresponds to the cell constant and σ corresponds to the effective liquid conductivity, which is the conductivity of the liquid embedded in the paper matrix. In this case, the maximum sensitivity is independent of the cell geometry and can be directly related to the conductivity of the electrolyte:

$$S_{max} = \frac{V_{OCP}}{4\sigma} \quad (6)$$

As it can be seen, the sensitivity decreases inversely proportional to the ionic conductivity, which limits the applicability of this self-powered strategy to low and moderate liquid conductivities. It is clear that under this scenario, the open circuit potential delivered by the chemistry selected at the electrodes can be used to increase the device sensitivity. In Figure 9 we have depicted the maximal sensitivity values that would be obtained in a battery yielding 1 V of open circuit potential. Calculations do not take into account the paper contribution to the electrolyte conductivity, so in practice, the sensitivity of the battery will diminish for paper of low porosity.

Compared to the state-of-the-art conductivity sensors, the battery-sensor presents two main advantages: (1) its response to conductivity can be characterized by a direct current (DC) that enables a radical simplification of the electronic module to operate it, and (2) if desired, the sensor response can be obtained without an additional power source; thus, it can be operated as a self-powered sensor.

In order to calibrate the performance of our battery at different ionic conductivities, we recorded the battery polarization curves when filled with water-based solutions containing different ionic conductivities. Solutions with different NaCl concentrations were prepared to set liquid conductivities to the ranges typically found in body fluids and beverages (0.5 mS cm^{-1} to 10 mS cm^{-1}). The solutions were daily prepared and the conductivity and temperature of the solutions were measured with the 914 pH/Conductometer (Metrohm AG, Herisau, Switzerland).

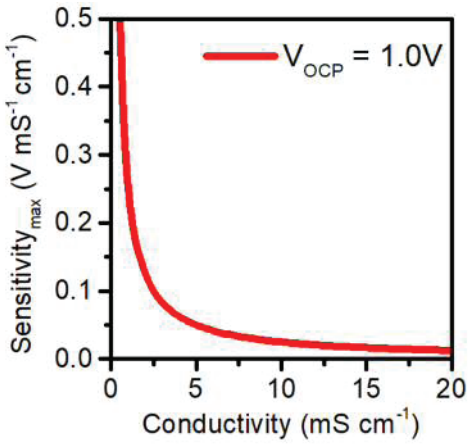

Figure 9. Maximum obtainable sensitivity with the paper battery-sensor when V_{OCP} is 1V.(Reprinted with permission from[19]. Copyright 2020 American Chemical Society).

Figure 10 shows the obtained polarization curves of the battery once the solution was introduced in the paper matrix. The open circuit voltage of the batteries was first measured for 20 seconds and afterwards a linear sweep voltammetry at 10 mV s^{-1} was performed from the open circuit voltage to 0 V.

The effect of the ionic conductivity of the activation liquid in the ohmic region of the curves is clear. It can be also noticed that voltage losses related to the Faradaic resistance of the electrodes in the activation zone of the I-V curve are significant, in particular at conductivity ranges below 3 mS cm^{-1}. An individual electrochemical characterization of both magnesium and silver/silver chloride electrodes was performed to analyze the origin of the activation losses observed in Figure 10. The half-cell measurements with both electrodes were performed with a commercial Ag/AgCl as the reference electrode and a Pt electrode as the counter inside a beaker. The magnesium anode and the silver/silver chloride cathode were connected as the working electrode in each of the experiments. A linear sweep voltammetry at 10 mV s^{-1} at different conductivities with the two electrodes revealed that the activation losses were dominated by the magnesium anode, as shown in Figure 11, probably due to the existence of a passivating layer of magnesium oxide in the anode. The effect of this passivating layer becomes less prominent at increasing conductivities, mainly due to the fact that the presence of chloride ions increases the rate of the anodic dissolution kinetics[20]. On the contrary, the Ag/AgCl cathode turned out to be completely independent of the electrolyte conductivity (and even from Cl^- content of the

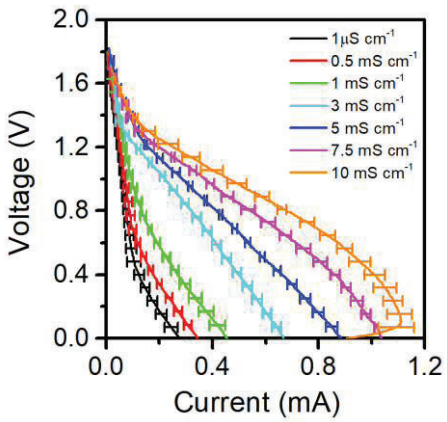

Figure 10. Polarization curves of the paper battery-sensor when tested at conductivities from 1 μS cm^{-1} to 10 mS cm^{-1}. Lines represent mean values, error bars represent ± one standard deviation, for N = 3. (Reprinted with permission from[19]. Copyright 2020 American Chemical Society).

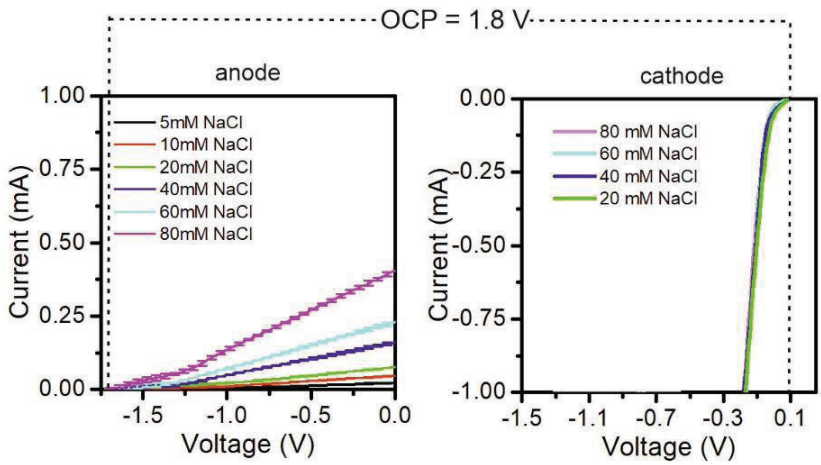

Figure 11. Partial reactions of the paper battery-sensor electrodes when introducing different electrolyte conductivities. Lines represent mean values, error bars represent ± one standard deviation, for N = 3.

solution). As it can be seen in Figure 11 (right), it was able to deliver high current with very low voltage losses, turning the Mg anode into the limiting electrode.

To use this battery as a self-powered sensor that allows deriving information of the conductivity of a liquid sample, a resistor is connected in series to the battery electrodes. As it has been previously mentioned, the value of this resistor has to be selected so it places the battery operation within its ohmic region for the whole conductivity range to be measured. As it can be observed in Figure 12, for this specific battery geometry and composition, suitable values of R_{LOAD} range from 1 to 2.5 kΩ.

In fact, these values correspond to the values of internal resistance measured in the battery sensor at the lower and upper limit of the tested conductivity range. Figure 13 shows the battery sensor output voltage derived from the intersection of R_{LOAD} with the battery polarization curves for resistor values of 1 and 2.5 kΩ. They also define the voltage operating window of the cell. As expected, higher output voltages are obtained at higher R_{LOAD} values due to the fact that the battery operates at the upper zone of its ohmic region.

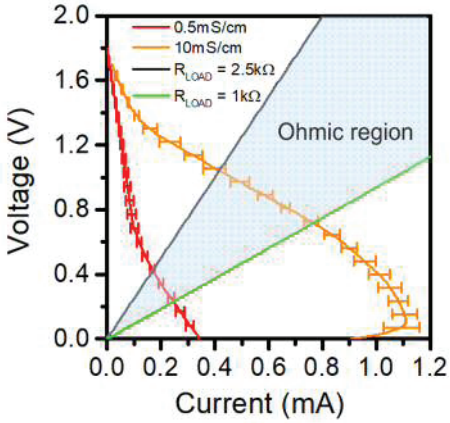

Figure 12. Polarization curves of the paper battery-sensor at the lower and upper values of the tested conductivity range (0.5 mS cm^{-1} and 10 mS cm^{-1}). R_{LOAD} from 1 kΩ to 2.5 kΩ (green and black solid lines) set the battery into the ohmic region operation. Lines represent mean values, error bars represent ± one standard deviation, for N = 3. (Reprinted with permission from[19]. Copyright 2020 American Chemical Society).

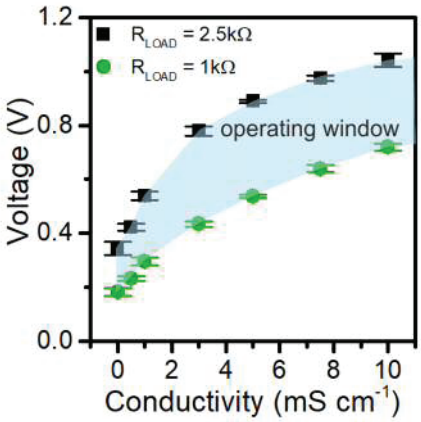

Figure 13. Output voltages obtained from the intersection of the battery polarization curves with R_{LOAD} set to 1 kΩ (green dots) and 2.5 kΩ (black squares). Data points represent mean values, error bars represent ± one standard deviation, for N = 3. (Reprinted with permission from[19]. Copyright 2020 American Chemical Society).

The derivative of the voltage curves allowed us to obtain the sensitivity of the sensor along the whole tested conductivity range, Figure 14. It can be seen that higher sensitivity is achieved at higher value of resistive load and that, as expected, sensitivity decreases significantly at increasing conductivity values. At the same time, impact of R_{LOAD} on

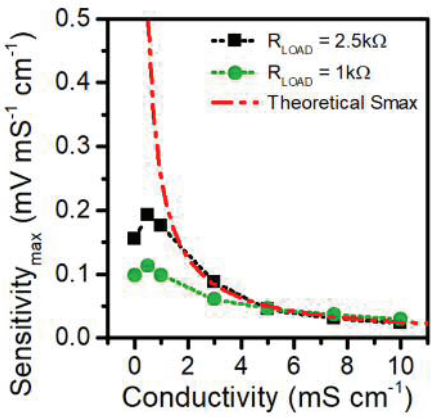

Figure 14. Sensitivity values of the battery obtained from the experimental polarization curves vs the theoretical maximum sensitivity (dashed red line). (Reprinted with permission from[19]. Copyright 2020 American Chemical Society).

sensitivity becomes less evident at conductivities above 5 mS cm^{-1}. Sensitivity values at low conductivities depart from the ideal 1/σ dependence due to the effect of the pre-existing passivation layer at the magnesium electrodes. In order to obtain the highest sensitivity response, a value of 2.5 kΩ was selected. The assembly was then thoroughly calibrated under continuous operation with different NaCl solutions. The battery was activated with 15 µl of the liquid samples and left to stabilize for 5 seconds. After that, the battery output voltage was recorded for 1 minute. The transient measurements to sense the output voltage of the battery once the resistor was connected in series were performed with an HP34401A Multimeter (Hewlett-Packard Palo Alto, CA, USA) and controlled with a custom-made LabVIEW program (National Instruments, N Mopac Expy, Austin, TX, USA).

Once the paper battery performance was calibrated within the conductivity range of interest, a battery sensor consumable was fabricated by incorporating a resistor in the paper-based device (see Figure 15).

Figure 16 shows the voltages generated by the battery over time at different conductivity values. It can be seen that battery voltages showed a significant stability for conductivities over 1.0 mS cm^{-1} along the measurement period whereas for lower conductivity values (0.5 and 1.0 mS cm^{-1}), the battery voltage showed a slight increase over time. This small voltage variation is due to the progressive removal of the passivation layer. During the calibration, the voltage output of the battery presented a repetitive behavior, providing voltages with a coefficient of variation of less than a 10% in all cases. A calibration curve

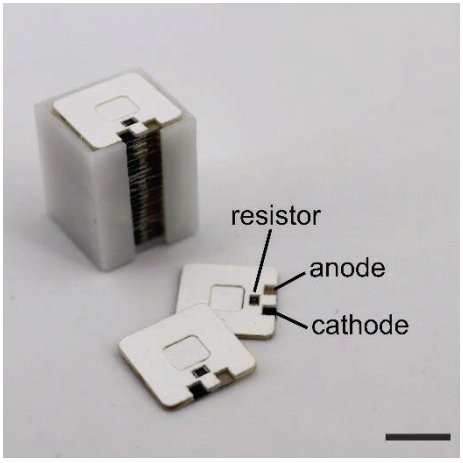

Figure 15. Picture of a ready-to-use conductivity battery-sensor (scale bar = 1 cm).

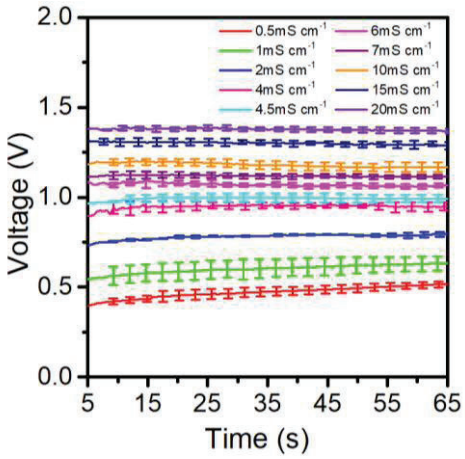

Figure 16. Battery output voltages under continuous operation at conductivities from 0.5 mS cm^{-1} to 20 mS cm^{-1}. Lines represent mean values, error bars represent ± one standard deviation, for N = 3. (Reprinted with permission from[19]. Copyright 2020 American Chemical Society).

was obtained by depicting the battery voltage output at a particular time (30 seconds) as shown in Figure 17.

The resulting values were fitted to expression (2) to which an additional term (V_0) had been added to account for the experimental offset value provided by the battery when activated with deionized water (1 μS cm-1), obtaining equation (7). Substituting the constant parameters in (7), the experimental results were fitted to the non-linear final expression (8), where k corresponds to the cell constant and V_{OCP}* to an effective value of the open

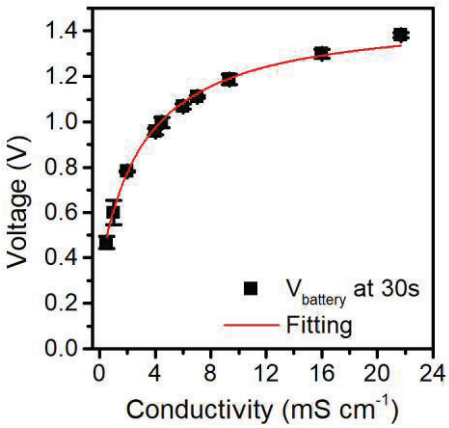

Figure 17. Calibration curve of the battery sensor. Data points represent mean values, error bars represent ± one standard deviation, for N = 3.(Reprinted with permission from[19]. Copyright 2020 American Chemical Society).

circuit potential of the battery (to which activation losses have been subtracted). A V_0 value of 0.33 V was extracted from the intersection of the corresponding polarization curve shown in Figure 13 with a R_{LOAD} of 2.5 kΩ. Fitting of the experimental values yielded an Adjusted R-Square of 0.9943 and k and V_{OCP}* coefficients that are presented in Table 2.

$$V_{out} = \frac{V^*_{OCP} \cdot R_{LOAD}}{\frac{k}{\sigma} + R_{LOAD}} + V_0 \quad (7)$$

$$V_{out} = \frac{V^*_{OCP} \cdot 2.5}{\frac{k}{\sigma} + 2.5} + 0.33 \quad (8)$$

Table 2. Battery voltage output fitting parameters

Parameter	**Value**	**Standard Error**
k	7.8	0.3
V_{OCP}*	1.15	0.02

It is worth noticing that as the sensor is a primary battery, its operational time depends on its charge capacity and the current intensity at which this charge is being released. In the

present case, despite its capability of delivering high density currents, the Ag/AgCl electrode was significantly thinner than the Mg anode and therefore, the total charge capacity of the sensor battery was limited by the total quantity of AgCl molecules available for reduction. We performed measurements of the current delivered by our sensor batteries under three different electrolyte conductivities until electrode exhaustion. They yielded an average charge capacity of 45 mC, which set to 80 seconds the maximum operational time at the highest conductivity tested value (20 mS cm^{-1}). Figure 18 shows the evolution of the current delivered by the battery at different conductivity levels.

After the battery sensor calibration, the device performance as single-use self-powered conductometer was validated by measuring conductivities of real liquid samples such as milk, juice, artificial eccrine perspiration, urine, lake water and phosphate butter. Artificial eccrine perspiration and artificial urine (Pickering Laboratories, Mountain View, CA, USA), phosphate buffer (Sigma-Aldrich, St Louis, Missouri, USA), milk samples (Central Lechera Asturiana, Asturias, Spain) and pineapple juice samples (Conserve Italia Soc Coop Agricola, Bologna, Italy) were used to perform the final validation of the device. Figure 19 shows the battery output voltages recorded for the different samples vs time with the same methodology used for the calibration.

As it can be seen, the battery sensor delivered output voltages with coefficient of variations of less than 10% in all cases regardless of the origin, synthetic or natural. Again, the

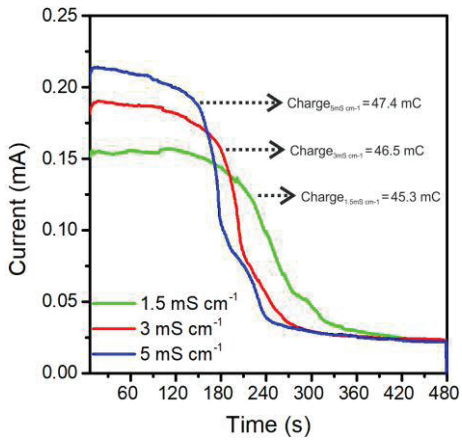

Figure 18. Current generated by the paper-based battery when introducing different sample conductivities. Integration of the current values generated during battery operation provides the amount of charge stored at the Ag/AgCl electrode. (Reprinted with permission from[19]. Copyright 2020 American Chemical Society).

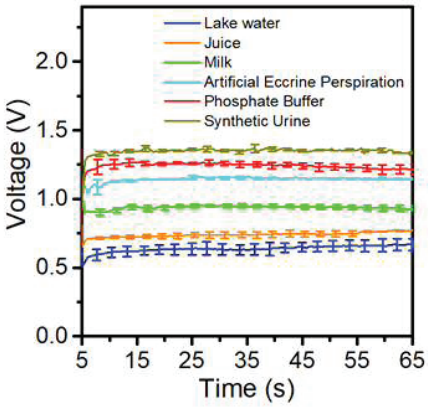

Figure 19. Battery output voltages under continuous operation when measuring real samples. Lines represent mean values, error bars represent ± one standard deviation, for N = 3. (Reprinted with permission from[19]. Copyright 2020 American Chemical Society).

voltage output of the battery recorded at 30 seconds was used in equation (8) to derive the conductivity of the samples.

Finally, the conductivity values measured by the paper battery sensor were compared with those provided with a commercial lab conductometer, 914 pH/Conductometer (Metrohm). Figure 20 shows the Passing-Bablok linear regression comparing the results provided by the paper battery sensor device against the lab conductometer results.

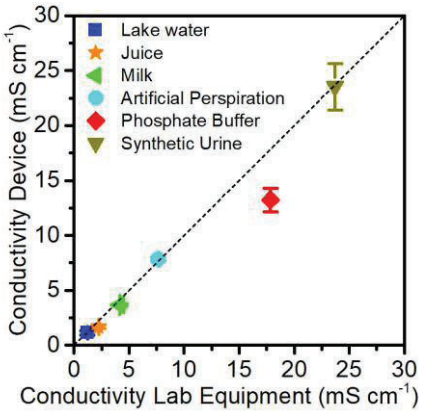

Figure 20. Passing-Bablok linear regression that compares the conductivity values obtained with the paper battery sensor device against the lab reference method. Data points represent mean values, error bars represent ± one standard deviation, for N = 3. (Reprinted with permission from[19]. Copyright 2020 American Chemical Society).

It can be seen that the conductivity values obtained with the paper battery sensor show a good correlation with the values obtained with the reference method except in the case of phosphate buffer, also shown numerically in Table 3.

Table 3. Conductivity values obtained by the paper battery-sensor and the Lab conductometer with the computed relative error

Sampler	**Lab Conductometer ($mS \cdot cm^{-1}$)**	**Conductivity battery-sensor ± SD ($mS \cdot cm^{-1}$)**	**Relative error (%)**
Lake water	1.2	1.1 ± 0.2	8
Juice	2.2	1.7 ± 0.2	23
Milk	4.2	3.8 ± 0.1	9
Artificial perspiration	7.6	7.8 ± 0.2	3
Phosphate buffer	17	13.0 ± 1.0	26
Synthetic urine	24	23.0 ± 2.0	1

The discrepancy is probably due to the interaction of phosphate salts with the magnesium ions released from the anode. Mg^{2+} has high affinity for many anionic salts. Although most of the magnesium salts have a relatively high solubility constant (K_{ps}) in aqueous media, there are a few that precipitate at very low concentrations. In particular, when mixed with carbonates, fluorides, hydroxides, sulfates or phosphates, the resulting magnesium salts form precipitates. In this case, the solubility of Mg^{2+} and PO_4^- corresponds to a K_{ps} of $4 \cdot 10^{-25}$, which reinforces the idea of electrode passivation by magnesium phosphate precipitates that is responsible for the observed deviation in the conductivity measurement of the buffer. The interaction of Mg^{2+} ions released by the anode with some specific anionic components restricts the applicability of the sensor to selected environments. In this sense, our sensor is particularly suited to measure conductivity biological samples where these interfering salts are seldomly present and generally, at ultralow concentrations. However, the interaction of the electrodes with ionic species present in the liquid sample can be further prevented by introducing ion-selective membranes as effective separators.

Conclusions

This chapter presents a novel method to measure fluid conductivity that does not require complex instrumentation or costly setups. In particular, the use of a paper-based battery connected to a single resistor allows to obtain a DC output that is not only easy to interpret with a simple handheld multimeter but is also self-powered, as the battery acts as a sensor and a power source at the same time.

The availability of a battery whose output voltage becomes informative of the conductivity of a sample opens new avenues for self-powered sensing strategies and their application to portable and wearable devices. The connection of a resistor allows obtaining both power (voltage and current) and information about the sample, which is coded in the output voltage of the battery. As it will be shown in the next chapters, there are many ways of translating output voltage to meaningful information about conductivity of the sample by solely using the power generated by the battery sensor.

The self-powered strategy followed in this chapter, connection of a resistor in parallel to the battery, limits the dynamic range of the sensor. As sensitivity decreases at a pace of $1/\sigma$, there is an unavoidable sensor saturation at increasing conductivities. However, there is room to explore new engineering strategies (i.e. operating the cell at fixed voltage in a self-powered mode or connecting a battery stack to obtain multiples of open circuit potential (V_{OCP})) that will allow expanding the sensor dynamic range beyond the values presented in this paper.

Furthermore, the device presented here requires a very small volume to perform the measurement (15 μL) which is significantly smaller than the mL range volumes required by common conductivity probes. This turns to be especially suitable for conductivity measurements of biological samples such as blood, tears or sweat, in which availability of sample volume is very limited. Although theoretically possible, the device cannot be reused in practice. The electrodes undergo irreversible redox reactions that modify their surface and the cell characteristics may be altered from one measurement to the next. Due to its nature, the device has been considered to be single use. However, the simplicity of both materials used and fabrication processes required to develop the sensor allows to envisage its rapid adoption by the booming generation of single use and paper-based analytical devices whenever conductivity measurements are needed.

Finally, the use of magnesium as anodic materials restricts the use of the battery to liquids with very low content of salts with capability of forming precipitates. In this sense, the battery is especially suited to measure biological samples, in which phosphates,

carbonates, etc…are particularly low. Besides, further engineering improvements of the battery can be implemented in order to keep magnesium protected from direct contact with the interfering salts, such as introducing ion-selecting membranes of buffered ion-conducting solutions around this particular electrode,

References

(1) Reddy, T. B. *Linden's Handbook of Batteries*; Mcgraw-hill New York, 2011; Vol. 4.

(2) Kiehne, H. A. *Battery Technology Handbook*; CRC Press, 2003; Vol. 118.

(3) Printed thin and flexible SoftBattery | Enfucell Oy https://www.enfucell.com/ (accessed Sep 30, 2020).

(4) Hilder, M.; Winther-Jensen, B.; Clark, N. B. Paper-Based, Printed Zinc-Air Battery. *Journal of Power Sources.* December 1, 2009. pp. 1135–1141. https://doi.org/10.1016/j.jpowsour.2009.06.054.

(5) Wang, Z.; Meng, X.; Wu, Z.; Mitra, S. Development of Flexible Zinc–Air Battery with Nanocomposite Electrodes and a Novel Separator. *Journal of Energy Chemistry.* January, 2017. pp. 129–138. https://doi.org/10.1016/j.jechem.2016.08.007.

(6) Gonzalez-Guerrero, M. J.; Gomez, F. A. An All-Printed 3D-Zn/Fe3O4 Paper Battery. *Sensors and Actuators B: Chemical.* June 15, 2019. pp. 226–233. https://doi.org/10.1016/j.snb.2019.03.097.

(7) Ferreira, I.; Brás, B.; Correia, N.; Barquinha, P.; Fortunato, E.; Martins, R. Self-Rechargeable Paper Thin-Film Batteries: Performance and Applications. *IEEE/OSA Journal of Display Technology.* August 9, 2010. pp. 332–335. https://doi.org/10.1109/JDT.2010.2056672.

(8) Gonzalez-Guerrero, M. J.; Gomez, F. A. Miniaturized Al/AgO Coin Shape and Self-Powered Battery Featuring Painted Paper Electrodes for Portable Applications. *Sensors and Actuators B: Chemical.* November 10, 2018. pp. 101–107. https://doi.org/10.1016/j.snb.2018.06.016.

(9) Avoundjian, A.; Galvan, V.; Gomez, F. A. An Inexpensive Paper-Based Aluminum-Air Battery. *Micromachines.* July 2017. pp. 222. https://doi.org/10.3390/mi8070222.

(10) Wang, Y.; Kwok, H.; Pan, W.; Zhang, H.; Leung, D. Y. C. Innovative Paper-Based Al-Air Batteries as a Low-Cost and Green Energy Technology for the Miniwatt Market. *Journal of Power Sources.* February 28, 2019. pp. 278–282. https://doi.org/10.1016/j.jpowsour.2019.01.018.

(11) Shen, L. L.; Zhang, G. R.; Biesalski, M.; Etzold, B. J. M. Paper-Based Microfluidic Aluminum-Air Batteries: Toward next-Generation Miniaturized Power Supply. *Lab on a Chip.* September 26, 2019. pp. 3438–3447. https://doi.org/10.1039/c9lc00574a.

(12) Koo, Y.; Sankar, J.; Yun, Y. High Performance Magnesium Anode in Paper-Based Microfluidic Battery, Powering on-Chip Fluorescence Assay. *Biomicrofluidics.* September 5, 2014. pp. 054104 (1-7). https://doi.org/10.1063/1.4894784.

(13) Liu, H.; Crooks, R. M. Paper-Based Electrochemical Sensing Platform with Integral Battery and Electrochromic Read-Out. *Analytical Chemistry.* February 22, 2012. pp. 2528–2532. https://doi.org/10.1021/ac203457h.

(14) Thom, N. K.; Yeung, K.; Pillion, M. B.; Phillips, S. T. “Fluidic Batteries” as Low-Cost Sources of Power in Paper-Based Microfluidic Devices. *Lab on a Chip.* March 14, 2012. pp. 1768–1770. https://doi.org/10.1039/c2lc40126f.

(15) Zhang, X.; Li, J.; Chen, C.; Lou, B.; Zhang, L.; Wang, E. A Self-Powered Microfluidic Origami Electrochemiluminescence Biosensing Platform. *Chemical Communications.* March 19, 2013. pp. 3866–3868. https://doi.org/10.1039/c3cc40905h.

(16) Jr William N Carson, W. H. F. Sea Water-Activated Primary Battery. US3352718A, July 23, 1963.

(17) Koontz, R. F.; Lucero, R. D. Chapter 17 Magnesium Water-Activated Batteries. *Magnesium* 2002, 1–27.

(18) Zhang, T.; Tao, Z.; Chen, J. Magnesium-Air Batteries: From Principle to Application. *Materials Horizons*. March 1, 2014. pp. 196–206. https://doi.org/10.1039/c3mh00059a.

(19) Ortega, L.; Llorella, A.; Esquivel, J. P.; Sabaté, N. Paper-Based Batteries as Conductivity Sensors for Single-Use Applications. *ACS Sensors.* May 20, 2020. pp. 1743–1749. https://doi.org/10.1021/acssensors.0c00405.

(20) King, A. D.; Birbilis, N.; Scully, J. R. Accurate Electrochemical Measurement of Magnesium Corrosion Rates; A Combined Impedance, Mass-Loss and Hydrogen Collection Study. *Electrochimica Acta*. March 1, 2014. pp. 394–406. https://doi.org/10.1016/j.electacta.2013.12.124.

3.

CONDUCTIVITY APPLICATION 1: DEVELOPMENT OF A SELF-POWERED SCALE-BAR CONDUCTOMETER

Overview

In this chapter, we present a practical implementation of a self-powered conductometer device able to analyze low volume liquid samples by applying the sensing principle described in the previous chapter. The device core consists of a stack of two single use paper-based battery sensors. Each battery-sensor unit consists of two electrodes, that have been connected in series internally in the laminated adhesives used as encapsulation as a as a way of increasing the sensitivity and measurement range of the device. As already described in the previous chapter, to operate the system in a self-powered mode a resistive element is connected to the battery stack so its output voltage is directly related to the conductivity of the electrolyte to be analyzed.

Signal management is performed by means of a flexible hybrid circuit fabricated using inkjet printing techniques that requires a minimal number of discrete off-the-shelf electronic components to function. In this sense, the simplicity of the circuit enables its full future printability. It consists of a set of resistors configured as voltage dividers and transistors that are used to discriminate different ranges of conductivities. The energy delivered by the battery allows displaying the result to the user by means of screen-printed electrochromic displays. The device has been calibrated using NaCl samples at different conductivities and finally has been tested to validate its performance with real water samples coming from domestic taps, natural local lakes and the sea.

Introduction

Conductometry is a widely used method employed to monitor the ionic content of a sample the progress of chemical reactions or alterations of the conductivity of liquid samples that reveals information about the consumption or production of charged species. The majority of the reported conductivity sensors are based on an interdigitated electrodes configuration, where the conductivity of a fluid is obtained by means of the measurement electrochemical impedance [1,2]. In this technique, a small sinusoidal signal is applied between two electrochemically inert electrodes, traditionally made of gold or titanium, and the induced current is recorded. Thanks to the proportionality between the applied voltage and the measured current, the impedance characteristics of the sample can be extracted. The dimensions of the electrodes as well as the gap between them defines the cell constant of the device and has a strong impact on the sensitivity of the sensor[3,4]. Conductivity sensors have a wide range of applications and utilities in different fields. One of the first approaches was to determine the urea concentration in solutions by a conductivity cell bridge[5]. In this case, the urea was measured by monitoring the conductivity inside a solution where an enzyme-catalyzed reaction was taking place destroying the urea protein with urease and producing charged species. The same method has also been used to directly monitor the changes in conductance of an electrode as a result of the immobilization of complementary antibody-antigen pairs, DNA or whole cells[6–9]. Another important application is related to water resources, conductivity reveals information about the quality of water, if it is drinkable or it can be dangerous for human health, and about the ionic composition which is important for irrigation[10].

As an evolution of the electrochemical impedance spectroscopy the tetrapolar impedance sensing has been well established in the field of biosening. This method involves four electrodes, two are used for current injection and the other two allow measuring the voltage response. The tetrapolar impedance configuration allows to increase the accuracy of the conductivity values as can be related entirely with the analyte properties as the electrode impedance contribution to the measurement is eliminated[11].

Apart from the technique presented above different alternative methods to measure the conductivity of a sample have been developed, on the last years the ISFET (Ion-Selective Field-Effect Transistors) and EnFET (Enzyme Field-Effect Transistors) have been demonstrated to be a viable alternative to EIS. FET transistors use an electrical field to control the conductivity of a channel between two electrodes. Functionalizing the gate (the third electrode which connects the two previous mentioned) researchers have been developing different sensors such as pH-sensitive, penicillin, glucose or urea[12–14].

However, these devices require a stable and reliable reference electrode, which in most of the cases prevents their application in real scenarios. Their limited selectivity is also a drawback.

Conductometers using EIS are a very mature product, which can be found in the market to be used in different applications from laboratory analysis to quality control for irrigation. More specifically, portable conductometers have been evolving to match different requirements as sensibility, user-friendliness, amount of sample required, impermeability or reusability among others. In Figure 1 it is shown some images of different portable conductometers.

In this section, we present the implementation of a functional self-powered conductometer that uses the already explained battery-sensor principle to measure the conductivity of water samples from different nature, avoiding the use of bulky instrumentations to perform the conductivity measurement. The prototype consists in a single use self-powered device that allows to measure ionic conductivity of a fluid with a very simple strategy. In particular, we propose to use the basic unit presented before to sense ionic conductivity by using the liquid to be sensed as battery electrolyte, which will power the entire electronic system implemented on a flexible hybrid inkjet printed circuit with screen-printed electrodes to show the result. With this device a low cost alternative is presented and due to the minimal electronics approach followed in the implementation of this device, this self-powered conductometer pretends to be a more sustainable solution compared with the already conductometers commercially available.

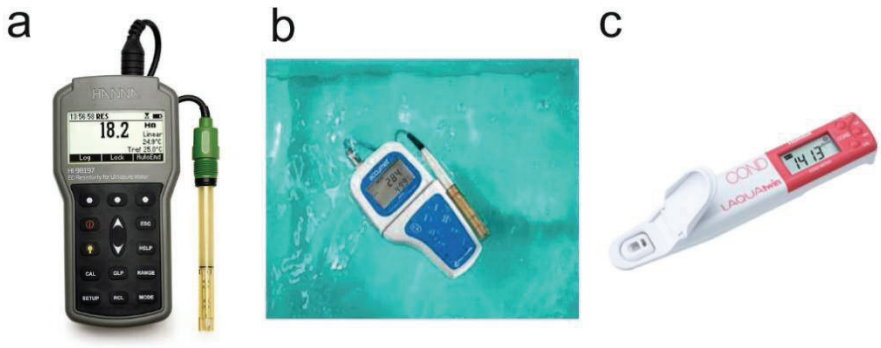

Figure 1. Portable conductometers a) Conductometer for ultrapure water from Hanna Instruments[15] b) Water conductometer for field applications from Thermo Fisher Scientific[16] and c) Small-volume conductometer from Horiba[17]

Results and discussion

Battery stack sensing capabilities

In this section, we describe the implementation of a battery stack that allowed increasing the dynamic range and the sensitivity of the single paper-based conductivity battery sensor disclosed in the previous chapter.

Figure 2 shows the exploded vision of the laminates used to build the battery stack and Figure 3 the final fabricated paper-battery stack. The battery stack was designed with CorelDRAW. Were mounted vertically with different pressure sensitive adhesive (PSAs) as substrates and cut with a CO_2 laser. The battery stack electrodes were obtained directly cut from a commercial magnesium sheet in the case of the anode and screen-printed over a PET substrate, cured and cut in the case of the silver/silver chloride cathode. Manufacturing details are specified in the previous chapter. During the battery stack mounting, the electrodes were connected internally in series.

The calibration of the battery stack was performed by wetting the paper cores of both batteries simultaneously with NaCl solutions with conductivities ranging from 0.5 mS cm^{-1} to 5 mS cm^{-1}. The NaCl solutions were prepared daily and the conductivity was measured for all the experiments with the 914 pH/Conductometer from Metrohm. The characterization of the battery stack was done with the Autolab Potentiostat PGSTAT204

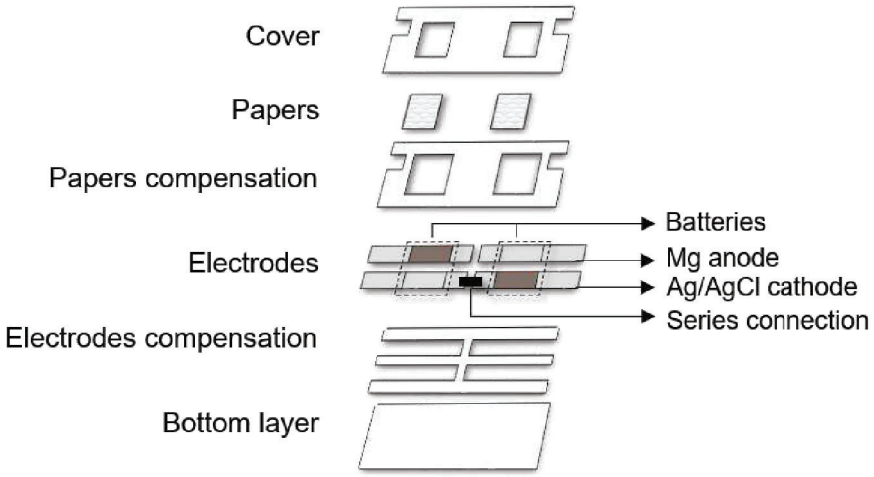

Figure 2. Exploded vision of layers and the main elements inside the battery stack.

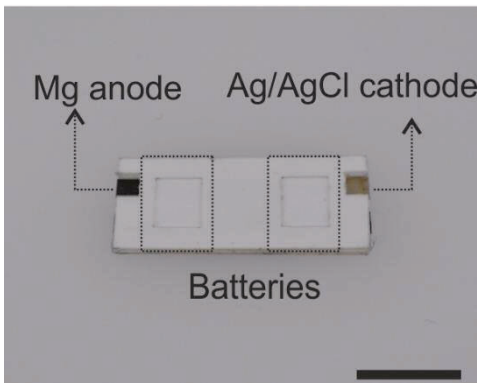

Figure 3. Fabricated paper-based battery stack (scale bar = 1 cm).

also from Metrohm by using the same methods used for the characterization of the single conductivity battery sensor. The open circuit potential (V_{OCP}) of the stack was measured during 10 seconds and then a Linear Sweep Voltammetry (LSV) was performed at 20 mV s^{-1} from V_{OCP} to 0 V, as shown in Figure 4.

One of the advantages of this sensor is that it can be operated in a very simple way by connecting a resistor (R_{LOAD}) in series with the battery stack. Under this configuration, the output voltage of the battery can be directly related to the conductivity of the liquid poured inside its glass fibre core. The selection of the resistor value is a key step in the implementation of the device. To achieve the maximum sensitivity of the battery

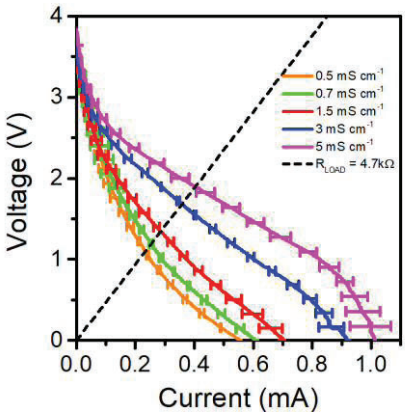

Figure 4. Polarization curve of the paper-based battery stack when analysing samples from 0.5 $mS \cdot cm^{-1}$ to 5 $mS \cdot cm^{-1}$ (solid lines) and a theoretical R_{LOAD} connected in series to the stack (dashed line). Lines represent mean values, error bars represent ± one standard deviation, for N = 3.

performance at a given conductivity, the optimal R_{LOAD} to be connected must have the same value as the internal resistivity of battery at that particular conductivity, the mathematical demonstration of this phenomenon can be found in the previous chapter. Because the intended use of this device is to measure different water samples to assess the suitability for crop irrigation, the risk of damaging the crop as a function of the conductivity of the water is very important. As stated by the FAO (Food and Agricultural Organization) irrigation water must accomplish different requirements depending on the tolerance of soils to salinity[18,19]. Taking into account sensitive crops, the risk of irrigation can be classified as specified in Table 1.

Table 1. Risk of crop damage as a function of conductivity of water for irrigation

Risk of damage	**Conductivity (mS cm^{-1})**
No risk	$\sigma < 0.7$
Low risk	$0.7 < \sigma < 1.5$
Moderate risk	$1.5 < \sigma < 3$
High risk	$\sigma > 3$

For the implementation of the device it was decided to maximize the sensitivity of No risk samples, due to is also the typical conductivity of drinkable water. During the calibration of the device, when adding a NaCl samples of 0.7 mS cm^{-1} the internal resistance of the battery corresponded to 4.7 kΩ (obtained from the slope of the polarization curve at its ohmic region at that particular electrolyte conductivity). Figure 5 shows the voltage delivered by the battery stack at the intersection of the polarization curves depicted in Figure 4 with the selected R_{LOAD} of 4.7 kΩ represented with a black dashed line.

Intersecting the resistor with the polarization curves obtained when characterizing the battery allows obtaining a preliminary calibration curve of the self-powered sensor and predicting the sensitivity of the dynamic range of the battery sensor. However, the calibration curve has to be refined by measuring the actual battery voltage when activated with the solution to be measured and then directly connected to the R_{LOAD} in series. First, the battery stack was led to stabilized for approximately 5 seconds. Then, the R_{LOAD} of 4.7 kΩ was connected and the battery voltage evolution was recorded during 60 seconds with an HP34401A Multimeter and a custom-made LabVIEW program. Figure 6 shows the voltage values recorded with different calibration solutions.

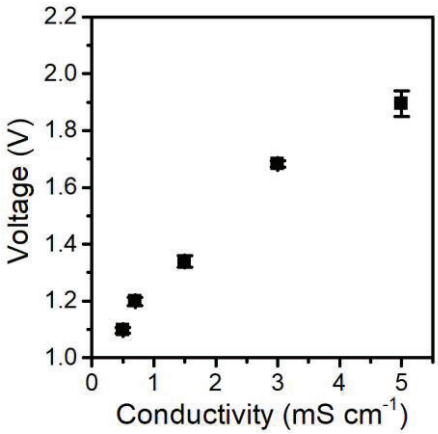

Figure 5. Theoretical voltage output of the paper-based battery stack at different electrolyte conductivities when connecting a resistor of 4.7 kΩ in series. Data points represent mean values, error bars represent ± one standard deviation, for N = 3.

It can be observed that the voltage values are stable along the measurement except from the experiments with 0.5 and 0.7 mS cm^{-1} where the voltage tends to increase in time. This voltage increase is due to the progressive removal of a native passivation layer on the surface of the magnesium electrode, which is progressively being consumed during the measurement (this is known as the pitting effect of chloride ions in the magnesium

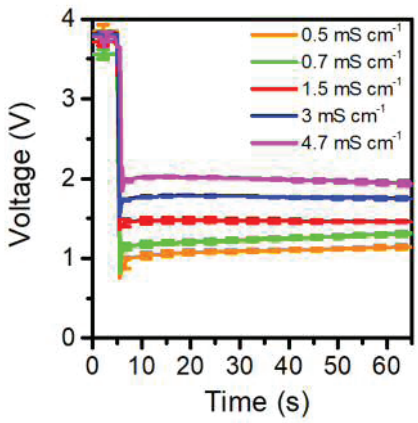

Figure 6. Voltage signal provided by the battery stack when introducing different NaCl samples with conductivities from 0.5 to 5 mS cm^{-1} and connecting the 4.7 kΩ resistor. Lines represent mean values, error bars represent ± one standard deviation, for N = 3.

electrode already disclosed in the literature[20]). At higher conductivities, this effect is practicably negligible, as the passivation layer is removed during the first few seconds. Figure 7 allows comparing the voltage output of the battery after 30 seconds of operation with the output voltage predicted in Figure 5 from the LSV.

The voltage discrepancies observed in Figure 7 that are also depending on the conductivity are due to the fact that the electrodes of the battery sensor are consumed at different rates depending on the operation time and generated charge. The polarization curve is a method that scans the battery from the V_{OCP} to 0 V at a predetermined scan rate and forces the battery to deliver increasing current densities until the voltage drops to zero, whereas in the case of fixing a constant load, the battery delivers a constant current that depends on the internal resistivity of the battery assembly. This situation leads to different scenarios depending on the conductivity being analysed. At low conductivities the voltage presented by the intersection between the polarization curve and the R_{LOAD} is higher than the one obtained by the transient characterization under the R_{LOAD}. This is because in the ohmic region of the polarization curve, the passivating layer is already removed but it is still present during the measurement of the transient response (30 seconds from the connection of the resistor). On the other hand, at high conductivities, in the intersection of the polarization curve with the resistor. The measured voltage is underestimated due to the consumption of the electrodes at this high current conditions. During the measurement

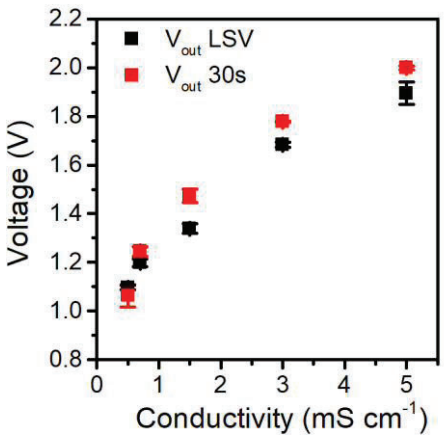

Figure 7. Comparison between the voltage of the battery stack from the characterization with the Linear Sweep Voltammetry (LSV) and the voltage obtained after connecting the resistor in series for 30 seconds. Data points represent mean values, error bars represent ± one standard deviation, for N = 3.

with the resistor in series, the voltage obtained is higher than the one predicted in the LSV because the electrodes have not been severely degraded during these firsts 30 seconds of transient operation of the battery.

The voltage output of the calibration curve of the battery sensor shown in Figure 7 with red squares was fitted to expression (1) that relates the voltage output of the battery with its open circuit potential V_{OCP}, the value of the resistive load R_{LOAD}, the conductivity of the electrolyte σ and the cell constant k, a geometrical factor related with the electrode configuration. The term V_0 accounts for the voltage delivered by the battery when operated with deionized water (0.80 V), whereas V_{OCP}^* corresponds to an effective value of the open circuit potential of the battery where the activation losses have been subtracted. Details about how expression (1) is derived can be found in the previous chapter.

$$V_{out} = \frac{V_{OCP}^{*} \cdot R_{LOAD}}{\frac{k}{\sigma} + R_{LOAD}} + V_0 \qquad (1)$$

Figure 8 shows the result of fitting the experimental values to eq. (1) and so defining the system calibration curve. Table 2 summarizes the values of the fitted parameters obtained with an Adjusted R-Squared of 0.99.

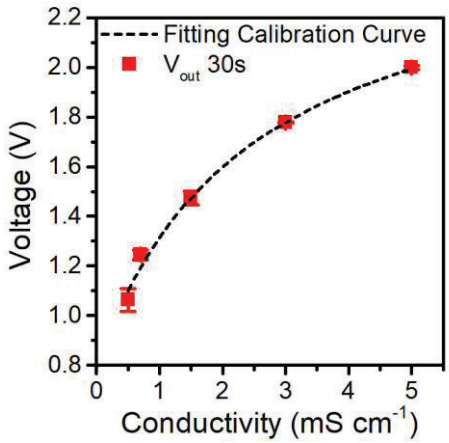

Figure 8. Non-linear curve fitting of the battery stack behaviour and the defined levels to build the self-powered conductivity sensor. Data points represent mean values, error bars represent ± one standard deviation, for N = 3.

Table 2. Fitted parameters of the battery stack voltage output

Parameter	Value	Standard Error
k	11.6	0.91
V_{OCP}*	1.78	0.06

Therefore, the calibration curve of the battery stack corresponds to expression (2).

$$V_{out} = \frac{1.78\ V \cdot 4.7\ k\Omega}{\frac{11.6\ cm^{-1}}{\sigma} + 4.7\ k\Omega} + 0.8\ V \qquad (2)$$

Circuit design, implementation and characterization

After obtaining the sensor calibration, we tackled the development of a self-powered conductometric device able to discriminate among four different conductivity ranges. For result visualization, electrochromic displays were identified as the most suitable technology due to their compatibility with flexible substrates, their fabrication with screen-printing techniques and their capability to operate with low voltages. In this case, a custom-made electrochromic display with 4 segments from Ynvisible (Portugal) was used. An image of the electrochromic display used for the implementation is shown in Figure 9.

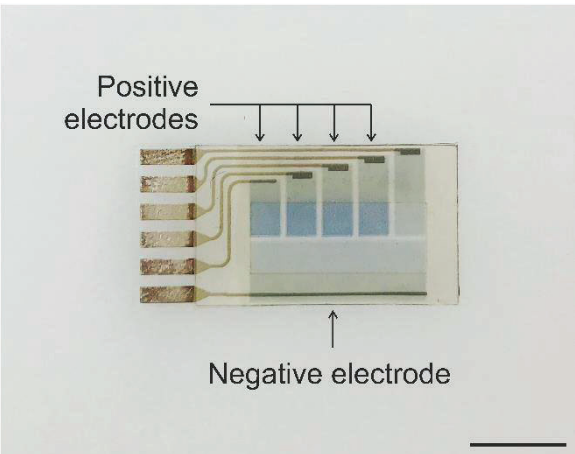

Figure 9. 4 Segments electrochromic display from Ynvisible (scale bar = 1 cm).

With the transfer function of the battery stack and the aim of implementing devices with the minimum number of components, the circuit was designed using only passive elements such as resistors, diodes, capacitors and transistors, which has been demonstrated in the literature feasible to be implemented using organic printed electronic techniques.

As the battery output voltage provides direct information about the conductivity of the sample, we decided to implement a minimalistic voltage level-discriminating module as basic unit that would turn on an electrochromic display when a predetermined voltage of the battery (V_{level}) is reached. Figure 10 shows the schematic of the basic unit.

The unit is composed of two NMOS transistors connected in a Darlington-like configuration that allows increasing the voltage gain. Under this configuration, the transistor T_1 is set in conduction mode when its voltage gate exceeds 0.8 V. In order to ensure that the battery is operated at its optimal R_{LOAD}, the equivalent resistance of the circuit seen has to be maintained around 4.7 kΩ. This is being achieved by setting the appropriate values to resistors R_A and R_B, as these two elements account for the overall impedance of the system when T_1 and T_2 are in off state. Moreover, R_A and R_B values are responsible of setting T_1 in conduction mode when V_{level} is surpassed by the battery, as they work as a voltage divider. This means that:

$$R_A = R_B \cdot \frac{V_{level} - V_{Threshold\ T1}}{V_{Threshold\ T1}} \quad (3)$$

When $V_{battery} > V_{level}$, transistor T_1 switches on and allows current to flow through R_C. Upon the activation of T_1 and T_2, in order to prevent the overall impedance of the unit change significantly, R_C is set to be at least 100 times higher than R_A+R_B. This strategy has the

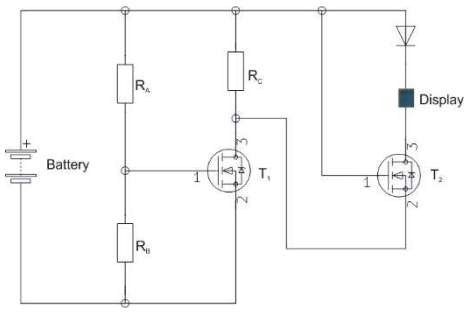

Figure 10. Single voltage level-discriminating unit.

additional advantage of setting T_2 to on state automatically, and the electrochromic display is switched on. By changing the portion of the voltage divider with different values of R_A and R_B and defining different V_{level}, several units can be placed in parallel to the battery-sensing stack to enable a scale-bar that quantifies the conductivity of a fluid by lightening one to several electrochromic display segments, shown in Figure 11.

Figure 12 shows the schematic of the electronic circuit implemented in the device. It has been designed with three different enabling units to allow discrimination among four conductivity levels.

The circuit is composed of five different blocks that are all connected in parallel to the sensing battery stack. The first block consists of an electrochromic display that is used to

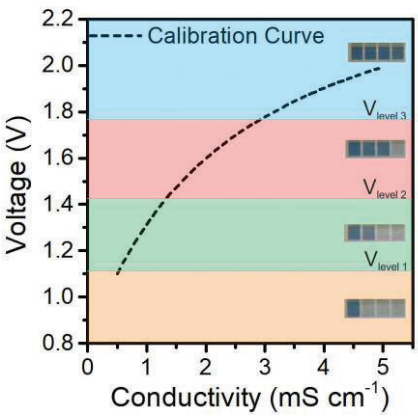

Figure 11. Representation the battery stack calibration curve and the voltage levels implemented to switch on one to four electrochromic display segments by introducing different enabling units in parallel.

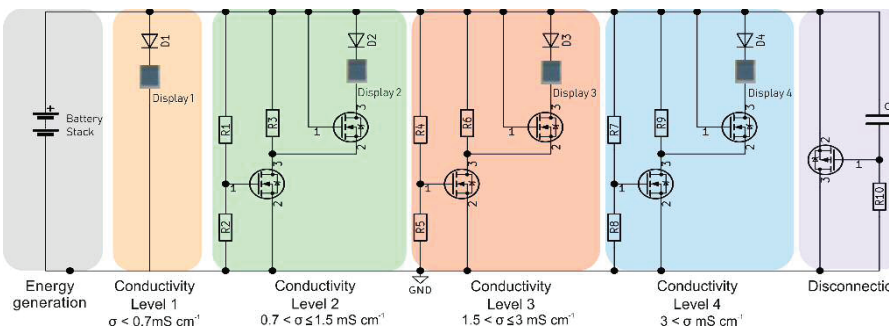

Figure 12. Schematic of the circuit with the six implemented blocks.

both inform about the correct functioning of the battery once activated with the fluid to be measured and accounts also for the first conductivity level. The electrochromic display lights on when the applied voltage surpasses 0.8V, as the battery delivers a minimum voltage of 0.8V (when activated with deionized water). As the electrochromic displays are reversible and suffer from self-discharge over time, a diode was added in series to all the displays so the charge stored can be kept for a long time. The next three blocks are voltage-level discriminating units that are set to light the different displays when the conductivity of the sample exceeds 0.7 mS cm^{-1}, 1.5 mS cm^{-1} and 3.0 mS cm^{-1} respectively. These ranges have been selected as an illustrative application example and correspond to the different levels of interest typically used to classify water suitability for human and animal ingestion and crop irrigation. Finally, the last block shown in Figure 12 has been labelled as disconnection block and it is responsible of short-circuiting the battery after a pre-set measurement time. This block was added to limit the time during which the circuit is measuring the battery sensor output and avoid recording undesired voltage drifts caused by liquid evaporation. The disconnection block is composed of a highly resistive element R_{10} (1 MΩ), a relatively small capacitor (22 μF) and a PMOS transistor. When the battery stack starts to operate, the capacitor starts charging at a rate that is limited by the current flowing through R_{10}. When the capacitor voltage reaches the threshold voltage of the transistor gate, the transistor switches from a cut-off state to a forward active state that sets the battery in a short circuit and makes its voltage drop down to zero. The time elapsed in the process depends also on the current provided by the battery which at the same time depends on the conductivity of the sample that is being measured. High conductivity samples provide large currents that lead to fast charging processes whereas samples below 1 mS·cm^{-1} deliver low current densities. Figure 13 shows the characterization of the disconnection module while using different NaCl solutions with conductivities ranging from 0.7 mS cm^{-1} to 5 mS cm^{-1} as batteries electrolyte.

It can be seen that at 0.7 mS·cm^{-1} the measurement time extends up to 25 seconds. The fact that at lower conductivities the measurement time is extended turns to be very beneficial. The battery is operated during a sufficient time for the magnesium passivation removal and voltage stabilization, which leads to better compliances at low conductivity ranges.

The resistors of the circuit were adjusted to allow the discrimination of the four conductivity levels taking into account the output voltages from the calibrated battery stacks (eq. 2) at the pre-defined threshold level conductivities, 0.7 mS cm^{-1}, 1.5 mS cm^{-1} and 3 mS cm^{-1}. Table 3 summarizes the resistors values.

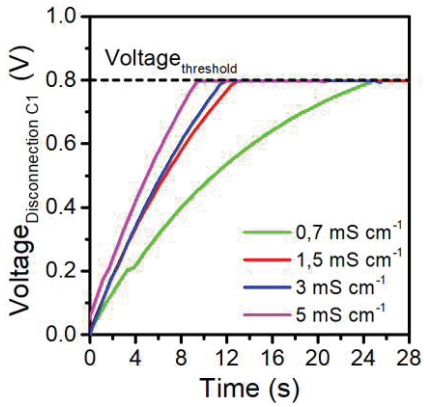

Figure 13. Voltage evolution in the disconnection module depending on the conductivity of the sample of the electrolyte.

Table 3. Resistor values used to implement the circuit

Parameter	**Value**
R_1	1 kΩ
R_2	3.9 kΩ
R_3	1 MΩ
R_4	300 kΩ
R_5	650 kΩ
R_6	1 MΩ
R_7	750 kΩ
R_8	750 kΩ
R_9	1 MΩ
R_{10}	1 MΩ

The operation of the circuit was tested on a protoboard connecting externally the paper-based battery stack. The liquid sample was introduced simultaneously in both batteries and then the voltage provided by the battery stack after activation and the voltage being

recorded in the different electrochromic displays were measured. Figure 14 shows the transient response of the battery during the first 25 seconds, which was sufficient to perform all the measurements and set the battery in short-circuit conditions.

As expected, the operating time of the device was different depending on the conductivity. Note that after disconnection, the final voltage of the battery drops to 0.7 V, which corresponds to the built-up voltage of the transistor internal diode. Figure 15 shows the

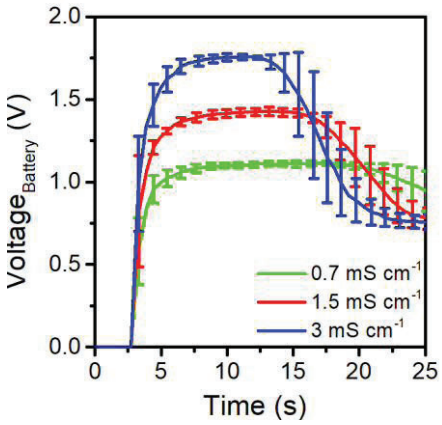

Figure 14. Voltage of the battery when introducing NaCl samples with 0.7, 1.5 and 3 mS cm^{-1}. Lines represent mean values, error bars represent ± one standard deviation, for N = 3.

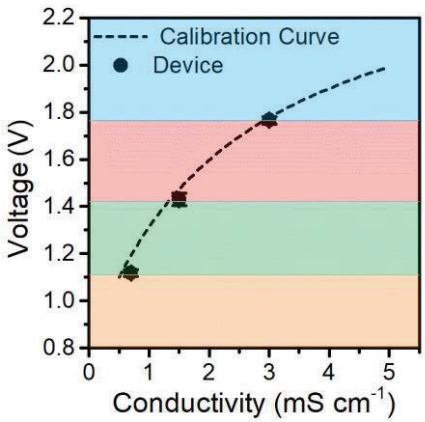

Figure 15. Extracted maximum voltage provided by the battery stack as a function of the conductivity of the electrolyte compared with the calibration curve from equation (2). Data points represent mean values, error bars represent ± one standard deviation, for N = 3.

value of the maximum voltages achieved by the battery during circuit operation compared to the calibration curve governed by equation (2).

As it can be observed, the paper-based battery stack presents a high repeatability when sensing the conductivity of a fluid, with coefficients of variation not higher than 2% (shown in Table 4), and the maximum voltage achieved by the battery during its operation matches almost perfectly with the governing equation (2).

Table 4. Battery maximum voltages when analysing 0.7, 1.5 and 3 mS cm^{-1}.

Conductivity (mS·cm^{-1})	**Maximum Voltage (V)**	**Standard Deviation (V)**	**Coefficient of Variation (%)**
0.7	1.12	0.01	1
1.5	1.43	0.03	2
3	1.77	0.02	1

When operating the device in the protoboard, allowed to monitor the voltage the different electrochromic displays as shown in Figures 16. For clarity purposes, a dashed line at 0.8V has been depicted in the figure. When the applied voltage at the display terminals exceeded this value, the display turned from faint to dark blue, showing a positive result.

As it can be observed, the system reacted as expected. The first electrochromic display turns on in all the situations as it indicates the correct functioning of the circuit and indicating that the conductivity surpasses the 0.5 mS·cm^{-1}. At a conductivity of 0.7 mS cm^{-1} the two first electrochromic displays were activated indicating that the conductivity of the sample was equal or greater than 0.7 mS cm^{-1}. Likewise, samples of 1.5 mS cm^{-1} and 3 mS cm^{-1} activated three and four electrochromic displays respectively.

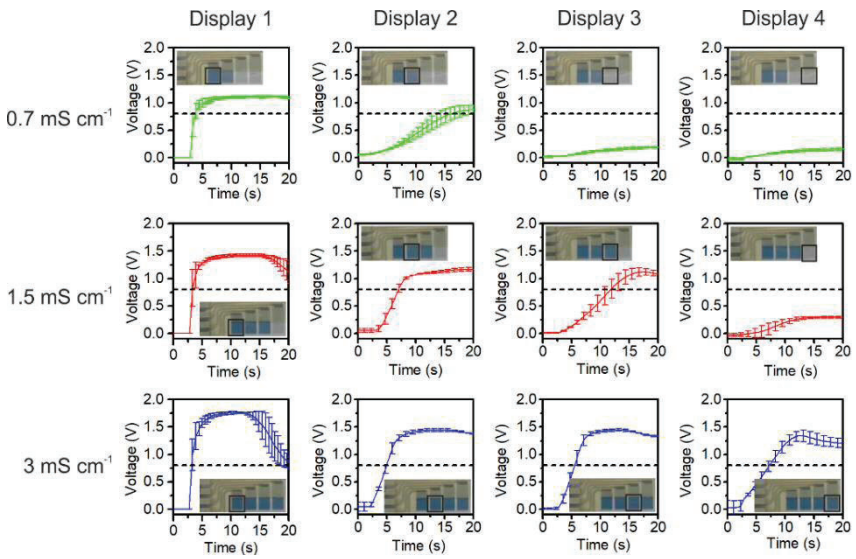

Figure 16. Voltage registered at every electrochromic displays when introducing a NaCl sample of 0.7 mS cm^{-1} (green lines), 1.5 mS·cm^{-1} (red lines) and 3 mS·cm^{-1} (blue lines). The electrochromic display threshold voltage to be switched on is represented with a black dashed line. Measured display segment is framed with a black solid line. Lines represent mean values, error bars represent ± one standard deviation, for N = 3.

Conductometer fabrication and validation

Once the conception of the device was validated on a protoboard, the hybrid circuit was fabricated. The conducting tracks of the circuit were inkjet printed with a commercial silver ink on a flexible polyethylene naphthalate (PEN) substrate. Then, the paper battery stack, the discrete SMD electronic components and the electrochromic displays were mounted and hybridized using a silver-based conducting adhesive ink. Finally, the system was encapsulated on a dedicated PMMA casing. All the components of the self-powered conductometer device are shown in Figure 17 and the final assembly of the device is presented in Figure 18.

The device was tested using tailored NaCl samples with 0.5 mS cm^{-1}, 1 mS cm^{-1}, 2 mS cm^{-1} and 5 mS cm^{-1} with the aim of verifying that the device is able to correctly determine conductivity values yielding at the four pre-defined conductivity ranges. As in the previous calibration, the paper-based battery stack voltage was monitored along the experiment (see Figure 19), as well as the voltage evolution at the electrochromic displays, which confirmed the correct performance of the device, Figure 20a-d.

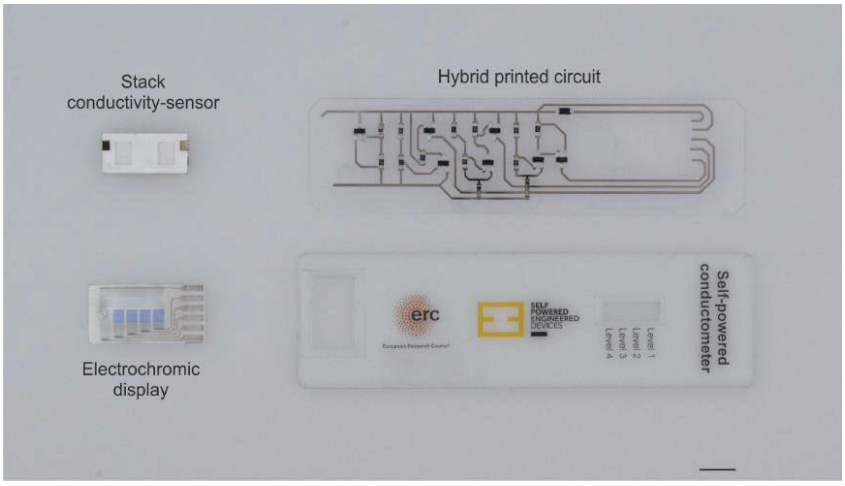

Figure 17. Exploded vision of the self-powered conductometer with all its parts (scale bar = 1 cm).

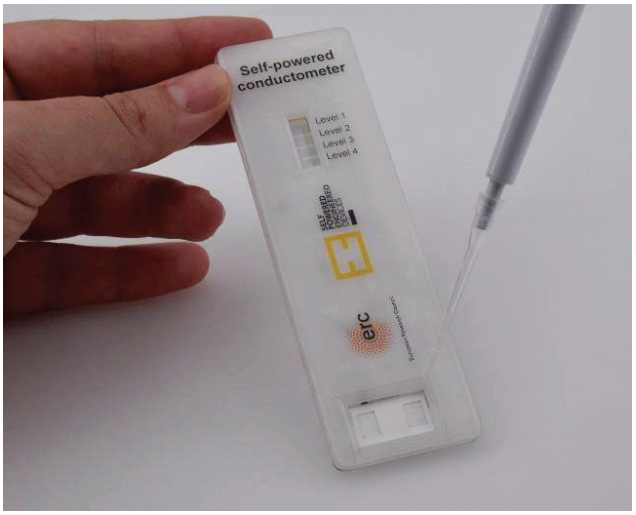

Figure 18. The final self-powered conductometer.

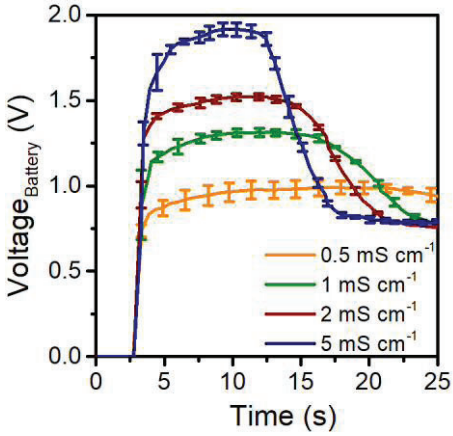

Figure 19. Battery stack voltage evolution during the validation of the device using conductivities from 0.5 to 5 mS·cm^{-1}. Lines represent mean values, error bars represent ± one standard deviation, for N = 3.

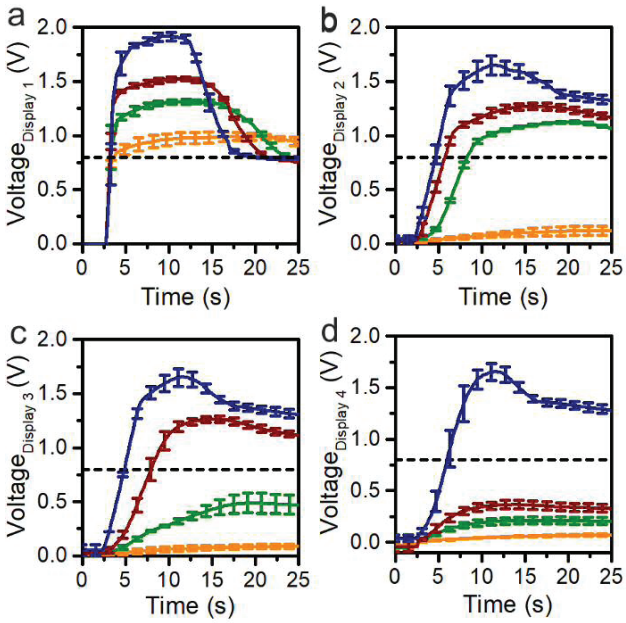

Figure 20. Voltage recorded at the displays during the validation of the device when analysing 0.5 mS·cm^{-1} (orange lines), 1 mS·cm^{-1} (green lines), 2 mS·cm^{-1} (red lines) and 5 mS·cm^{-1} (blue lines). The black dashed lines represent the electrochromic display threshold voltage to be switched on. Lines represent mean values, error bars represent ± one standard deviation, for N = 3.

Figure 21 shows the maximum output voltage achieved by the battery during the measuring interval compared with battery-sensor transfer function, equation (2), represented with a black dashed line.

The experimental voltage values obtained from the validation of the device are slightly lower than the ones recorded during the battery stack calibration, probably due to the fact that the equivalent impedance of the ink-jet printed circuit is a little bit higher than the 4.7 kΩ resistor for calibration. Although this slight difference, it is demonstrated the device capacity of classifying the sample conductivities deposited inside the paper-core of the device. In addition, it is shown the accuracy of the paper-based battery-sensor to provide and output maximum voltage directly related to the electrolyte conductivity according to equation (2). Table 5 shows the actual values presenting a coefficient of variation of the measurements less than a 5%.

Finally, the device performance was tested with three samples of water: tap water (0.55 $mS \cdot cm^{-1}$), lake water (1.16 $mS \cdot cm^{-1}$) and sea water (37.22 $mS \cdot cm^{-1}$). First, the conductivity of the water samples was measured with the lab 914 pH/Conductometer. Afterwards, the samples were introduced inside the device, which lighted the corresponding displays according to the sensed conductivity. Figure 22 shows the experiment performed for each water sample and Figure 23 shows the obtained results.

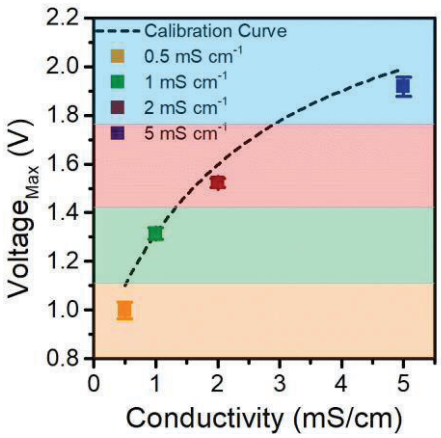

Figure 21. Maximum voltage of the battery when analysing 0.5 $mS \cdot cm^{-1}$ (orange lines), 1 $mS \cdot cm^{-1}$ (green lines), 2 $mS \cdot cm^{-1}$ (red lines) and 5 $mS \cdot cm^{-1}$ (blue lines) following the calibration curve behaviour. Data points represent mean values, error bars represent ± one standard deviation, for N = 3.

Table 5. Battery maximum voltages when analysing 0.5, 1, 2 and 5 mS cm^{-1}.

Conductivity ($mS \cdot cm^{-1}$)	Maximum Voltage (V)	Standard Deviation (V)	Coefficient of Variation (%)
0.5	0.99	0.03	3
1	1.31	0.02	2
2	1.52	0.02	1
5	1.92	0.04	2

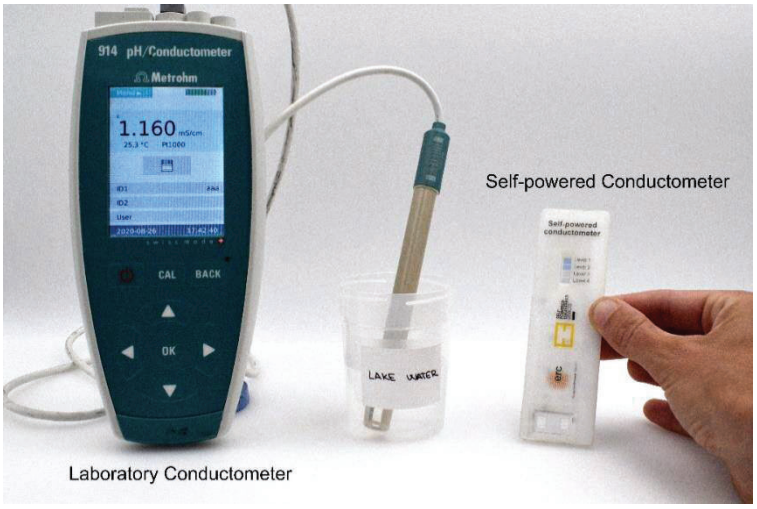

Figure 22. Image of the experimental setup used to compare the results obtained with a laboratory conductometer and the self-powered conductometer.

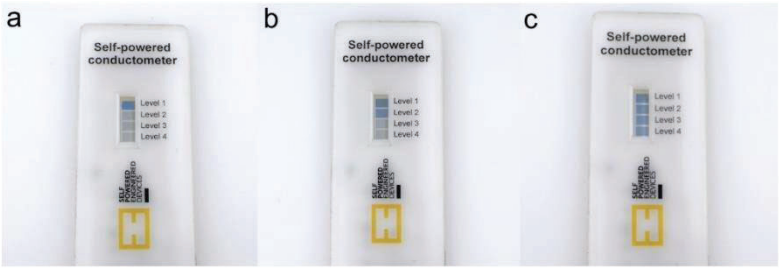

Figure 23. Image of the three results obtained with the self-powered conductometer measuring a) tap water, b) lake water and c) sea water.

It can be seen that the single use conductometer was capable of classifying the different samples in the right conductivity ranges and show clear, easy to read results to the user.

Conclusions

This chapter presents the realization of a fully operative self-powered single-use conductometer which is based on the battery sensor described in the previous chapter. It was demonstrated how this approach is particularly suitable to analyze very small liquid samples (below 100 µL). The device presented here required 35 µL to perform a digital and semi-quantitative measurement of conductivity in a range that comprises from 0.5 to 40 $mS \cdot cm^{-1}$ in a very simple way, avoiding expensive, bulky and sophisticated external equipment. As a particular example, the electronic circuit used to drive the battery signal has been designed to assess water suitability for human and animal ingestion and crop irrigation. However, the design flexibility of the presented approach allows tuning both the number of discrimination levels and the values ranges to be detected in a very simple manner. In order to leverage the advantages of the system, a hybrid electronic circuit was fabricated using low cost and environmentally friendly manufacturing techniques that could be finally be implemented using organic printed electronics. This first device realization demonstrates the convenience of combining techniques such as inkjet printing, lamination of substrates and self-powered strategies to obtain a fully functional single use device with the capability of fulfilling the degree of affordability and sustainability required for its future deployment in real case scenarios.

Note that the dual use of the battery as a sensor and a power source renders the system energetically independent, which is one of the main hurdles of a single-use device. The minimum power generated by the battery is 1 mW, which is dissipated almost entirely in the resistive elements in the current circuit design. In a more sophisticated version, this power could be used to enable communication or data storage functions which certainly would boost the performance of the device.

References

(1) Gan, T.; Shi, Z.; Sun, J.; Liu, Y. Simple and Novel Electrochemical Sensor for the Determination of Tetracycline Based on Iron/Zinc Cations-Exchanged Montmorillonite Catalyst. *Talanta*. April 2014. pp. 187–193. https://doi.org/10.1016/j.talanta.2014.01.002.

(2) Arshak, K.; Moore, E.; Lyons, G. M.; Harris, J.; Clifford, S. A Review of Gas Sensors Employed in Electronic Nose Applications. *Sensor Review*. June 1, 2004. pp. 181–198. https://doi.org/10.1108/02602280410525977.

(3) Olthuis, W.; Streekstra, W.; Bergveld, P. Theoretical and Experimental Determination of Cell Constants of Planar-Interdigitated Electrolyte Conductivity Sensors. *Sensors and Actuators B: Chemical.* March 1995. pp. 252–256. https://doi.org/10.1016/0925-4005(95)85053-8.

(4) Van Gerwen, P.; Laureyn, W.; Laureys, W.; Huyberechts, G.; Op De Beeck, M.; Baert, K.; Suls, J.; Sansen, W.; Jacobs, P.; Hermans, L.; Mertens, R. Nanoscaled Interdigitated Electrode Arrays for Biochemical Sensors. *Sensors and Actuators B: Chemical.* June 25, 1998. pp. 73–80. https://doi.org/10.1016/S0925-4005(98)00128-2.

(5) Cullen, D. C.; Sethi, R. S.; Lowe, C. R. Multi-Analyte Miniature Conductance Biosensor. *Analytica Chimica Acta.* August 21, 1990. pp. 33–40. https://doi.org/10.1016/S0003-2670(00)86394-1.

(6) Brosel-Oliu, S.; Mergel, O.; Uria, N.; Abramova, N.; Van Rijn, P.; Bratov, A. 3D Impedimetric Sensors as a Tool for Monitoring Bacterial Response to Antibiotics. *Lab on a Chip.* February 20, 2019. pp. 1436–1447. https://doi.org/10.1039/c8lc01220b.

(7) Lei, Y.; Chen, W.; Mulchandani, A. Microbial Biosensors. *Analytica Chimica Acta.* January 18, 2006. pp. 200–210. https://doi.org/10.1016/j.aca.2005.11.065

(8) Katz, E.; Willner, I. Probing Biomolecular Interactions at Conductive and Semiconductive Surfaces by Impedance Spectroscopy: Routes to Impedimetric Immunosensors, DNA-Sensors, and Enzyme Biosensors. *Electroanalysis.* July 8, 2003. pp. 913–947. https://doi.org/10.1002/elan.200390114.

(9) Pei, R.; Cheng, Z.; Wang, E.; Yang, X. Amplification of Antigen-Antibody Interactions Based on Biotin Labeled Protein-Streptavidin Network Complex Using Impedance Spectroscopy. *Biosensors and Bioelectronics.* August 2001. pp. 355–361. https://doi.org/10.1016/S0956-5663(01)00150-6.

(10) Silva, J. L. de A.; Mesquita, T. C. R.; Aires, U. R. V.; Silva, D. D. da. Spatial Variability of Water Electrical Conductivity and Its Implications for Agricultural Planning. *Journal of Irrigation and Drainage Engineering.* September 28, 2019. pp. 05019010 (1-8). https://doi.org/10.1061/(ASCE)IR.1943-4774.0001424.

(11) Hantschke, M.; Sideris, D.; Panayiotis Kyriacou, A.; Triantis, A. I. F. Optimization of Tetrapolar Impedance Electrodes in Microfluidic Devices for Point of Care Diagnostics Using Finite Element Modeling. *Proceedings of Annual International Conference of the IEEE Engineering in Medicine and Biology Society*. July, 2018. pp. 5321–5324. https://doi.org/10.1109/EMBC.2018.8513467.

(12) Lue, C. E.; Yu, T. C.; Yang, C. M.; Pijanowska, D. G.; Lai, C. S. Optimization of Urea-EnFET Based on Ta2O5 Layer with Post Annealing. *Sensors.* April 27, 2011. pp. 4562–4571. https://doi.org/10.3390/s110504562.

(13) Luo, X. L.; Xu, J. J.; Zhao, W.; Chen, H. Y. A Novel Glucose ENFET Based on the Special Reactivity of MnO2 Nanoparticles. *Biosensors and Bioelectronics*. May 15, 2004. pp. 1295–1300. https://doi.org/10.1016/j.bios.2003.11.019.

(14) Chin, Y. L.; Chou, J. C.; Sun, T. P.; Chung, W. Y.; Hsiung, S. K. A Novel PH Sensitive ISFET with on Chip Temperature Sensing Using CMOS Standard Process. *Sensors and Actuators B: Chemical*. June 1, 2001. pp. 582–593. https://doi.org/10.1016/S0925-4005(01)00639-6.

(15) HI-98197 Professional Waterproof Meter for Ultrapure Water https://www.hannainstruments.co.uk/hi-98197-professional-waterproof-meter-for-ultrapure-water.html (accessed Nov 30, 2020).

(16) Fisherbrand™ accumet™ AP85 Portable Waterproof pH/Conductivity Meter: Conductivity Meters Electrochemistry | Fisher Scientific https://www.fishersci.se/shop/products/fisher-scientific-accumet-ap85-portable-waterproof-ph-conductivity-meter-2/p-196103 (accessed Nov 30, 2020).

(17) LAQUAtwin EC-33 - LAQUA [Water Quality Analyzer Website] - HORIBA https://www.horiba.com/uk/application/material-property-characterization/water-analysis/water-quality-electrochemistry-instrumentation/compact/details/laquatwin-ec-33-25025/ (accessed Nov 30, 2020).

(18) Ayers, R. S.; Westcot, D. W. *Water Quality for Agriculture*; Food and Agriculture Organization of the United Nations Rome, 1985; Vol. 29.

(19) Rhoades, J. D.; Kandiah, A.; Mashali, A. M. The Use of Saline Waters for Crop Production-FAO Irrigation and Drainage Paper 48. *FAO, Rome* 1992, *133*.

(20) King, A. D.; Birbilis, N.; Scully, J. R. Accurate Electrochemical Measurement of Magnesium Corrosion Rates; A Combined Impedance, Mass-Loss and Hydrogen Collection Study. *Electrochimica Acta*. March 1, 2014. pp. 394–406. https://doi.org/10.1016/j.electacta.2013.12.124.

4.

CONDUCTIVITY APPLICATION 2: DEVELOPMENT OF A SELF-POWERED SKIN PATCH FOR THE SCREENING OF CYSTIC FIBROSIS

Overview

Cystic fibrosis (CF) patients present higher chloride concentrations in sweat than healthy people because of a mutation in a transmembrane regulator protein (CFTR). This increase in the chloride concentration is translated into a rise of the ionic conductivity of sweat. In this chapter, we have made use of this symptom to develop a flexible skin patch to perform the screening of cystic fibrosis by measuring sweat conductivity with our battery sensor. A minimalistic circuit has been used to discriminate the output signal in healthy and non-healthy populations. The device is entirely fabricated with medical grade materials and fabricated with printing and rapid prototyping techniques. The skin patch performance has been calibrated using NaCl laboratory solutions and then a validated with artificial eccrine perspiration. As a result, the patch provides a promising unambiguous digital result that can be read in an electrochromic display with a 95% sensitivity and 100% specificity.

Introduction

Cystic fibrosis (CF) is a genetic autosomal recessive disease that induces mutations on a conductance transmembrane regulator protein, the cystic fibrosis conductance transmembrane regulator (CFTR), which controls the chloride transportation between cells, helps the movement of water in tissues and helps the production of mucus, sweat, saliva tears and digestive enzymes. When the CFTR is mutated causes an accumulation of mucus in exocrine and exocrine-associated organs, affecting lungs, intestinal and reproductive tracks. Although CF is a disease with low incidence (<1:10.000 individuals in Europe), the faulty gene that causes the disease can present more than 2.000 different mutations. Figure 1 shows the estimated prevalence of CF condition worldwide. Because of the many different mutations occurring in CFTR, the disease can vary widely in its severity and symptoms. This can sometimes make CF more difficult to diagnose, as it can mimic other lung diseases such as asthma or bronchitis.

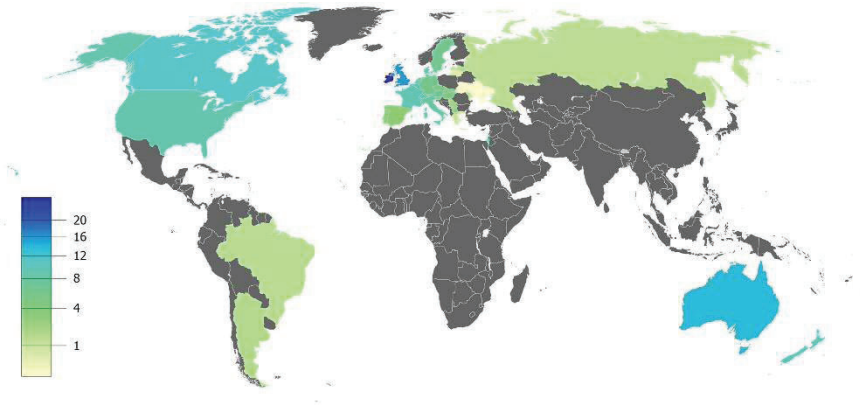

Figure 1. Estimated prevalence of cystic fibrosis per 100,000 habitants[1]

Patients with CF present higher chloride contents in sweat than healthy subjects. Despite being considered a minority disease, the mutation is very common in caucasian societies and for this reason most countries have stablished a national newborn screening program to detect the disease. The screening of CF is performed by the heel prick test, where a drop of blood from the heel is extracted from the newborn and the analysis of different serious rare diseases is performed. For the detection of CF, the immunoreactive trypsin (IRT) is quantified, since this enzyme is expressed in high contents in newborns with CF. If the screening test results positive, the newborn is addressed to a specialized unit of cystic fibrosis to perform the confirmation test, the sweat chloride test. In this test, chloride

concentration in sweat is quantified in order to determine if the patient will suffer CF or will only be carrier of the disease. Infancy chloride concentrations over 60 mmol L^{-1} are classified as positive CF patients, concentrations between 40 – 59 mmol·L^{-1} are considered possible CF patients and concentrations under 40 mmol·L^{-1} are negative CF patients.

During sweat chloride testing, the excretion of sweat is induced by spreading pilocarpine over the skin of the newborn followed by the application of mild electric currents. Early methods consisted in collecting the produced sweat with a medical grade filter paper (Gibson Cooke method), to then measure chloride concentration by conductometric titration of the filter paper. Currently, the gold standard technique of the sweat chloride test to diagnose CF consists in the use of a plastic capillary-based collection system that measures collected sweat with a dedicated apparatus, the Macroduct®. In the last years, many scientific works have reported different approaches of chloride quantification is portable devices.[2–4] However, up to now only one of them has reached the market, the CF Quantum sweat test from Metronic[5]. Images of the mentioned methods and devices are shown in Figure 2.

Although chloride quantification is the gold standard method to diagnose CF, different studies have demonstrated the effectiveness of the sweat conductivity measurement as a screening test for CF[8,9]. In the past twenty years, different series of clinical studies aimed

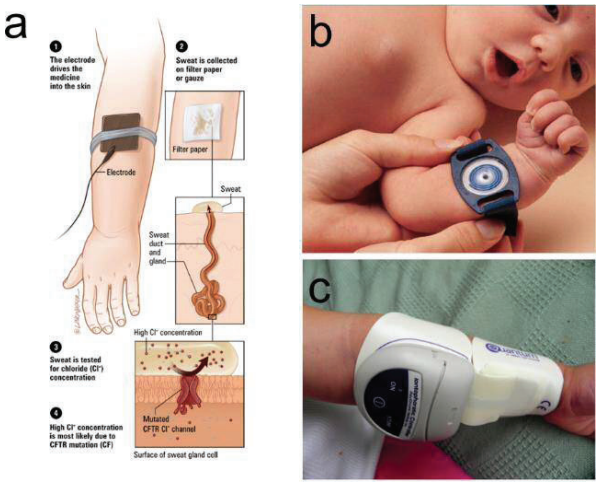

Figure 2. Sweat test methods and devices a) Gibson Cooke method[6] b) Macroduct sweat collection system[7] c) CF Quantum from Metronic, (Reprinted from[5], Copyright (2014), with permission from Elsevier).

to determine the interferences of different ionic species aside from Cl^- and Na^+ in sweat conductivity have been performed.[8–11] The ionic content of sweat varies from patient to patient, however the studies analysed samples of several hundreds of patients and concluded that the conductivity of sweat approximates very closely to the sum of its sodium and chloride ions with a tolerance margin that accounts for conductivity variations caused by the presence of secondary ions (Table 1). The small bias observed between electrical conductivity and chloride concentration was found to be due to the presence of other species like potassium, bicarbonate, ammonium and lactate ions. This bias was observed to be function of the conductivity of the sample, and this enabled converting chloride range-limiting levels to their electrolyte conductivity equivalents shown in Table 1. Note that conductivity is expressed in mmol L^{-1}, being this parameter the conductivity that would have a solution containing the referred concentration of ions. The electrolyte typically selected as reference is sodium chloride (NaCl). Therefore, conductivity values of the solutions used along the chapter are referred to mmol L^{-1} of equivalent NaCl (mM NaCl).

Table 1. Equivalent conductivity due to the chloride content in sweat and in a solution of NaCl.

Concentration (mM)	**Chloride content ($mmol \cdot L^{-1}$)**	**Electrolyte concentration ($mmol \cdot L^{-1}$)**
CF negative	0 - 39	0 - 59
CF possible	40 - 59	60 - 80
CF positive	+ 60	+ 80

Taking advantage of the conductivity sensing capacity of our paper-based battery sensor the development of a self-powered skin patch has been performed. Since the analysis of biological samples requires the disposal of the device after use, the patch was conceived to be a single-use device. The device has been conceived to discriminate between two conductivity ranges - above or under 60 $mmol \cdot L^{-1}$ – as this is the conductivity threshold value that indicates that an individual is suspected of suffering CF condition. A positive result would direct the patient to a confirmatory test of sweat chloride with the gold standard technique for precise chloride quantification and confirmatory diagnosis. The patch combines the low cost and easy handling of paper that is associated with the traditional filter paper-based diagnosis technique and at the same time allows obtaining a digital response with no further handling or treatment of the sample. This removes the need of highly specialized training. Moreover, as it already contains the sensor and the electronics

to manage the signal, sweat collection and testing does not require additional equipment and can be easily taken to any clinical environment. The patch will enable an easy and affordable screening of the CF condition in regional hospitals or clinics, allowing for an early identification of patients not diagnosed with blood tests or for those where the screening test has provided a false negative result but the patient has recurrent respiratory complications and needs to be re-tested again.

Since the self-powered skin patch is designed to detect solely if conductivity surpasses a threshold value, the required amount of electronic components can be reduced to a minimum number that in addition, are entirely printable. The use of electrochromic displays as visual indicators allows providing a non-ambiguous result to the user or the specialist (physician/nurse) performing the test. The patch is schematically depicted in Figure 3.

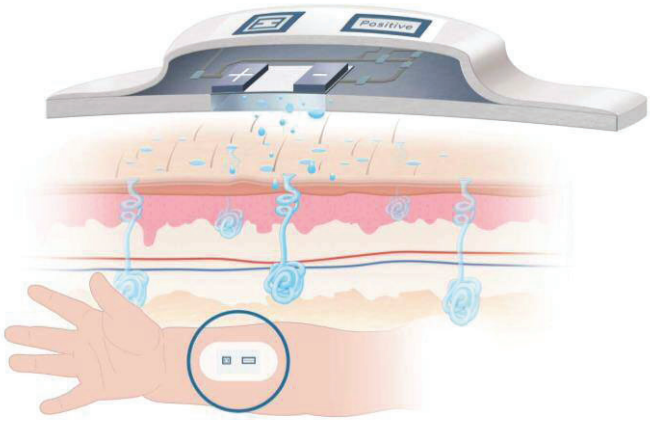

Figure 3. Schematic representation of the self-powered skin patch. (Material from[15], Springer Nature).

Results and discussion

Device design and operation

The patch has been conceived to be applied on the forearm of a patient and remains quiescent until the sweat is absorbed by the paper-based matrix that is in contact with the skin. Upon the complete saturation of the paper core of the battery embedded in the patch, the battery starts to function and delivers a positive output voltage. A very simple circuit

that enables discerning between a healthy and a non-healthy condition handles the signal generated by the battery sensor. This circuit combines ink-jet printed conductive tracks, discrete electronic components and two electrochromic displays (Control and Test output) to show the result. A flow chart of the device operation is shown in Figure 4. In the first step, the forearm skin has to be prepared in the same way as in the state-of-the-art cystic fibrosis measuring tests, which consists on skin forearm cleaning followed by sweat stimulation with iontophoresis (Step 1). Then, the patch is placed on the cleaned skin surface and adhered by the patch adhesive layer (Step 2). At this point, the sweat starts to be absorbed by the paper, which activates the battery (Step 3). Then, the electronics in the patch perform the discrimination of the signal delivered by the battery (Step 4). Finally, the result of the test can be read in the electrochromic displays: The Control Display turns on to show that the patch is functioning correctly and the test is valid, whereas the Test Display turns on only in case of a positive result (Step 5).

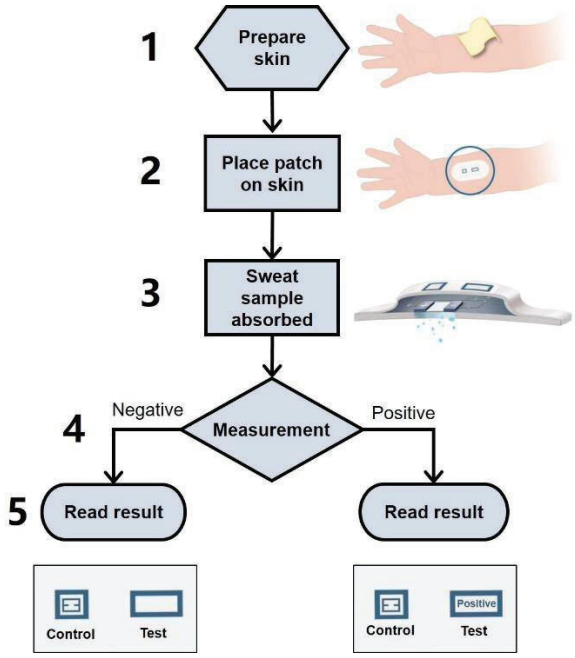

Figure 4. Flowchart of self-powered smart patch operation. (Material from[15], Springer Nature).

Calibration of battery-sensor for cystic fibrosis screening application

The sweat patch was designed to operate within a conductivity range from 5 mM equiv NaCl to 160 mM equiv NaCl (equiv NaCl) as these limits are limits defined in the Diagnostic

Sweat Testing Guidelines from the Cystic Fibrosis Foundation[12,13]. However, since the conductivity test is a method that is only valid to perform a screening of the disease, it was considered that a device able to discriminate the conductivity threshold associated to the existence of CF would be suitable to accomplish the screening goal (in this case, the threshold value corresponds to 60mM eq NaCl).

The self-powered device operating principle relies on the connection of a purely resistive load (R_{LOAD}) to the battery-sensor and calibrate the battery output voltage as a function of the electrolyte conductivity. The selected R_{LOAD} enables the battery to operate inside the ohmic region of its polarization curve, providing a voltage that is directly dependent on the conductivity of the electrolyte used to active it. When aiming to detect above and under a single conductivity level, the paper-based conductivity battery sensor must be connected to a R_{LOAD} of a value that matches with the internal resistivity of the battery when activated with a sample with that specific level of conductivity. This strategy maximizes the sensitivity of the sensor around that operating value. Figure 5 shows the polarization curve of the paper-based conductivity battery sensor when a 60mM eq NaCl is used to activate the battery. The battery has an internal resistivity – which is defined by the slope of the IV curve – of around 1KΩ.

Then, the paper-based conductivity battery sensor response was characterized at the lowest conductivity value of NaCl concentration as defined by the Cystic Fibrosis Foundation, which in this case is set to 5mM eq NaCl. Figure 6 shows the obtained result.

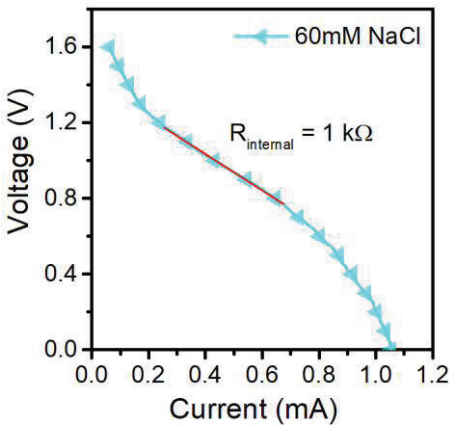

Figure 5. IV curve of a paper-based conductivity battery sensor when introducing a solution of 60mM NaCl. With a red line is represented the internal resistivity of the battery at this particular concentration.

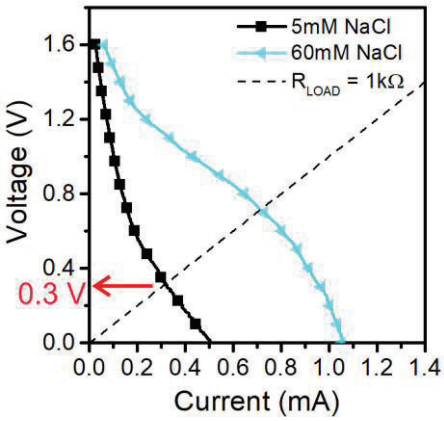

Figure 6. IV curves of the paper-based conductivity battery sensor at the lowest concentration dictated by the Cystic Fibrosis Foundation and at 60mM eq NaCl. With a black dashed line is represented the theoretical R_{LOAD} of 1kΩ.

As it can be observed, the voltage expected from the paper-based conductivity battery sensor at the lowest concentration value when connected to a R_{LOAD} of 1KΩ corresponds to 0.3 V. This value is not sufficient to light an electrochromic display (which requires a minimum of 0.6 V). Therefore, to ensure that the Control Display turned on even at so low conductivity values, a stack of two batteries had to be connected in series. This strategy had been already implemented successfully in the previous chapter. Figure 7 shows the calibration of the paper-based battery stack for ionic conductivities ranging from 5mM to

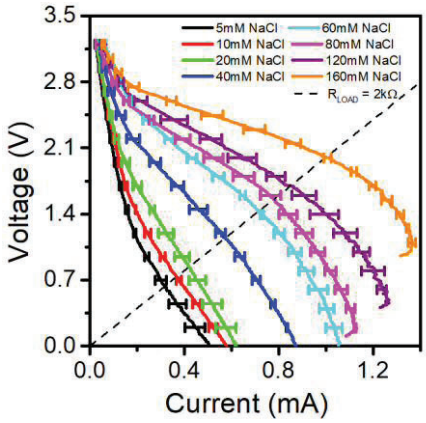

Figure 7. IV curves of the stack of the paper-based conductivity battery sensor at the whole range of conductivities. With a black dashed line is represented the R_{LOAD} of 2kΩ. Lines represent mean values, error bars represent ± one standard deviation, for N = 3.

160 mM eq NaCl. To maintain the maximum sensitivity of the device at the 60mM operating point, the R_{LOAD} value was doubled (from 1KΩ to 2KΩ) as the stack of two battery units provided twice the voltage at the same current, thus doubling the internal resistivity of the device.

The intersection of a theoretical R_{LOAD} of 2kΩ with the IV curves obtained at each conductivity, the expected output voltage of the battery can be derived.

Figure 8 shows the output voltages obtained from the intersections as well as the power generated by the battery. It can be noticed that the use of a battery stack allows obtaining a minimum voltage of 0.6 V at the lowest concentration of NaCl.

The calibration of the stack provided the required information to built-up the self-powered screening device able to detect a possible CF condition in patients. For the implementation of the screening device, the *User protocol for Evaluation of Qualitative Test Performance (EP12-P)* dictated by the Clinical and Laboratory Standards Institute[14] was followed. The protocol recommends evaluating the compliance of the screening test by statistically testing its outcome at the threshold value (60 mM) and at least at a cut-off value that corresponded to the -20% of the threshold value (48 mM in this case). To analyse statistically the performance of the sensor, 40 stacks of two paper-based conductivity battery sensors were fabricated and tested, 20 with a solution of 60mM eq NaCl and 20 at -20%, being 48mM eq NaCl. The mean voltage values delivered by the battery as well as their standard deviation are displayed in Figure 9.

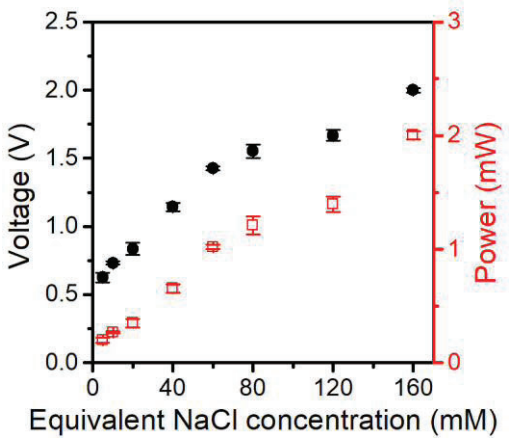

Figure 8. Output voltage and power of the stack of two paper-based conductivity battery sensors as a function of the conductivity of the electrolyte. Data points represent mean values, error bars represent ± one standard deviation, for N = 3. (Material from[15], Springer Nature).

As shown in Figure 9a, the I-V curves obtained by averaging the values of the two sample sets were clearly distinguishable. However, the representation of the voltage values obtained at the intersection with the 2KΩ R_{LOAD} revealed an overlapping of the two sample populations, as shown in Figure 9b. In order to comply with the screening purposes of the patch, a decision strategy about which voltage value had to be established as the voltage threshold that would inform of a positive result (or in other words, that would turn the Test Display on) had to be taken. We decided to give priority to the minimization of false negative results over the false positives, as the consequences of not detecting a possible CF condition impacts severely on the life expectancy of the individuals. Therefore, the threshold voltage was placed at -5% of the Gaussian distribution of the voltage values obtained at 60 mM equiv NaCl ($V_{threshold}$ =1.51 V), which ensured that 95% of patients with sweat conductivity values around 60mM would yield positive results. Due to the partial overlapping of the voltage values obtained at 48mM eq NaCl, this voltage threshold setting yields a 12% false positive results on healthy patients. A graphical representation of the decision limits and the corresponding results of the test is shown in Figure 10.

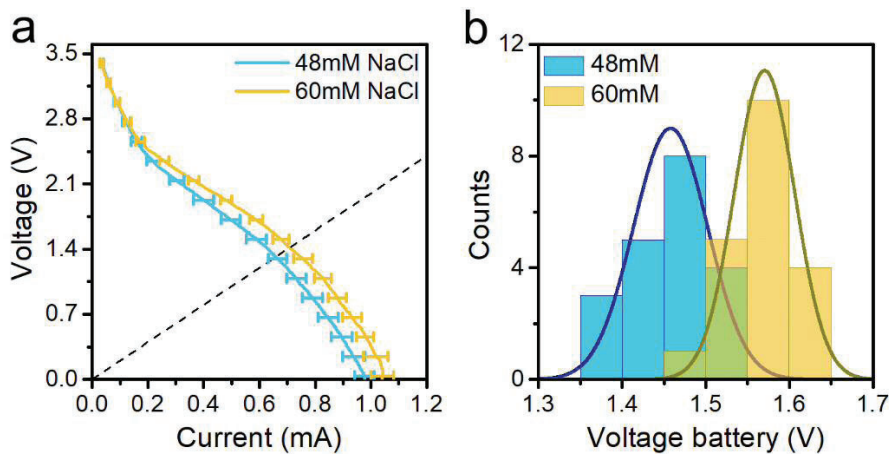

Figure 9. Testing of 40 stacks of two paper-based conductivity sensors at 48mM and 60mM eq NaCl a) IV characteristic of the 40 stacks of batteries b) Extracted output voltage from the intersection with the R_{LOAD} of 2kΩ at each conductivity. Lines represent mean values, error bars represent ± one standard deviation, for n = 20. (Material from[15], Springer Nature).

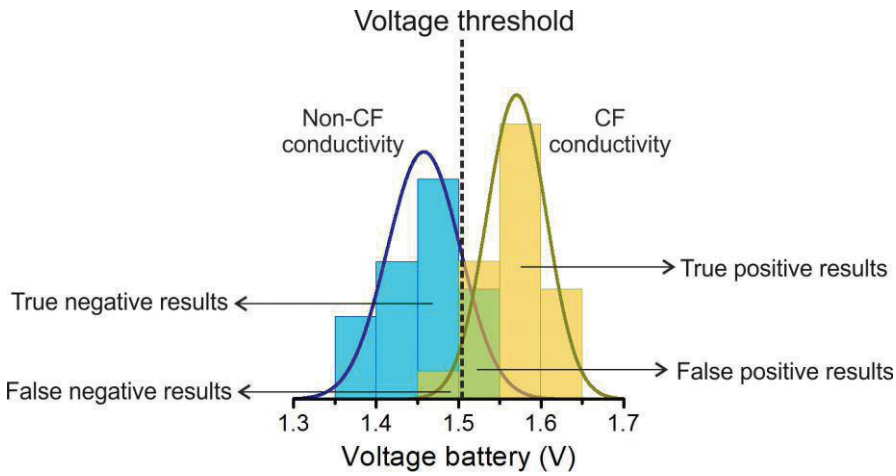

Figure 10. Results of the test when introducing a threshold voltage at 1.51V. CF conductivities under the threshold will provide a false negative result while non-CF conductivities over the threshold will show a false positive result.

Electronic circuit design and characterization

The logic of the self-powered patch was designed following the criteria of a minimum number of electronic components, which would minimize both cost and environmental impact after disposal, while providing an unambiguous visual result to the user. The electrical characterization of the system was performed with a 2400 SourceMeter (Keithley Instruments) and an HP34401A Multimeter (Hewlett-Packard) measuring the current flowing towards the Test display and the voltage at the gate terminal of the transistor, respectively, controlled with a custom LabVIEW program. Figure 11 shows the electronic circuit and components.

Electrochromic displays were again identified as the most suitable technology due to its compatibility with flexible substrates, its fabrication with screen-printing techniques and their capability to operate with voltages as low as 0.6 V. The Control Display was directly connected to the battery stack showing that the patch was working properly regardless of the conductivity of the sweat sample. The Test Display was activated when the battery yielded a voltage that is equal to or above the CF positive threshold voltage. Two diodes were connected to the displays to prevent their discharge once the battery ceased to operate. The Test Display activation was controlled with an n-type MOSFET.

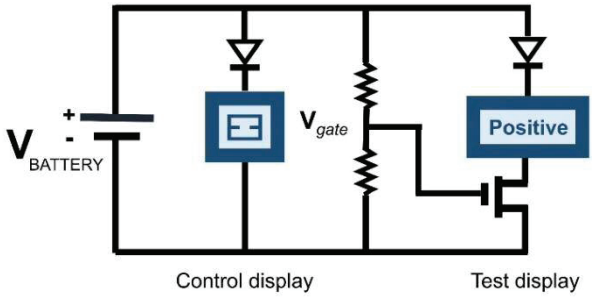

Figure 11. Electronic circuit implemented in the self-powered device. (Material from[15], Springer Nature).

To match the CF-positive threshold voltage of the battery sensor with the gate Voltage (V_{gate} = 1.2 V), R_{LOAD} was divided between two resistors R_1 and R_2. R_2 value was calibrated so when the voltage provided by battery was below the gate voltage, ($V_2 < V_{gate}$) no current ($i_{positive}$) flows towards the Test display. Contrarily, when the battery sensor yielded a voltage over the threshold, $V_2 > V_{gate}$, allowed the current to flow towards the Test Display turning it on. The accumulated threshold charge value that provided a distinguishable display activation at a minimum working potential of 0.6 V was set to 10 µC and 40 µC for the Control display and Test display, respectively.

To test the circuit performance together with the stack of two paper-based conductivity battery sensor it was first mounted on a protoboard. The system was validated with samples with relevant conductivities of 5 mM, minimum conductivity value, 48 mM and 60 mM (all in equiv NaCl). First, the lowest concentration, 5mM eq NaCl, was tested to check the activation of the Control Display. At this concentration, the battery yielded a voltage of 0.6 V during the first 60 seconds (shown in Figure 12), which produced an accumulated charge of 50 µC that activated the Control Display.

Then, the system performance was tested with triplicated samples of 48 mM equiv NaCl and 60 mM equiv NaCl, respectively. The evolution of the voltage at the gate terminal of the N-MOS transistor and the current that flowing towards the Test Display were monitored during the tests as shown in Figure 13.

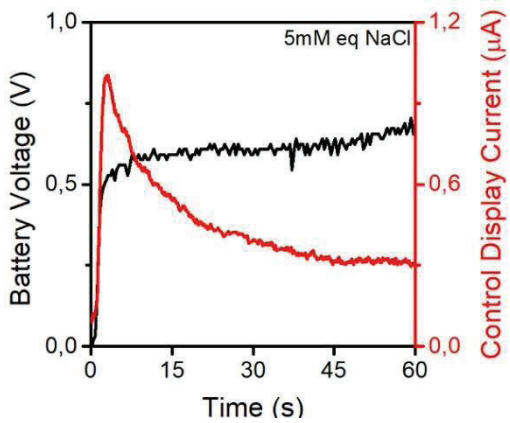

Figure 12. Voltage and current provided by the battery and collected in the Control Display at the lowest conductive sample. (Material from[15], Springer Nature).

From Figure 13a, a steady decline in the voltage at the gate terminal of the transistor under continuous operation is observed. This decline is attributed to an increase in the internal resistance caused by the consumption of the battery electrodes during device operation. However, this behaviour has proven to be highly reproducible with a variation coefficient less than 3.5%. As it can be observed in Figure 12a for 60 mM equiv NaCl, the voltage in the gate terminal of the transistor was higher than the threshold voltage (1.2 V, represented with a dashed line), which caused the current to flow towards the Test Display. The voltage

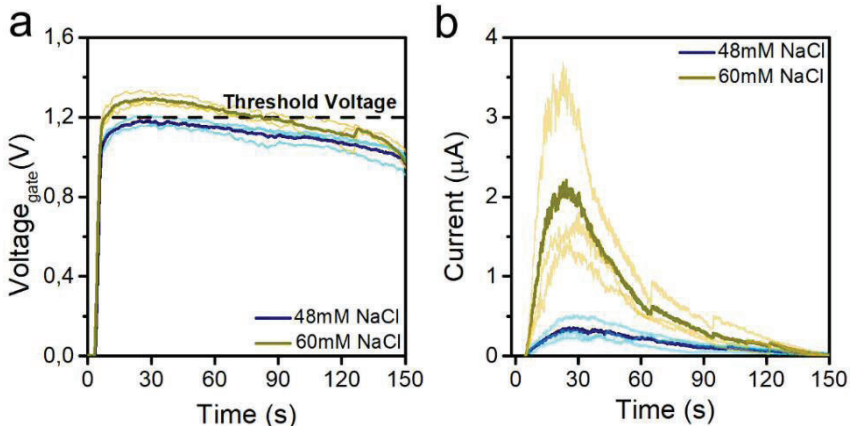

Figure 13. Operation of the system with samples at 48mM and 60mM equiv NaCl. a) voltage at the gate terminal of the transistor and b) the current flowing towards the Test Display. (Material from[15], Springer Nature).

was sustained above the transistor threshold for approximately 60 seconds but subsequently decayed due to the progressive exhaustion of the battery electrodes. At 48 mM equiv NaCl, the voltage at the transistor gate never attained the threshold voltage value; thus, the Test Display remained switched off. The current that flowed towards the electrochromic display during the system operation in both cases has been depicted in Figure 13b. A significant current flowed towards the Test Display for all tested samples at 60 mM. Although no current was expected to flow towards the display at 48 mM, the presence of a small current was observed. This current corresponded to a leakage current of the transistor. This current was unable to switch on the Test Display as the accumulated charge did not exceed the threshold charge to generate any significant change in the active segments contrast. The charges accumulated inside the electrochromic displays for the two tested conductivities are shown in Figure 14.

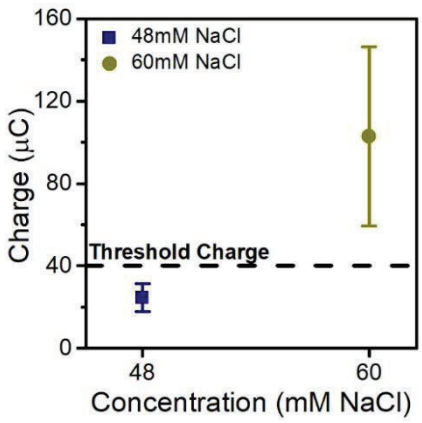

Figure 14. Charge accumulated in the Test Display at the two concentrations of NaCl. Data points represent mean values, error bars represent ± one standard deviation, for N = 3. (Material from[15], Springer Nature).

Self-powered sweat patch fabrication

The stack of two batteries was fabricated using the same design, materials and processes as in the last chapter. The patch laminated components were designed with CorelDraw. All laminate materials – which were medical grade pressure sensitive adhesives from Adhesive Research - were cut with a CO_2 laser and mounted vertically in sequence. The hybrid flexible printed circuit was fabricated using an ink-jet printer (CeraPrinter X-Series). Silver tracks of the circuit were ink-jet printed on a PET substrate. Then, the battery stack,

the discrete electronic components (resistors, diodes and transistor) and the electrochromic displays were hybridized on the printed circuit with a conductive paste (EPO-TEK H20E from Agar Scientific Ltd) that attached the components and ensured the conduction of current. The area surrounding the battery was encapsulated with a PDMS elastomer to protect the electronic circuit and avoid any short circuit caused by occasional sweat overflooding. The elastomer also provides a flat surface that improves skin contact and avoids sweat evaporation. A final outer layer of a medical grade pressure sensitive adhesive was introduced to cover the whole device and provide a pleasant attachment of the patch to the user's skin. The final compact self-contained skin patch is shown in Figure 15.

The device top side includes the two electrochromic displays used to show the results of the test. In this top side, graphic features were printed to make it appealing to small children. The bottom side view of the patch displays the integration of the main functional parts of the self-powered skin patch. An exploded vision of the different components of the patch is shown in Figure 16 and an image of the final device attached to the forearm of a volunteer is shown in Figure 17.

The paper-based battery sensor was placed in the bottom side of the patch in order to absorb the sweat produced by the user of the patch. In this configuration, the sample is forced to pass through the entire thickness of the paper core before reaching the electrode surface and activating the electrochemical reaction. This process mitigates the risk of a partial soaking of the paper battery core that would yield an incorrect conductivity value.

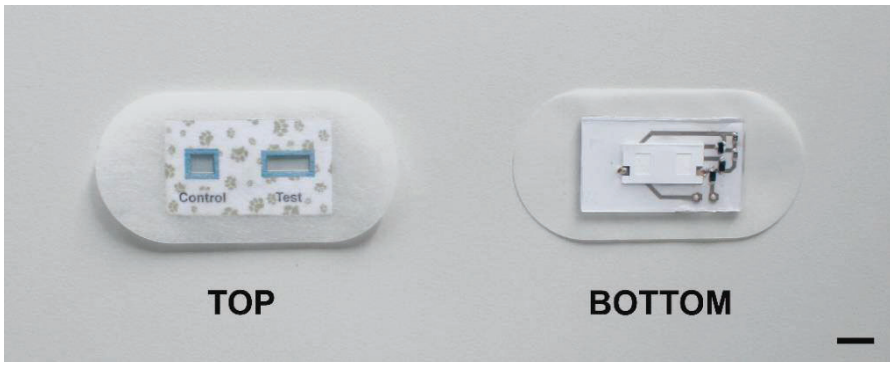

Figure 15. Photograph of the self-powered skin patch after integration (scale bar = 1 cm). (Material from[15], Springer Nature).

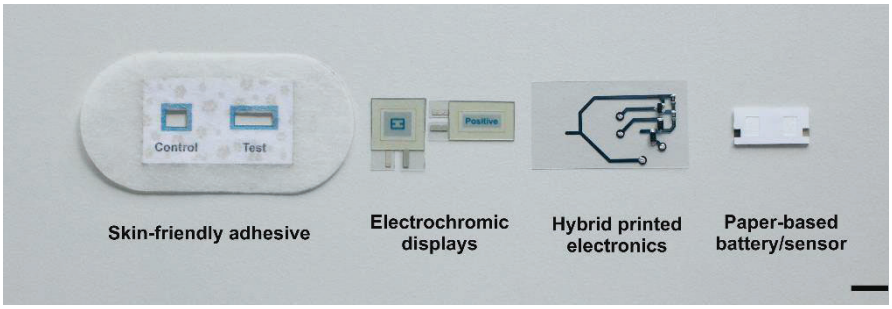

Figure 16. View of the components integrating the self-powered skin patch (scale bar = 1 cm). (Material from[15], Springer Nature).

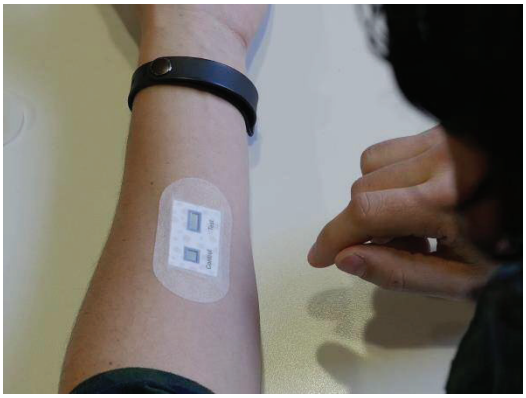

Figure 17. Image of the self-powered skin patch adhered to the skin of a volunteer

Self-powered sweat patch performance validation

Once the system was tested in a protoboard and connected to the stack of two paper-based conductivity battery sensor, the integration of the device was done and the final validation using artificial eccrine perspiration samples. The validation was performed again following the *User protocol for Evaluation of Qualitative Test Performance (EP12-P)* dictated by the Clinical and Laboratory Standards Institute, implementing 40 devices to test the real performance of the whole device.

Body sweat is a complex mixture of accumulative secretions from eccrine, apocrine and sebaceous glands, which contain various electrolytes, ions, amino acids, proteins and lipids. With the exception of ionic species, most of the components present in sweat are

neutrally charged and have a negligible effect on conductivity. So, the final device was validated with an artificial eccrine perspiration solution (Pickering Laboratories), which mimics human eccrine sweat and consists of nineteen amino acids, the most abundant minerals and metabolites from human eccrine sweat (Table 2).

The purchased artificial sweat presented a conductivity of 80 mM equivalent of NaCl. Thus, the conductivity for each sample was adjusted to 48 mM equiv NaCl and 60 mM equiv NaCl by diluting the samples with deionized water.

Table 2. Composition of the artificial eccrine perspiration solution.

Compounds	**Type**	**Quantity (g/L)**
Amino acids	Glycine, L-Alanine ,L-Arginine, L-Asparagine,L-Aspartic acid, L-Citrulline,L-Glutamic acid, L-Histidine,L-Isoleucine,L-Leucine, L-Lysine as hydrochloride, L-Methionine,L-Ornithine as hydrochloride,L-Phenylalanine, L-Serine, L-Threonine,L-Tyrosine, L-Valine,Taurine	from 0.001 for Taurine to 0.15 for L-Serine)
Metabolites	Uric acid, Lactic acid, Urea, Ammonia	(from 0.007 for Uric Acid to 0.8 for Urea)
Minerals	Sodium	1.80
	Calcium	0.81
	Potassium	2.46
	Zinc	0.002
	Iron	0.002
	Sulphate	0.25
	Chloride	2.85
	Magnesium	0.34

To be compliant with the EP12-P test protocol, the validation of the devices was performed with 40 different devices. Half of them were tested with samples with an adjusted conductivity of 48 mM eq NaCl and the other half with samples with the adjusted

conductivity of 60 mM equiv NaCl. As in the calibration of the discrete system, the voltage was recorded at the gate terminal of the N-MOS transistor and the current flowing towards the Test Display was monitored as shown in Figure 18.

Samples that represent “healthy” patients yielded voltages under the transistor threshold voltage in all tested devices. Conversely, samples at higher “non-healthy” conductivity values yielded voltages above the threshold, which enabled the current to flow towards the Test Display except in one case where the voltage provided by the battery was not sufficient to reach the threshold voltage. The current that flowed towards this display in all tested cases was transferred to an accumulated charge in the Test Display. The accumulated charge stored in all the Test displays for the two tested conductivity populations is shown in Figure 19.

All healthy samples generated charges less than 40 µC, and therefore, did not turn on the display. The accumulated charges obtained when testing the devices with the threshold conductivity value of 60 mM ranged from 40 µC to 150 µC. The high dispersion in the stored charge values is attributed to an existing exponential relationship between the voltage gate and the current of the transistor in the working region selected in this application (region near the transistor cut-off value). The contingency table shown in Figure 20 to compare the results of the test with the already-known diagnosis shows that the patch yields 95% of sensitivity and 100% specificity.

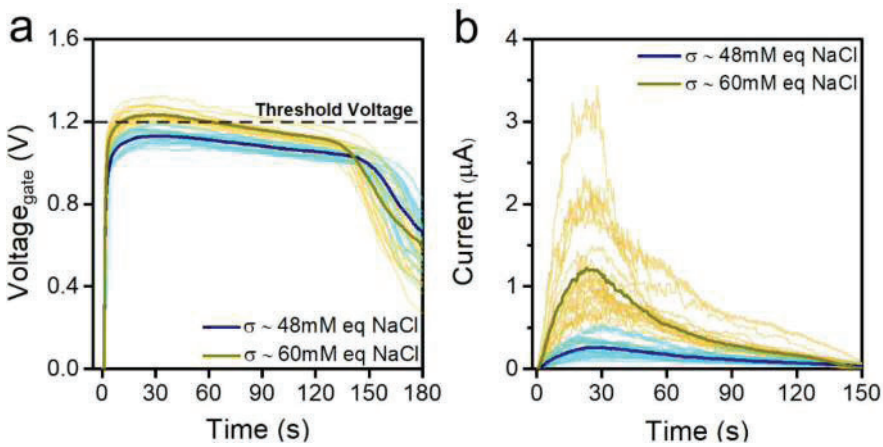

Figure 18. Operation of the device with artificial eccrine perspiration samples at the two conductivities of 48mM equiv NaCl and 60mM equiv NaCl. a) Voltage at the gate terminal of the transistor and b) Current flowing towards the Test Display. (Material from[15], Springer Nature).

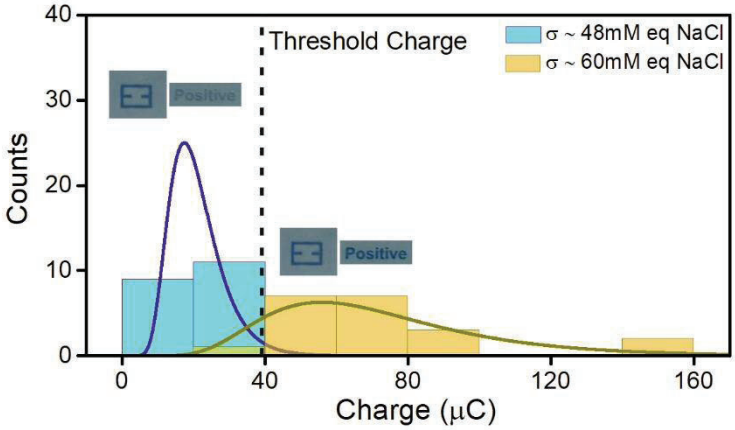

Figure 19. Gaussian distribution of the accumulated charge at the two sample conductivities tested in the device.

The difference in performance of the different patches was assessed by testing the variability of the fabricated batteries with NaCl solutions showed in Figure 9b, testing the response of the batteries after connecting the minimal electronic circuit (Figure 14) and checking the performance of 40 ready-to-use patches with artificial sweat samples (Figure 19). The coefficients of variation obtained by characterizing the single batteries at the different targeted concentrations were less than 5%. However, when the battery was connected to the electronic circuit mounted in a protoboard, the coefficients of variation of

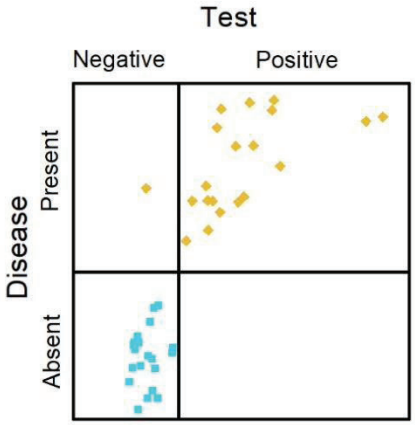

Figure 20. Final representation of the results provided by all devices compared with the known condition of the samples, healthy and non-healthy. (Material from[15], Springer Nature).

the response increased to 25% in the case of a low conductivity value (48 mM) and 40% in the case of the upper threshold value (60 mM). This finding is attributed to the fact that the system relies on a single N-MOS transistor to determine whether the voltage generated by the battery corresponds to a positive or a negative result. When the battery operates at voltages near the value of the threshold voltage of the transistor, the transistor operated in a transition region that limited the current generated by the battery. This was the main source of the variation recorded in the total current that flowed towards the display elements. When 40 patches are tested with artificial sweat samples that contained amino acids, urea and different ions, the coefficients of variation slightly increased to 30% (at 48 mM) and 42% (at 60 mM), which indicated that the effect of introducing a more complex matrix that mimics real sweat does not introduce additional dispersion to the results.

Outlook: pre-clinical testing

The research described in this chapter was published in the Microsystems & Nanoengineering Journal[15] and the patch received an award as the Best Prototype from the Organic Electronics Association in 2019 (https://oe-a.org/). In addition, funding from the European Research Council Proof-of-Concept call was obtained with the aim of performing pre-clinical testing with paediatric patients of the Cystic Fibrosis Unit of Sant Joan de Déu Hospital in Barcelona. Thus, the POWER-PATCH project aims at performing a late-stage prototype development, a safety clinical study with patients and investigate the commercial feasibility of this innovation. POWER-PATCH can make a significant impact through cost-effective, efficient and quick screening that could be used in pulmonology units in clinics and hospitals with no expertise in CF. Moreover, this rapid test could also be implemented in countries were both new-born screening and confirmatory CF testing is scarcely supported due to cost-effectiveness.

Clinical testing at the Hospital required the preparation of a clinical protocol, the refinement of the technical specifications of the self-powered skin patch and the readying of the informed consent to be provided to the volunteers. The documents were submitted to the Clinical Research Ethics Committee (CEIm) of Sant Joan de Déu Hospital. The approval was obtained on February of 2020 (see Annex 1). Afterwards, the Investigator Brochure and the Approval of the CEIm was submitted to the Agencia Española del Medicamento y Productos Sanitarios (AEMPS) to request permission to perform the clinical assay. The approval of the Agency was obtained on July 2020 (see Annex 2).

The technical validation requires performing different POWERPATCH prototypes in order to ensure the correct specifications required for class IIa medical device. The final prototypes will be tested in our Institute (IMB-CNM) and in the hospital (SJD) in close collaboration with the physicians and principal investigator (PI) in charge of the research. Later on, participants of the study will be recruited. The clinical assay will take place during the first six months of 2021. For the assay, 14 CF patients and 14 healthy participants will be tested with the self-powered skin patch and the safety of the patch will be tested. Afterwards, the statistical department of the SJD Hospital will analyse the results obtained during the study. Finally, a Contract Research Organization (CRO) will prepare the final report of the assay; the PI of the hospital will add the relevant clinical information and all the reports will be sent to AEMPS and to the ERC.

Conclusions

The device presented in this chapter shows the feasibility of a self-powered patch for the screening of cystic fibrosis condition with the novel method of conductivity measurement that is the cornerstone of the present thesis. The realization of the patch demonstrates for the first time the suitability of the battery sensor to develop a clinically relevant digital ASSURE device. Importantly, it is a powerful example that validates the three main technological drivers identified in the introductory chapter (i.e. printed electronics, paper microfluidics and self-powering sensing approaches) as effective enablers of the long-awaited digital ASSURED devices.

In this particular example, it becomes evident how using the paper battery as a conductivity sensor enables measurements with an extremely simple electronic circuit that utilizes a small number of components. Considering state-of-the-art printing technologies, the elements of the circuit can be entirely printed with inkjet printing processes. Combined with the screen printing methods that are employed to obtain the battery elements and the electrochromic displays, these processes pave the way to mass production of the device. In fact, these factors render the patch suitable for a single-use and disposable approach, as the low cost associated with the materials and fabrication processes and the use of a minimum number of electronic components contributes to the sustainability of the device.

These promising preliminary results resulted in a new research project that aims to further develop the patch technology and perform a pre-clinical study in collaboration with the Cystic Fibrosis Unit from largest local children hospital (Hospital Sant Joan de Déu).

In addition to the inherent impact of the current development in the clinical sector, the conductivity patch has the possibility to be utilized to evaluate the electrolyte content in sweat for other purposes, such as dehydration induced by physical activity, which is described in the next chapter.

References

(1) Lopes-Pacheco, M. CFTR Modulators: Shedding Light on Precision Medicine for Cystic Fibrosis. *Frontiers in Pharmacology*. September 5, 2016. pp. 275. https://doi.org/10.3389/fphar.2016.00275.

(2) Mu, X.; Xin, X.; Fan, C.; Li, X.; Tian, X.; Xu, K.-F.; Zheng, Z. A Paper-Based Skin Patch for the Diagnostic Screening of Cystic Fibrosis. *Chemical Communications.* March 3, 2015. pp. 6365–6368. https://doi.org/10.1039/C5CC00717H.

(3) Emaminejad, S.; Gao, W.; Wu, E.; Davies, Z. A.; Nyein, H. Y. Y.; Challa, S.; Ryan, S. P.; Fahad, H. M.; Chen, K.; Shahpar, Z.; Talebi, S.; Milla, C.; Javey, A.; Davis, R. W. Autonomous Sweat Extraction and Analysis Applied to Cystic Fibrosis and Glucose Monitoring Using a Fully Integrated Wearable Platform. *Proceedings of the National Academy of Sciences pf the United States of America.* April 17, 2017. pp. 4625–4630. https://doi.org/10.1073/pnas.1701740114.

(4) Koh, A.; Kang, D.; Xue, Y.; Lee, S.; Pielak, R. M.; Kim, J.; Hwang, T.; Min, S.; Banks, A.; Bastien, P.; Manco, M. C.; Wang, L.; Ammann, K. R.; Jang, K. I.; Won, P.; Han, S.; Ghaffari, R.; Paik, U.; Slepian, M. J.; Balooch, G.; Huang, Y.; Rogers, J. A. A Soft, Wearable Microfluidic Device for the Capture, Storage, and Colorimetric Sensing of Sweat. *Science Translational Medicine.* November 23, 2016. pp. 366ra165. https://doi.org/10.1126/scitranslmed.aaf2593.

(5) Rock, M. J.; Makholm, L.; Eickhoff, J. A New Method of Sweat Testing: The CF Quantum®sweat Test. *Journal of Cystic Fibrosis.* May 23, 2014. pp. 520–527. https://doi.org/10.1016/J.JCF.2014.05.001.

(6) Diagnostic Testing - Johns Hopkins Cystic Fibrosis Center https://hopkinscf.org/knowledge/diagnostic-testing/ (accessed Nov 30, 2020).

(7) Macroduct® Sweat Collection System – ELITechGroup: In Vitro Diagnostic Equipment & Reagents https://www.elitechgroup.com/product/macroduct-sweat-collection-system-2 (accessed Nov 30, 2020).

(8) Hammond, K. B.; Turcios, N. L.; Gibson, L. E. Clinical Evaluation of the Macroduct Sweat Collection System and Conductivity Analyzer in the Diagnosis of Cystic Fibrosis. *The Journal of Pediatrics.* February 1, 1994. pp. 255–260. https://doi.org/10.1016/S0022-3476(94)70314-0.

(9) Mattar, A. C. V.; Leone, C.; Rodrigues, J. C.; Adde, F. V. Sweat Conductivity: An Accurate Diagnostic Test for Cystic Fibrosis? *Journal of Cystic Fibrosis.* September 1, 2014. pp. 528–533. https://doi.org/10.1016/j.jcf.2014.01.002.

(10) Heeley, M. E.; Woolf, D. A.; Heeley, A. F. Indirect Measurements of Sweat Electrolyte Concentration in the Laboratory Diagnosis of Cystic Fibrosis. *Archives of Disease in Childhood.* May 2000. pp. 420–424.

(11) Lezana, J. L.; Vargas, M. H.; Karam-Bechara, J.; Aldana, R. S.; Furuya, M. E. Y. Sweat Conductivity and Chloride Titration for Cystic Fibrosis Diagnosis in 3834 Subjects. *Journal of Cystic Fibrosis.* March 1, 2003. pp. 1–7. https://doi.org/10.1016/S1569-1993(02)00146-7.

(12) LeGrys, V. A.; Yankaskas, J. R.; Quittell, L. M.; Marshall, B. C.; Mogayzel, P. J. Diagnostic Sweat Testing: The Cystic Fibrosis Foundation Guidelines. *Journal of Pediatrics.* July 1, 2007. pp. 85–89. https://doi.org/10.1016/j.jpeds.2007.03.002.

(13) Farrell, P. M. P.; Rosenstein, B. J. B.; White, T. T. B.; Accurso, F. J.; Castellani, C.; Cutting, G. R.; Durie, P. R.; Legrys, V. a; Massie, J.; Parad, R. B.; Rock, M. J.;

Campbell, P. W.; Fibrosis, C.; Health, C.; Hospital, M.; Children, S.; Hill, C.; Foundation, C. F.; Campbell 3rd, P. W. Guidelines for Diagnosis of Cystic Fibrosis in Newborns through Older Adults: Cystic Fibrosis Foundation Consensus Report. *Journal of Pediatrics.* August 1, 2008. pp. S4–S14. https://doi.org/S0022-3476(08)00398-3 [pii]\r10.1016/j.jpeds.2008.05.005.

(14) NCCLS. EP12-A User Protocol for Evaluation of Qualitative Test Performance; Approved Guideline. *22* (15).

(15) Ortega, L.; Llorella, A.; Esquivel, J. P.; Sabaté, N. Self-Powered Smart Patch for Sweat Conductivity Monitoring. *Microsystems and Nanoengineering.* January 28, 2019. pp. 1-10. https://doi.org/10.1038/s41378-018-0043-0.

5.

CONDUCTIVITY APPLICATION 3: IMPLEMENTATION OF A SINGLE USE DEHYDRATION MONITOR FOR ATHLETES

Overview

In this chapter we present the validation of the battery sensor performance with real sweat samples and explore the applicability of sweat conductivity measurement to the assessment of dehydration episodes of athletes under intense physicals activities such as long-distance races.

The first objective of this chapter was to develop reliable and reproducible sweat absorbent patches able to collect sweat from the lower back skin of volunteers of a marathon race and perform ex-vivo sweat conductivity measurements with a commercial conductivity sensor. Sweat measurements taken at the beginning and at the end of the physical exercise were then analysed together with body weight losses and some blood dehydration biomarkers in order to find out a parameter correlation.

The second objective of the present chapter was to validate the performance of the battery sensor when measuring the conductivity of real sweat samples. Therefore, high capacity sweat absorbent patches were developed and tested on human volunteers in order to obtain sufficient sample volume to feed our battery sensor and a commercial conductivity standalone device.

Introduction

Wearable devices field is already a consolidated market that sized up to USD 32.63 billion in 2019, according to a review performed by Grand View Research[1]. The report estimates a CAGR of 15.9% by 2027. The wearable devices field can be segmented between application areas such as wellness, sports/fitness, lifestyle computing, medical, security and safety and mining industry[2], being the three first areas the larger in terms of market penetration[3]. Wearables can also be divided by product types, for example, as wrist-worn accessories, e-textiles and e-patches. Wrist-worn accessories are the most popular wearable devices since they include smart watches and wristbands. These devices have two main functionalities: to communicate and show notifications to the user, acting as the perfect complement to smartphones and to monitor human physiological and biomechanical signals. Wrist-worn accessories can sense these biological signals due to the maturity achieved by physical sensors in the last couple of decades. High-performing accelerometers, gyroscopes, light sensors, heart rate sensors, barometers or vibration sensors are nowadays being readily integrated in wearable devices such as the Apple Watch, Samsung Galaxy Watch or the Huawei Watch among others. In the field of e-patches – which are devices designed to be attached to the arm or the chest of the user - there are is also powerful commercial examples. The HealthPatch MD by VitalConnect and the e+ Emergency Patch provide continuous electrocardiography (ECG) monitoring, acceleration measurements, respiration rate (with respiratory bands), body temperature and detection of postures and basic activities performed by the user [4]. Nowadays, since the maturity of these sensors is very high most of the research being developed in the area is focused on increasing the functionalities offered by the existing devices in terms of signal processing, data management and machine-learning algorithms to achieve accurate diagnose, warn or monitor rehabilitation precedures[5–8]. Beyond the monitoring of physical parameters, measuring chemicals from inside the body such as lactate, pH, or electrolytes holds promise of providing a much more useful insight of wearer's health, performance or stress at molecular level. A big variety of *in-vitro* chemical sensors are reported in the literature but when coming to *in-vivo* monitoring they face the problem of body fluid extraction to perform the measurement that divides them in two groups: invasive and non-invasive wearable sensors. Invasive sensors use blood as the main biofluid to assess health status. Despite the large amount of literature reporting implantable blood sensors, only the commercial Freestyle Libre glucose monitor from Abbot seems to have finally encountered a reliable and harmless solution that allows obtaining continuous data from the bloodstream for up to 15 days[9] In fact, invasive sensors seem to be not suitable for continuous monitoring systems in applications not life threatening, such as wellness or

fitness. Consequently many efforts have been done to monitor biochemical parameters from accessible biofluids such as saliva[10,11], tears[12] or sweat[13–18] and relate their contents to relevant information from the individuals.

In this chapter, we present the initial steps of the implementation of a self-powered skin patch to monitor sweat conductivity as a way to assess dehydration during physical exercise. Dehydration has been traditionally defined by the percentage of body mass lost by sweat and has been associated to problems such as reduced athletic performance, heat illness, skeletal muscle cramps and acute renal failure[19]. Conventionally, a 2%-body mass reduction has been considered as the threshold limit in which exercise-associated body mass loss without fluid ingestion could cause medical complications[20–22]. Water loss during exercise contains also many different micronutrients (sodium, chloride, potassium, calcium, magnesium, iron, zinc, copper and vitamins) and compounds (lactate, urea, ethanol, ammonia, bicarbonate, glucose, heavy metals, antibodies, cytokines, amino acids or proteolytic enzymes)[23]. Sodium and chloride are excreted in the largest amounts, but this also vary considerably among different individuals[24,25]. Furthermore, dehydration has been associated to an increased[26], decreased[27] or unaltered[28] concentration of sodium and chloride in sweat. Therefore, the determination of dehydration condition based on sweat composition is still a challenging task.

This chapter describes the use of a single-use absorbent patch and a paper-based conductivity battery-sensor to measure the conductivity of athletes sweat and assess their hydration status. The research presented in this chapter is framed within project D2PATCH (call PRODUCTE-2018 from the Agència de Gestió d'Ajuts Universitaris i de Recerca).

Results and discussion

Sweat absorbent patch design, implementation and calibration

The single-use absorbent patch was conceived to absorb sweat from the lower back of the user, since it has been reported to be the body area with the higher sweat flow rate produced during running, for both men and women[29]. The objective of the device was to absorb sweat directly from the skin and allow performing a conductivity measurement in a reproducible manner. The sweat absorbent patch consists of two main parts, the collection pad and the storage channel, which are enclosed inside adhesive layers. Figure 1 shows a scheme that identifies these two wicking components. One face of the collection pad is

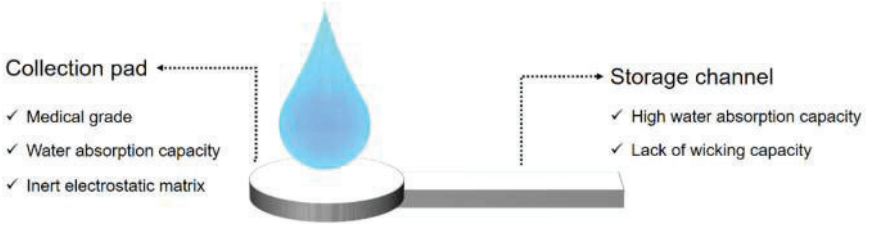

Figure 1. Schematic representation of the wicking materials in the sweat absorbent patch.

left open to air, so it can be placed directly in contact with the skin of the user and absorb the sweat produced. The storage channel allows the storage of the excess of collected sweat. The channel also provides a visual inspection of the sweat level of the patch, indicating in this way when the minimum volume of sweat to perform the conductivity measurement has been collected.

A first selection of materials was performed in order to ensure the necessary specifications of the device. As specified in Figure 1, the collection pad must be of medical grade, since it will be in direct contact with the skin of the user and it also needs to have a high water absorption capacity, in order to absorb all the *in-situ* generated sweat. Additionally, it is important that the pad behaves as an inert electrochemical matrix in order to avoid any interaction between sweat and the paper-based material. The geometric form factor was designed to be circular to fit the commercial electrodes used to perform the conductivity measurement, as shown in Figure 2. Besides, the storage channel requires a high water absorption capacity in order to hold all the excess of sweat from the collection pad. However, it is important that its wicking capacity is not higher than the one in the collection pad material, in order to avoid the drying of the collection pad, which would affect the viability of the conductivity measurements.

For these reasons, the material chosen for the collection pad consisted of glass-fiber LF1

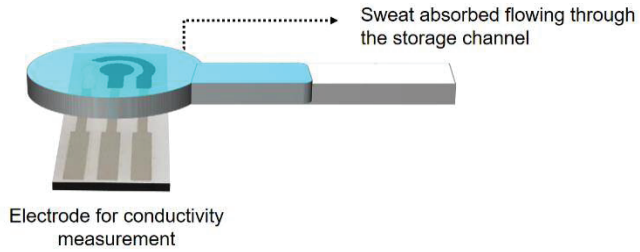

Figure 2. Representation of the measurement setup with the electrodes integrated with the sweat absorbent patch.

paper (from GE). The suitability of this material to act as a porous matrix that contains the liquid to be characterized electrochemically has been already acknowledged in previous chapters of this thesis. For the implementation of the storage channel, three paper-based materials with different porosities and capillary rates were tested: a cellulose membrane from Alhstrom (238 Cellulose), and two different glass-fibers, the already presented LF1 and Standard 14, both from GE. Both the pad and the channel were encapsulated between laminates of pressure sensitive adhesives (PSA) from Adhesive Research that had been previously cut and shaped with a CO_2 laser. An exploded view of all the different parts of the patches and pictures of the fabricated devices are presented in Figure 3.

To achieve a reproducible measurement of the sweat conductivity, the volume of the

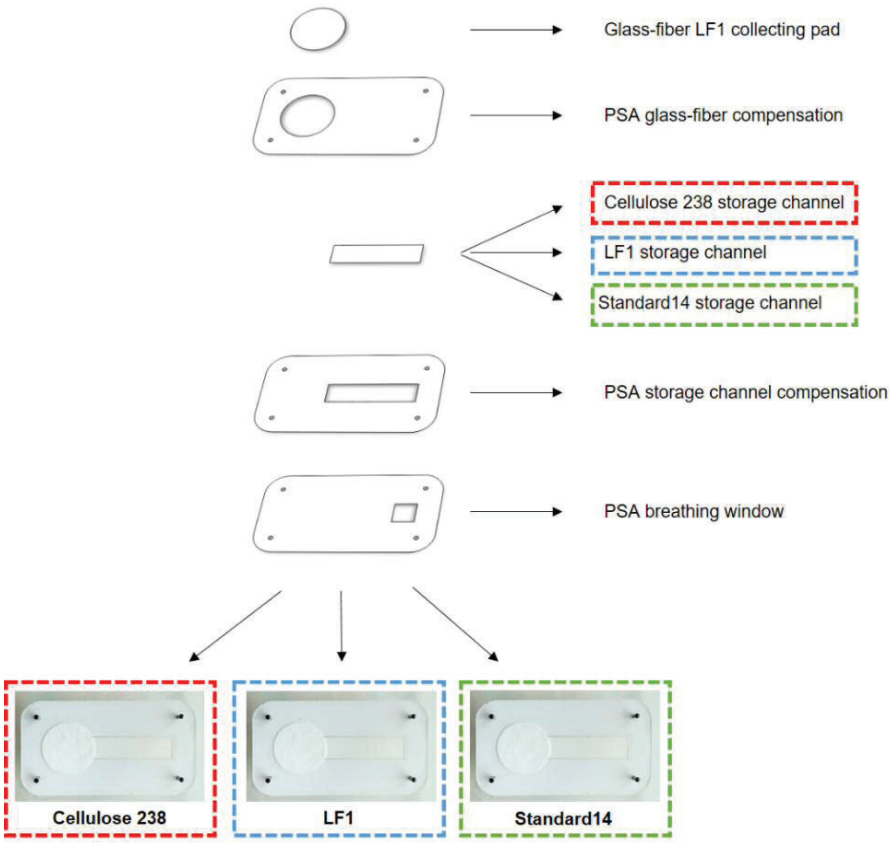

Figure 3. Exploded view of the sweat absorbent patch, showing the three storage channel materials that were tested (scale bar = 1 cm).

collection pad after sweat absorption had to be kept constant. In practice, this meant that the storage channel had to be able to draw out the excess of sweat accumulated in the pad in a continuous manner. Therefore, the absorption capacity of the three papers in time was analysed by performing a visual study of a coloured liquid flowing through the device. The experiment was done using a blue dye (Erioglaucine disodium salt) dissolved in a deionized water solution. The resulting colour provided sufficient contrast to perform a clear visual inspection of the flow. The sample was poured onto the collection pad while pictures of the fluid progression along the channel were taken. Pictures of patches corresponding to three different paper channel materials (taken after 5 seconds, 1 minute and 15 minutes) are shown in Figure 4.

As it can be observed in Figures 4, the fluid progression observed in the patches differs depending on the paper used to define the storage channel. The structure with the Cellulose 238 as the storage channel (device 1) was not suitable for the purpose of this application due to its wicking capacity. In this case, the storage channel absorbed the liquid present in the collection pad, modifying the volume inside the pad, which was necessary to keep constant and completely full to perform a reproducible conductivity measurement. In device 2 and device 3, which used LF1 and Standard 14 glass-fiber respectively, the volume inside the collection pad and the storage channel was maintained unaltered up to 15 minutes after addition of the sample, indicating no drying of the collection pad. From the two suitable materials, it was decided to use Standard 14 glass-fiber, since it presents a higher water absorption capacity than LF1 (50.9 $mg \cdot cm^{-2}$ and 25.3 $mg \cdot cm^{-2}$, respectively). Therefore, the final device included LF1 glass-fiber as collection pad and Standard 14 glass-fiber as the storage channel. Finally, to assist the visual indication of sufficient sweat absorption, a line with food dye was introduced at the storage channel. The dye is barely visible when no sweat is present inside the storage channel (as shown in Figure 5), and it turns into a bright blue colour when the fluid reaches the line (as it can be seen in Figure 6c).

Once the materials of the single use absorbent patch were selected, the patches were calibrated using NaCl solutions with different conductivities, within the range of reported values in sweat[30]. The conductivity calibration of the devices was performed by measuring the electrolyte resistance when the liquid sample was absorbed into the device. In addition, the electrolyte resistance of a single drop of 100 µL of NaCl on top of the electrodes was performed. This test allows to evaluate the effect of the electrolyte confined inside the paper matrix of the device. A schematic representation of the setup to measure the conductivity of the electrolyte and pictures of the actual setups are shown in Figure 6.

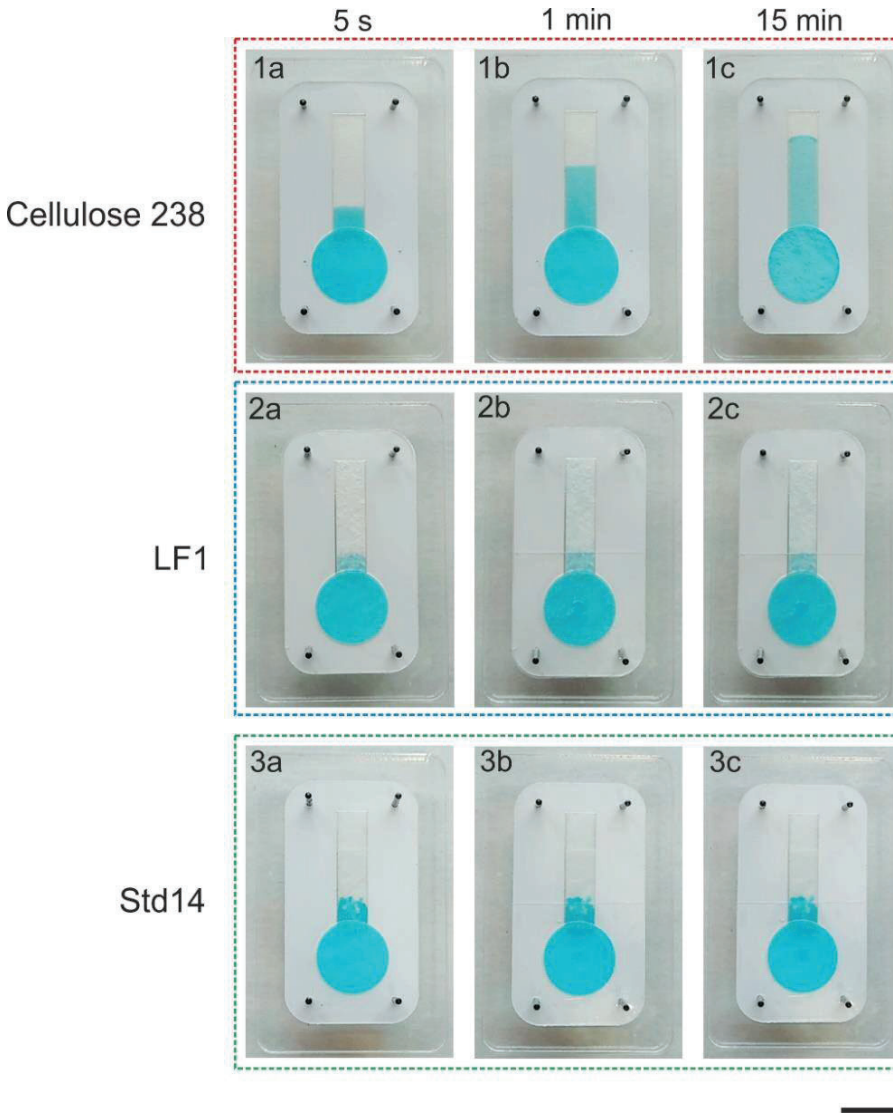

Figure 4. Fluidic experiment with the structure that combined LF1 paper in the collection pad and Cellulose 238 (red dashed square), LF1 (blue dashed square) and Standard 14 (green dashed square) as storage channels (scale bar = 1 cm).

The calibration was done by performing an Electrochemical Impedance Spectroscopy (EIS) measurement, applying a sinusoidal signal with 10 mV amplitude in a sweep of the frequency, from 100kHz to 1kHz with the EmStat Pico Potentiostat (Palmsens BV, Houten, The Netherlands). Finally, the value of the electrolyte resistance was extracted from the total impedance when the imaginary component of the impedance was almost zero, as it

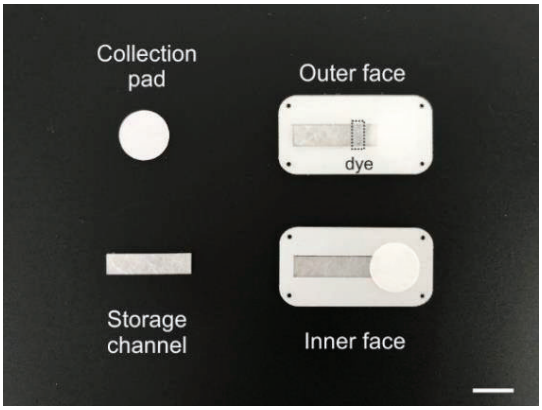

Figure 5. Image of the assembled sweat absorbent patch and its wicking components (scale bar = 1 cm).

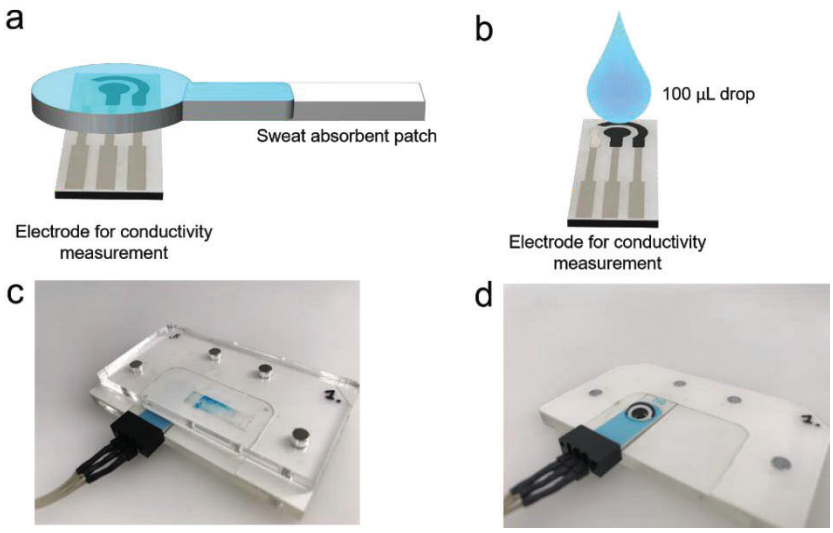

Figure 6. Experimental setup used to measure the electrolyte conductivity inside the paper-based sweat absorbent patch (a, c), and using a 100 µL drop of NaCl without any paper over the electrodes (b, d).

has been widely explained in the literature. The results of the electrolyte resistance depending on the setup measured are shown in Figure 7.

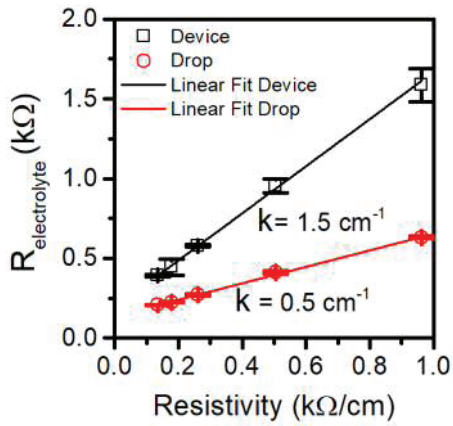

Figure 7. Representation of the electrolyte resistance measured when depositing the sample inside the sweat absorbent patch device (black squares) and with a drop of 100 µL NaCl over the electrode (red dots). Data points represent mean values, error bars represent ± one standard deviation, for N = 3.

As explained in previous chapters, the electrolyte resistance relates with the conductivity by equation (1):

$$R_{electrolyte} = \frac{k}{\sigma} = k \cdot \rho \qquad (1)$$

Where σ and ρ corresponds to the liquid conductivity and resistivity respectively and k corresponds to a geometrical parameter, the cell constant, which takes into account the geometry and position of the sensing electrodes and the dimensions of the bulk of the electrolyte, being the whole medium over the electrodes.

As it can be observed in Figure 7, the electrolyte resistance measurement differs a lot when it is absorbed by the paper matrix and then measured (represented with black squares) or when the electrolyte is deposited free over the electrode (red circles). The reason is that when measuring the electrolyte resistance with a drop of 100 µL solution in an electrode area of 0.13 cm^2, the bulk of the electrolyte is purely a drop of liquid with no additional resistance. In this situation, the current lines generated between the electrodes flow freely from one electrode towards the other, presenting a smaller cell constant and maximizing the dynamic range of the system. In contrast, when using the absorbent patch, the current lines are confined inside a porous paper matrix, in our case within a height of 250 µm, increasing the bulk resistance radically, and hence, the cell constant, which

decreases the dynamic range of the device making it insensitive at low conductivities. In contrast, it can be observed that in this particular range of resistivities, the sensitivity of the device is higher than the one obtained with the drop configuration. In addition, it can be noticed that the linear relationship between the electrolyte resistance and the resistivity is maintained in both cases. To analyse the repeatability of the device fabrication process and take into account the electrode intrinsic variation, three different electrodes were calibrated with the same NaCl solutions as in the previous experiments. Due to the single use nature of the patches, 45 different patches were needed to perform the calibration, one patch per each measurement with three repeats per sample conductivity and three different electrodes, as shown in Figure 8. It can be seen the similarity between all the experimental values at each conductivity, which was traduced in a coefficient of variation of the system cell constants of 1%.

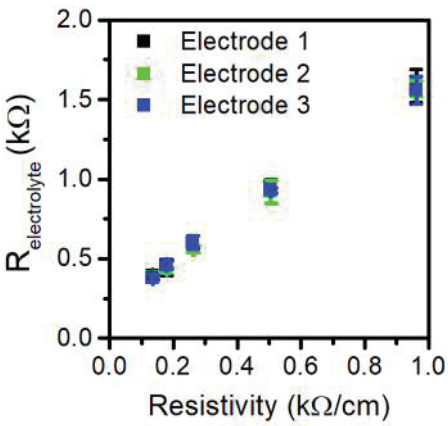

Figure 8. Device calibration for the analysis of the repeatability in the patches manufacturing process. Data points represent mean values, error bars represent ± one standard deviation, for N = 3 different patches.

Sweat absorbent patch testing in a relevant environment

Once the sweat absorbent patch was calibrated and its reproducibility was ascertained in the laboratory, its performance was tested in human volunteers. In order to set the experiment in a relevant environment, the volunteers were selected among the participants of a local mountain trail of 60 km, the *TRAIL PIRINEU 2019*[31]. The volunteers were selected from a group of male volunteers, with ages ranging from 30 to 45 years with at least 10 years of specific training experience. All the volunteers were asked to fill an

informed consent and a confidential agreement of sample donation (agreed with the ethics committee of the Olot Hospital). The aim of this test was firstly to evaluate the capability of the patch to absorb sweat from the skin during intense physical activity and secondly, to stablish a correlation between sweat conductivity changes and already identified dehydration markers in blood.

The test was performed in collaboration with Serialmed SL., a Catalan company focused on promoting healthy and safe sports practices by preventing, controlling and maintaining cardiovascular risk factors in safety standards through good lifestyle habits. Serialmed was in charge of recording body weight and different blood dehydration biomarkers of the volunteers before and after the race, whereas our research group focused in the obtaining of sweat samples and perform *in-situ* conductivity measurements. Since dehydration occurrence in individuals has been reported to be highly dependent of their initial hydration conditions as well as their personal health status[25], the relative variation of sweat conductivity between two different points of the race was taken as a potential indicator of dehydration. Likewise, blood samples were collected the day before the race and immediately after the race. The blood samples were analysed with the i-STAT handheld blood analyser with the CHEM8+ cartridge, which measured blood sodium (Na), potassium (K), chloride (Cl), total carbon dioxide (TCO_2), anion gap, ionized calcium (iCa), glucose (Glu), urea nitrogen (BUN), creatinine (Crea), Hematocrit (Hct) and Hemoglobin (Hgb). In addition, the body mass of the volunteers was also recorded before and after the race. Although body mass loss by perspiration is not always a reliable indication of dehydration, it has traditionally been used as the solely available parameter to determine dehydration in different studies[21,32,33].

A graphical diagram of the attachment and removal of the sweat collection patches including locations and distances is shown in Figure 9.

Two absorbent patches were adhered to the lower back of each of the 20 volunteers. Figure 10 shows a picture of one of the fabricated patches (left) and its placement on the back of one of the volunteers (right). The first sweat patch collection point was set at 5 km from the start of the race, where the participants are presumed to be hydrated and in well condition. The second sweat patch collection point was set at end of the race, where dehydration is more likely to appear in participants that do not follow a correct hydration plan.

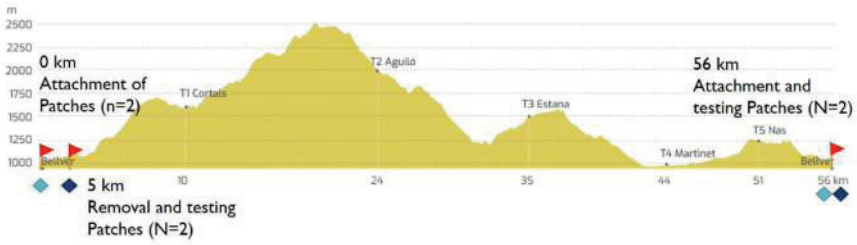

Figure 9. Patches attachment and removal points in the *TRAIL PIRINEU 2019.* Light blue points indicate the attachment of the sweat collection patches and dark blue points the removal and sweat analysis.

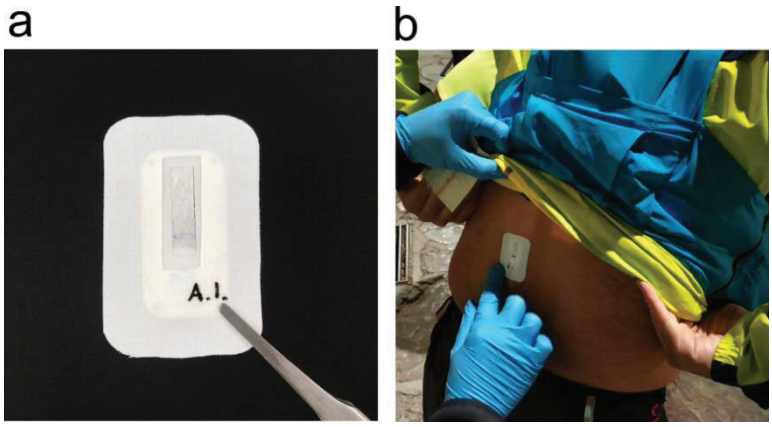

Figure 10. a) Image of the a sweat absorbent patch and b) patch being attached to the lower back of volunteer before the mountain race *TRAIL PIRINEU 2019.*

The protocol for sweat collection and measurement was set as follows. First, the skin of the volunteers was cleaned using 96º reinforced alcohol for topical use and let it to dry. Then, two identical patches were attached to the lower back of the participants in order to analyse the reproducibility of the adhesion, collection and measurement methods. After 5 km of the starting point of the race, the sweat absorbent patches were removed from the users and introduced in a closed wet reservoir to avoid sweat evaporation before the conductivity measurement. It has to be remarked that at this point, the full amount of sweat patches were completely saturated. After patch collection, the sweat conductivity measurement was performed following the same procedure used in the laboratory calibration phase. Two conductivity values were obtained from each volunteer, which allowed to obtain an estimation of the coefficient of variation between measurements of

identical patches. Results are shown in Figure 11. The conductivity values obtained from the two patches applied to each volunteer did not differ more than a 10% (black bar) in the 75% of the cases. Only in four of the volunteers, higher differences in the conductivity values obtained from the two patches were observed (blue bar) whereas in two other cases, one of patches did not deliver any reliable result (red bar).

Sweat was collected again at the finish line of the race. Immediately after their arrival, the volunteers were directed to a specific zone where they were submitted again to the measurement protocol previously described. During the sweat absorption interval, the participant was asked to undress, weight himself on a scale and rest on a stretcher during the collection of a blood sample. Figure 12 displays a detail of the back of one of the volunteers during sweat collection.

After sweat collection, conductivity measurements were performed using the same procedure as previously described. Unfortunately, almost half of the volunteers did not provide a sufficient volume of sweat to measure conductivity, probably due to the fact that the nudity of the participants increased the sweat evaporation rate and helped them to regulate the body temperature, stopping in this way skin perspiration. This unexpected effect diminished the number of suitable samples. Figure 13 shows the obtained results. Only the patches collected from 10 out of 20 volunteers delivered a reliable result in both patches and allowed the comparison of their conductivity values. From this, only in seven of the volunteers the obtained values presented a coefficient of variation of the measured conductivity of less than 10% (black bar) and in three cases the measured conductivity differs too much (blue bar) to be acceptable.

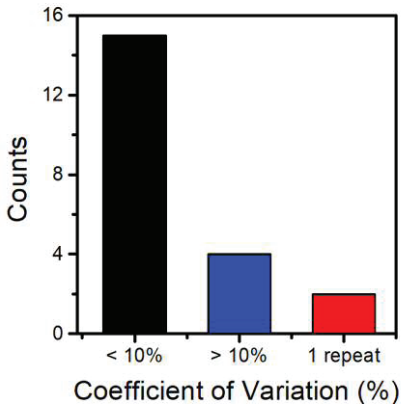

Figure 11. Coefficient of variation of the conductivity values obtained for each participant when measuring the conductivity in the two sweat absorbent patches at +5 km from the start of the race.

Only the data obtained from the volunteers in which sweat conductivity measurements presented a coefficient of variation of less than 10% both at the beginning of the race first conductivity measurement) and at the end (second conductivity measurement) were used in the dehydration analysis. Table 1 presents the average conductivity values extracted from the two patches at the starting and ending points of the race and the relative variation between them. The participants labelled as dehydrated according to the results of the blood biochemical analysis have been marked with an asterisk.

Figure 12. Image of two sweat absorbent patch attached to the lower back of volunteer at the end of the mountain race *TRAIL PIRINEU 2019* while the sweat was being absorbed.

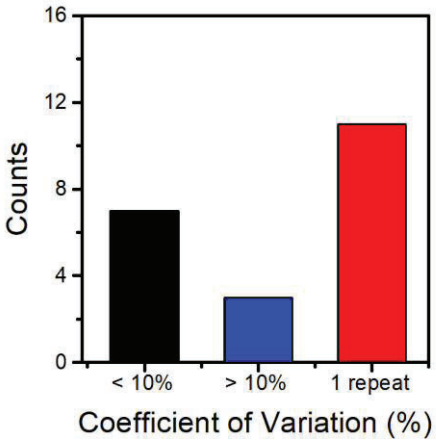

Figure 13. Coefficient of variation of the conductivity values obtained for each participant when measuring the conductivity of the two sweat absorbent patches at the end of the race.

Table 1. Conductivity values obtained from each participant at the different stages of the race, and the relative variation between the two points. The asterisk shows the dehydrated volunteers determined by the blood biochemical analysis.

Volunteer	Concentration start (mM eq NaCl)	Concentration end (mM eq NaCl)	Concentration relative variation (%)	Percentage of Weigh loss (%)
*E**	38	71	88	-3.9
*G**	72	68	5	-5.0
*H**	44	67	54	-5.3
*J**	67	40	2	-4.9
*L**	28	69	42	-4.0
M	51	49	4	-2.9
*O**	41	38	6	-4.0

Our procedure recorded a high relative variation of the conductivity in 3 of the 7 volunteers (E, H and L) that also corresponded to a dehydrated status according to blood analisis and the percentatge of body weight loss (dehydration is supposed to occur when percentatge of body weight loss is higher than a 3%). However, it can also be noticed that sweat conductivity did not change significantly or it even decresed in other 3 of the participants (G, J and O) despite their blood analysis and weight loss indicated dehydration.

As an attempt to stablish a conductivity variation threshold that could potentially assess dehydration, the relative variation of sweat conductivity of every participant was compared with the percentage of body mass loss (since it has been widely used to evaluate dehydration[21,32,33]. Figure 14 shows the ROC curve in which the threshold was extracted with the nearest point from the top left corner of the ROC curve, corresponding to a relative variation of sweat conductivity of 49%, with a sensitivity of 62.5% and a specificity of 100% and an AUC of 0.781.

Although the obtained results were not conclusive in terms of dehydration assessment, the experiment allowed to verify the feasibility and efficiency of the absorption and measurement methodology of sweat in volunteers and set the basis to perform a more precise test with controlled individuals in a subsequent phase of the project.

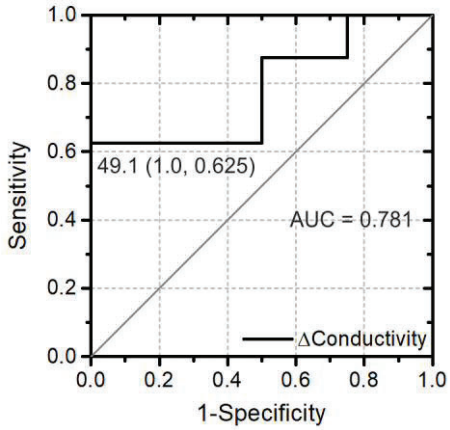

Figure 14. ROC curve of the relative variation of conductivity as dehydration marker

Self-powered sweat sensor, study of two different designs to maximize the device performance

Once conductivity measurements on the sweat patch with commercial impedimetric electrodes were validated, the next objective was to integrate the self-powered conductivity measurement capability inside the patch. To do so, two different designs of the battery-sensor were explored in order to minimize the total sweat volume needed while maximizing the voltage output sensitivity and linearity evaluating its intrinsic variation.

The two paper-based battery designs shared the same chemistry that has been widely described and tested along the previous chapters of this thesis. Therefore, the battery electrodes consisted of a magnesium anode (Mg) and a silver/silver chloride cathode (Ag/AgCl) which undergo the oxidation and reduction reactions respectively.

As in the previous chapters, the two electrodes were positioned side-by-side in a coplanar configuration, while a paper-based matrix is placed on top and connects the two electrodes. It has been also assessed that the electrolyte volume – mainly driven by the paper thickness and its water absorption capacity – has a direct influence on the device sensitivity and dynamic range. By increasing the thickness and the water absorption capacity of the paper-based matrix used in the device, the battery sensor turns to be less resistive (more similar to a traditional drop configuration of the conductivity measurements), which decreases its sensitivity but increases its dynamic range. We

observed this effect by testing two battery with two different paper matrixes. The first design included a glass fiber with a thickness of 250 µm and a water absorption capacity of 25.3 mg·cm^{-2} (LF1 paper from GE, already used along this thesis) whereas the second design incorporated a polyester-fiber of 420 µm thickness and 57 mg·cm^{-2} of water absorption (6614 from Ahlstrom). Figure 15 shows a schematic representation of both configurations.

In this case, differently from the devices presented in the previous chapters, a single paper-based layer was chosen for the design of the two battery candidates. This is because the amount of sweat available to be obtained during exercise is very limited, so the study was performed with a single paper-based matrix with different volume requirements (in the order of tens of µL).

Glass fiber membranes consist of abundant extremely fine fibers of glass with a capillary structure that allows liquid holding and filtration. The fibers are biochemically inert, which makes them very suitable for electrochemical purposes[34,35]. Polyester-fibers were initially developed for clothing and furniture business but in the last years have been also applied in the diagnostic field. They are especially suited for blood filtration in chromatographic applications[36]. Glass fiber and polyester-fiber were preferred in this work to more traditional diagnostic materials such as cellulose because they do not change in volume (i.e. expand) upon water absorption.

To observe the effect of the paper-based matrix properties on the performance of the batteries, an exhaustive characterization of each design was performed. Due to the single-use nature of our batteries, 30 batteries were built - 15 with the glass fiber and 15 with the polyester matrix. NaCl water-based samples with salt contents from 10 mM to 80 mM were

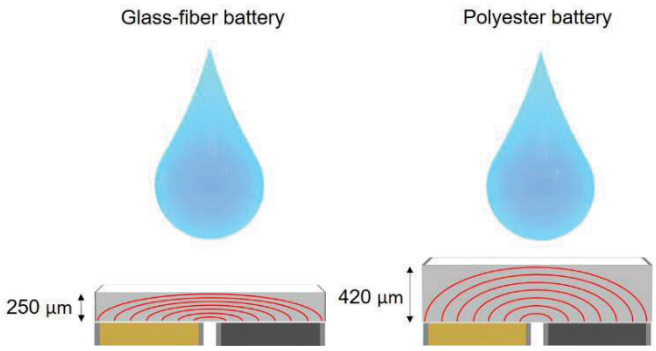

Figure 15. Schematic of the two different batteries used for this study. Red lines represent theoretical ion conduction paths between the electrodes.

prepared and tested with a laboratory conductimeter and then introduced in the battery sensors. Three repeats were performed at each conductivity. The characterization of the battery was done by performing a linear sweep voltammetry (LSV) at 10 mV·s^{-1}, departing from the open circuit voltage of the battery to 0 V. The obtained results are displayed in Figure 16.

The effective electrolyte resistance of the battery at a given conductivity can be derived from the slope of the ohmic region of the IV curve presented by the batteries. Figure 17 shows the internal resistance of the batteries versus the resistivity of the ionic solution.

As it can be observed in Figure 17, the polyester-fiber matrix showed lower internal resistance values due to its higher thickness. However, the relative change of internal resistance along the whole measurement range of conductivities is lower than for the glass fiber batteries. To derive information about the conductivity of the liquid used to activate the battery in a self-powered mode - as shown in chapter 2 - an external resistive element (R_{LOAD}) was connected in series to the battery, so its voltage output is proportional to the electrolyte conductivity. The value of the R_{LOAD} must be equal to the internal resistance of the battery at a given conductivity to maximize the sensitivity at that particular conductivity value. Therefore, the expected output voltages of the battery when connected to different R_{LOAD} values (within the range of experimental internal resistances) were extracted from the intersection between the I-V curves of the battery and R_{LOAD} for the glass-fiber battery as shown in Figure 18a. Figure 18b shows the expected output voltages vs ionic salt

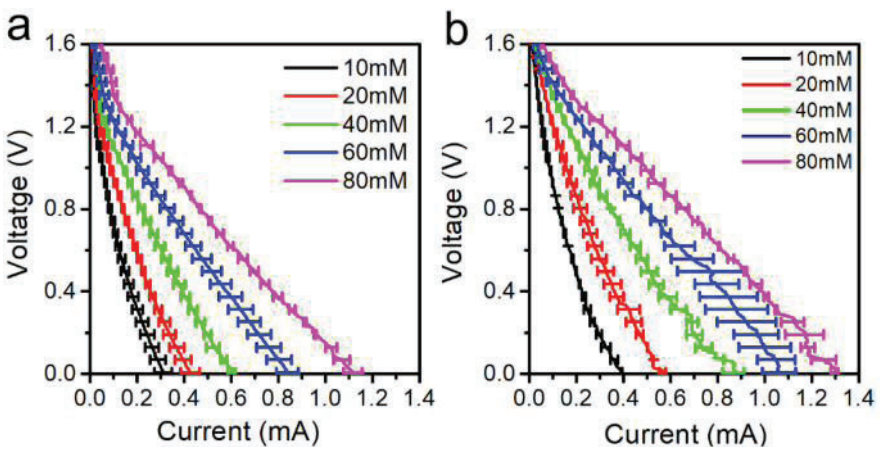

Figure 16. IV curves of the battery mounted with a) the LF1 glass fiber and b) 6614 polyester-fiber fiber activated with solutions of 10 to 80 mM NaCl. Lines represent mean values, error bars represent ± one standard deviation, for N = 3.

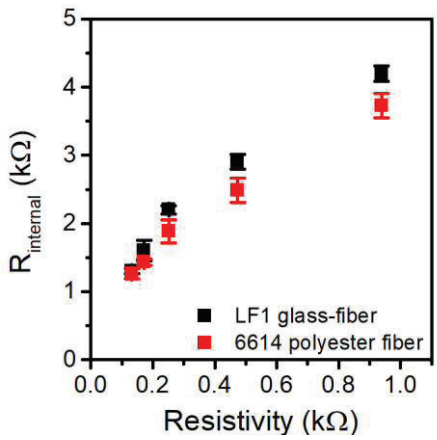

Figure 17. Internal resistance of the battery depending on the electrolyte resistivity comparing two different paper-based matrices. Data points represent mean values, error bars represent ± one standard deviation, for N = 3.

concentrations. Linearity along the dynamic range was calculated from the voltage outputs obtained at each R_{LOAD} for the two battery types, as shown in Figure 19. The same analysis was done with the polyester-fiber battery; results are shown in Figure 20 and Figure 21.

As presented in Figure 19 the voltage output of the LF1 glass-fiber battery presents different linearities depending on the external resistor connected in series. In addition, it is

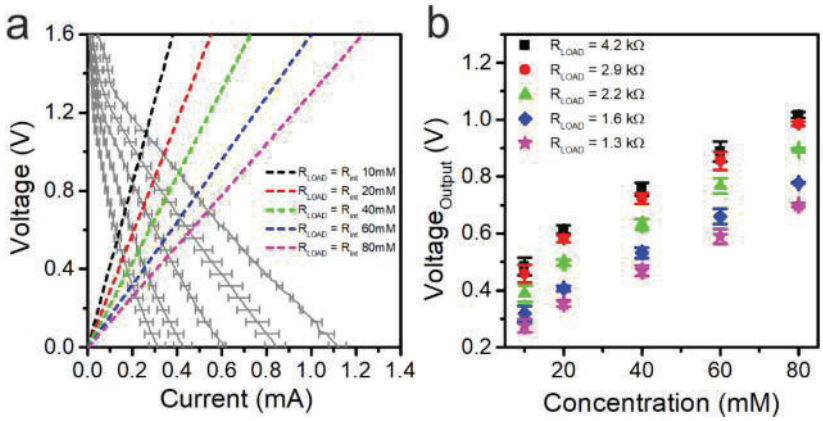

Figure 18. LF1 glass-fiber battery voltage output. a) Intersection of the different R_{LOADS} to assess the voltage output of the battery depending on the conductivity of the electrolyte. b) Voltage output depending on the connected R_{LOAD}. Lines and data points represent mean values, error bars represent ± one standard deviation, for N = 3.

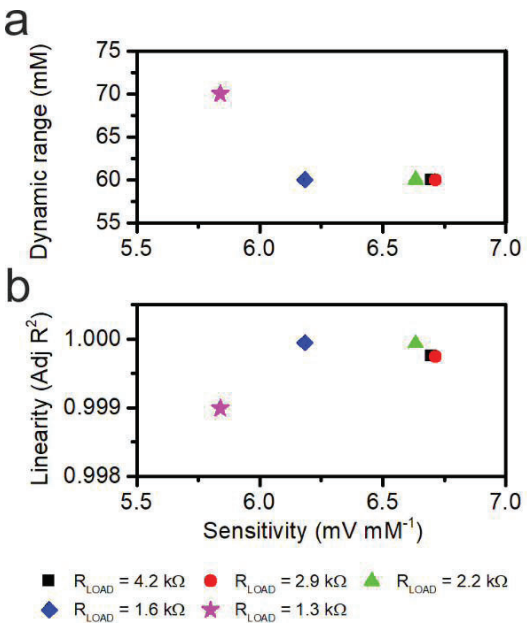

Figure 19. Analysis of the LF1 glass-fiber battery. a) Dynamic range vs Sensitivity and b) Linearity vs Sensitivity of the battery depending on the R_{LOAD} connected in series.

shown the sensitivities in the corresponding dynamic range that can be obtained as a function of the resistor connected. As it can be observed in Figure 19a the dynamic range of measurement can be maximized by using the external resistor of 1.3kΩ but having the lowest sensitivity that can be obtained (5.8 mV mM^{-1}). In this configuration, as it can be observed in Figure 19b the linear relationship between the voltage output and the NaCl concentration is the lowest of the range but still high with a 0.999 of adjusted R^2. In contrast, choosing any other resistor within the range presented, higher linearities and sensitivities can be obtained but not permit the measurement in the whole range of concentration (from 10mM to 80mM of NaCl). For these reasons, the best candidate chosen for a subsequent analysis of the LF1 glass-fiber battery was the R_{LOAD} of 1.3kΩ.

In Figure 21 the 6614 polyester-fiber voltage output characteristics depending on R_{LOAD} are presented. As it can be observed in Figure 21a the dynamic range of the battery changes dramatically depending on the resistor connected. Again, the maximum dynamic range can be obtained with the lowest R_{LOAD} presenting the highest sensitivity (6.9 mV mM^{-1}) at the expense of linearity which is the lowest that can be obtained (Figure 21b). Because the objective is to analyse sweat conductivity in the whole range con concentrations, the R_{LOAD} of 1.2 kΩ was the final resistor selected.

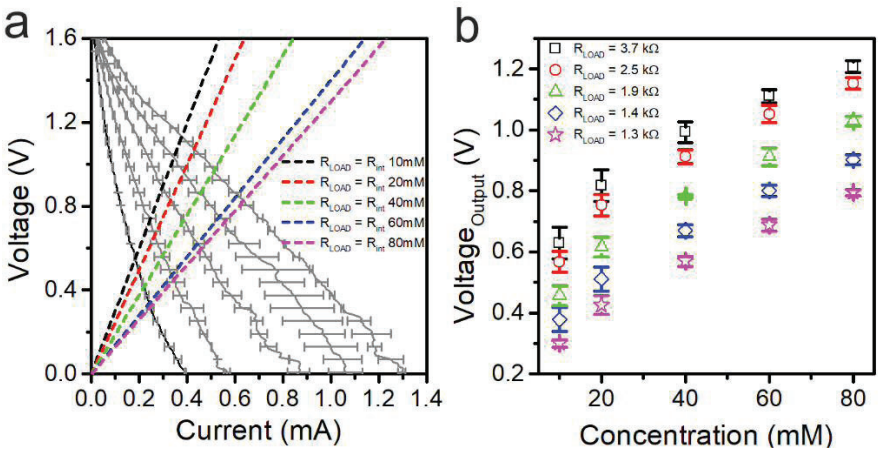

Figure 20. 6614 polyester-fiber battery voltage output. a) Intersection of the different R_{LOADS} to assess the voltage output of the battery depending on the conductivity of the electrolyte. b) Voltage output depending on the connected R_{LOAD}. Lines and data points represent mean values, error bars represent ± one standard deviation, for N = 3.

As it has been previously explained in this thesis, the intersection of a R_{LOAD} with the IV curve is only an estimative tool to predict the actual voltage output provided by the battery under continuous operation. Therefore, measurements of the output voltage at the same

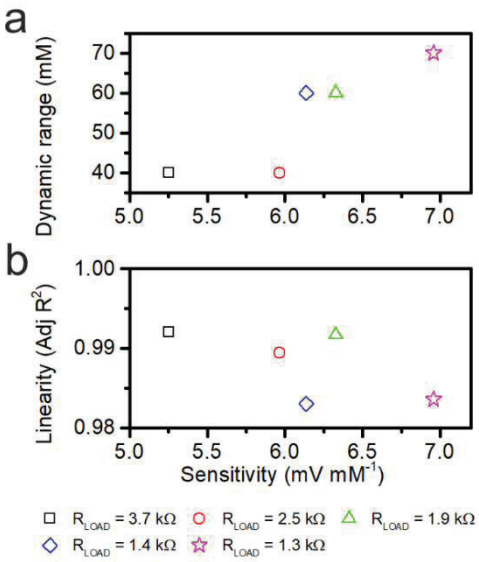

Figure 21. Analysis of the 6614 polyester-fiber battery. a) Dynamic range vs Sensitivity and b) Linearity vs Sensitivity of the battery depending on the R_{LOAD} connected in series.

NaCl concentrations used in the IV battery calibration were performed. First, the liquid sample was poured inside the battery paper core and the voltage was let to stabilize at the battery open circuit potential (V_{OCP}) during 5 seconds. Then, optimal R_{LOAD} for each battery (1.3 kΩ and 1.2 kΩ for the LF1 glass-fiber and 6614 polyester-fiber battery respectively) was connected in series to the battery. The battery voltage was recorded for 30 seconds. The obtained results are shown in Figure 22.

Figure 22 shows that the voltage output provided by the batteries during the measurement time of 30 seconds experiences a slight and monotonous increase when activated with

low-conducting ionic solutions. This is probably due to the slow dissolution of the oxide passivation layer at the anode that at low chloride concentrations takes place at slower rates. In order to follow a traceable criterion, the highest voltage value of every transient response was taken as a representative output voltage related to the conductivity of the electrolyte. In fact, with the objective in mind to develop minimalistic devices, the connection of a single capacitor in parallel to the resistor may be a simple way of registering the maximum voltage achieved by the battery along the measurement period. The addition of a diode to prevent the capacitor discharge would turn the capacitor into a memory of the device behaviour for a period of time. Figure 23 shows the maximum voltage achieved by the batteries versus the NaCl content of the activating solutions.

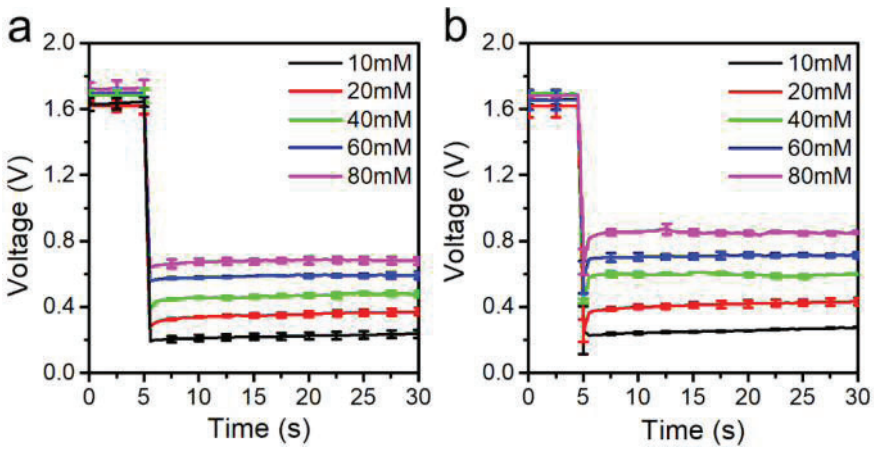

Figure 22. Transient response during 30 seconds from a) LF1 glass-fiber battery when connecting in series a resistor of 1.3 kΩ and b) 6614 polyester-fiber battery when connecting in series a resistor of 1.2 kΩ. Lines represent mean values, error bars represent ± one standard deviation at specific times, for N = 3.

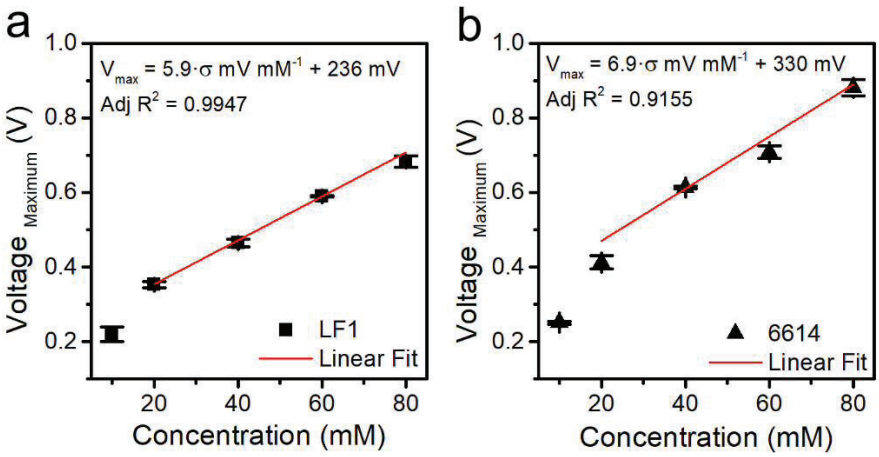

Figure 23. Maximum voltage output of both batteries a) LF1 glass-fiber battery and b) 6614 polyester-fiber battery. Data points represent mean values, error bars represent ± one standard deviation, for N = 3.

It can be seen in Figure 23a that the battery implemented with the LF1 glass-fiber shows a linear behaviour in the range from 20 mM to 80 mM NaCl concentration. At 10 mM NaCl the pre-existent passivation layer over the magnesium anode, which has not been totally removed during the 30 s of battery operation, introduces an additional resistance that diminishes the voltage of the battery, and hence the linearity or linear relationship between the maximum voltage output versus the NaCl concentration. Even the shortening of the dynamic range of the battery, the sensitivity is maintained unaltered with respect to the first calculations with the intersection with the IV battery response (Figure 19). Figure 23b shows the maximum voltages achieved by the battery containing the polyester-fiber. In this case, even the sensitivity is almost the same as the sensitivity calculated from the IV battery response it has been calculated from 20 to 80mM NaCl and the linearity is clearly worse than in the IV calculations.

Contrary to the strategy followed in the previous chapters, in this case the output voltage of the battery has been fitted to a linear function. Even the dynamic range of conductivities being measured is similar, in this case, the effect of having only one layer of paper-based matrix, in contrast to the batteries from chapter 2 to 4 which had two layers, makes the new battery more resistive, linearizing the voltage output of the battery in front of conductivity. As explained before, the decision to introduce a single paper-based matrix rather than two is because the amount of sweat that can be obtained during exercise is very limited.

To summarize, the characteristics considered for the selection of the best battery design to be incorporated inside the patch are shown in Table 2.

Table 2. Battery characteristics

Battery	**Volume required**	**Voltage Output sensitivity**	**Dynamic range**	**Linearity**	**Intrinsic variation**
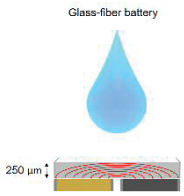	8.5 µL	5.9 mV mM^{-1}	20 – 80 mM	0.9947	2%
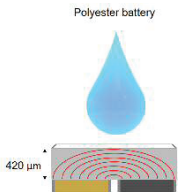	18.5 µL	6.9 mV mM^{-1}	20 – 80 mM	0.9155	2%

Linearity of the output signal of the battery is always preferred, as it allows for a simple signal interpretation and processing. In addition, in this particular application, linearity is very convenient since dehydration monitoring will be based on a differential measurement of the sweat conductivity from the same individual. A linear signal dependence allows to associate the voltage difference obtained during a certain period to a difference in conductivity regardless the absolute conductivity values (which are not informative as independent values) and so the hydration monitoring can be reliably performed in a very easy way. Based on this sole criterion, the battery with the glass-fiber core was selected as the best candidate to perform the conductivity measurement of sweat for dehydration assessment despite its sensitivity is slightly lower than the polyester-based battery. This prototype offers the additional advantage of requiring a smaller amount of sweat to operate (8.5 µL).

Testing of the self-powered sensor with artificial eccrine perspiration and real sweat

Once the selection of the most suitable battery to perform the conductivity measurement of sweat was done, the objective was to test the conductivity battery-sensor with artificial

eccrine perspiration and real sweat samples and compare the results provided by the battery with the ones obtained with a commercial portable conductometer. The selected commercial device used as reference was the LAQUAtwin EC-33 model from HORIBA. This device is a compact conductometer, which requires 120 μL to perform conductivity measurements in different water-based samples such as rain, rivers, lake or aquariums.

Before measuring real sweat samples, the two conductivity sensors were calibrated using artificial eccrine perspiration solutions as a way to test their performance in a more realistic matrix than NaCl solutions prepared in the laboratory. The artificial eccrine perspiration sample used in this test was the same as in Chapter 4 (from Pickering Laboratories), the composition of which has already been described. To obtain artificial perspiration samples with the conductivities in the range of the NaCl solutions used for device calibration, the samples were adjusted in conductivity by diluting them and measuring their conductivity values with a laboratory conductometer. Table 3 shows the conductivity of the different concentration of NaCl solutions used for adjusting the artificial perspiration samples conductivities.

Table 3. Conductivity of bare NaCl samples used for adjusting the conductivity of artificial eccrine perspiration samples

Concentration (mM)	**Conductivity ($mS \cdot cm^{-1}$)**	**Standard Deviation of Conductivity ($mS \cdot cm^{-1}$)**
10	1.02	0.03
20	2.01	0.01
40	3.83	0.10
60	5.68	0.05
80	7.54	0.05

Afterwards, the testing of the conductivity battery sensor and the LAQUAtwin EC-33 with artificial eccrine perspiration samples was performed. For the battery sensor, as in the calibration, the sample was introduced inside the battery and the V_{OCP} was measured during 5 seconds to allows voltage stabilization. Then, a R_{LOAD} of 1.3 kΩ was connected in series to the battery and the output voltage of the battery was recorded for 30 seconds. Then, the highest voltage value of every transient response was extracted and compared with the values previously recorded with NaCl solutions (Figure 23a). The results are displayed in Figures 24.

As it can be observed in Figure 24a, the conductivity battery sensor presented a stable performance when introducing the different perspiration samples at different conductivities. In Figure 24b, the voltage output with the two different matrixes – artificial perspiration and NaCl solutions - is represented. It can be observed that the performance of the batteries activated with different matrixes did not differ significantly. However, the battery output voltages seem to be slightly lower when measuring the artificial eccrine perspiration samples. This phenomenon might be attributed to the sample composition as, apart from ions, the presence of different amount of proteins and other components may increase the resistivity of the electrolyte and the dispersion of the device (as represented by the red error bars). To convert the maximum voltage provided by the battery to a conductivity value, the calibration curve used was the one obtained with the artificial eccrine perspiration samples. Figure 25 shows the calibration curve and the linear regression which relates the maximum voltage output provided by the battery with the conductivity. As it can be observed from Figure 25, the linear relationship of the maximum voltage output of the battery as a function of the conductivity is maintained until the saturation of the sensor is reached for conductivities over 6 mS·cm^{-1}. The LAQUAtwin EC-33 conductometer was then tested with the artificial eccrine perspiration samples. The conductivity values obtained with the LAQUAtwin EC-33 are represented against the conductivity values obtained during the preparation of the samples with the conductometer 914 pH/Conductometer from Metrohm in Figure 26.

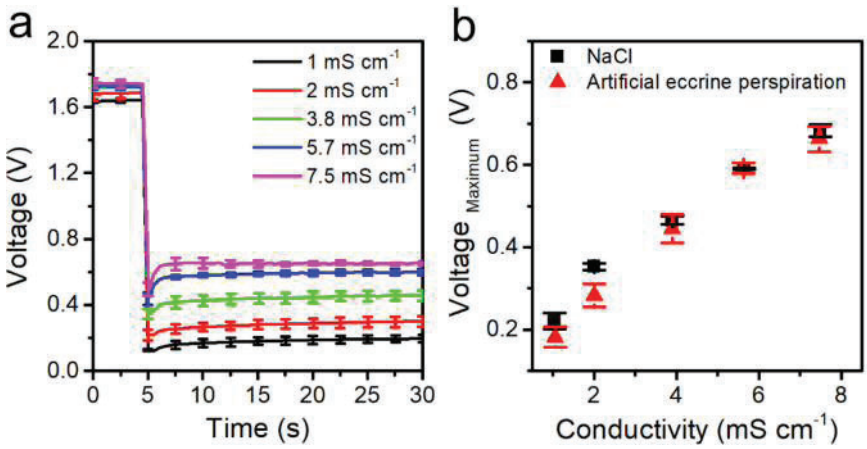

Figure 24. a) Transient response of the LF1 glass-fiber battery using artificial eccrine perspiration samples and b) Comparison between the voltage output provided by the battery when analysing NaCl samples (black squares) and artificial eccrine perspiration (red triangles). Data points represent mean values, error bars represent ± one standard deviation, for N = 3.

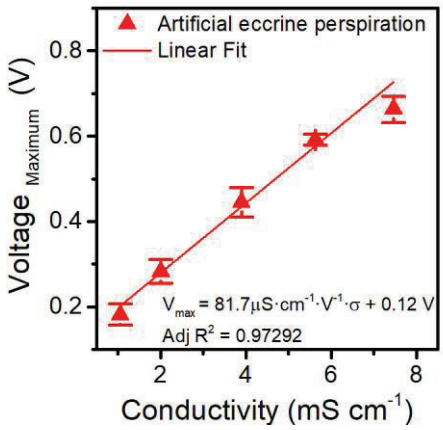

Figure 25. Calibration curve of the paper-based conductivity battery sensor calibrated with artificial eccrine perspiration samples and the equation governing the relationship between voltage output and conductivity. Data points represent mean values, error bars represent ± one standard deviation, for N = 3.

As it can be observed from Figure 26, the conductivity values provided by the LAQUAtwin EC-33 differ from the measured by the laboratory conductometer with a systematic error.

The LAQUAtwin EC-33 provided very precise conductivity measurements, with triplicates yielding a coefficient of variation of less than a 3%, but systematically higher than the reference values, i.e. the device showed a constant sensitivity of 1.15 in comparison to the

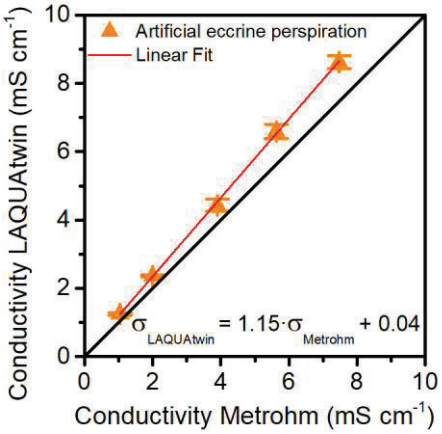

Figure 26. LAQUAtwin EC-33 conductivity measurements from the eccrine perspiration samples at different conductivities. Data points represent mean values, error bars represent ± one standard deviation, for N = 3.

laboratory conductometer. Taking this into account, it was decided to use this curve (formula shown in Figure 26) as the calibration curve to refer the conductivity values obtained from the LAQUAtwin EC-33 to the conductivity of the 914 pH/Conductometer from Metrohm, which has higher metrological characteristics.

Once the two conductometers were recalibrated with artificial perspiration samples, both devices were tested with real sweat obtained from volunteers during a low-intensity physical activity test. The main goal of the test was to get sweat samples from the skin of the lower back of the volunteers and measure them with our self-powered conductivity battery-sensor and the commercial conductometer in order to assess the performance and reliability of the batteries in real conditions. In this case, the sweat samples were collected from a group of volunteers from our Institute, Institute of Microelectronics of Barcelona. To perform the test, an information sheet for the participants and an informed consent for sample donation were submitted to the ethics committee of the *Consejo Superior de Investigaciones Científicas* (CSIC) to ensure the legal implication of the participants (see Annex 3). The selected participants declared to have between 25 and 60 years, that practiced sports at least two days per week and that were able to perform a low intensity physical activity (see Annex 4).

For this test, a sweat collector patch was designed with a collection area large enough to absorb the required sample to fill the devices under test. The batteries required 8.5 µL to yield a result whereas the LAQUAtwin EC-33 needed 120 µL. The paper selected to implement the collector patch was the polyester-fiber 6614 from Ahlstrom. Figure 27 shows an exploded vision of the layers that are integrated in the patch as well as a picture of one of the ready-to-use patches.

To attach the sweat collector patch to the volunteers, the same protocol as in the mountain race *ULTRA PIRINEU 2019* was followed. First, the skin was cleaned using ethanol and let to dry and then, two patches were attached in the lower back of the volunteer in order to analyse the reproducibility of the conductivity measurement. In this case, the volunteers were asked to perform moderate physical activity (running, jumping…) and return every 15 minutes to a check point, where the research team checked the level of sweat volume collected in the patch. Figure 28 shows an image of two sweat collectors being attached to the lower back skin of a volunteer at the beginning of the test. Once the patches reached saturation, they were removed from the volunteers skin and squeezed inside a syringe. The syringe content was stored in Eppendorf containers for further analysis. The conductivity results provided by the self-powered conductivity sensor and the LAQUAtwin EC-33 can be observed in Figure 29.

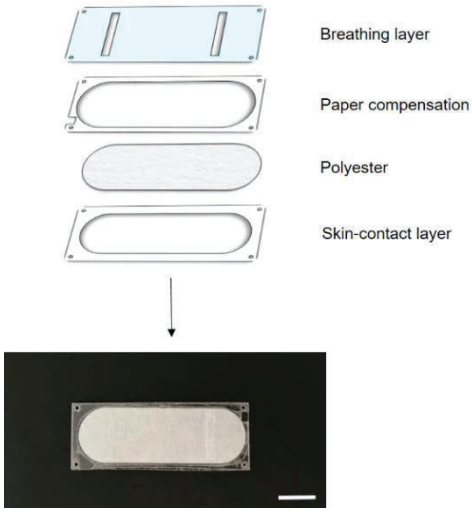

Figure 27. Sweat collector patch design and final fabricated device (scale bar = 1 cm).

The measurements obtained with our self-powered conductivity sensor show a high degree of correlation with the ones obtained by the recalibrated LAQUAtwin EC-33. The 79% of the results obtained with our device presented a deviation with respect to the LAQUAtwin EC-33 lower than 10% (represented in Figure 29 with green triangles). The 10% of the results presented deviations between 10 and 20% whereas another 10% yielded deviations higher than 20% (data represented with blue and pink triangles respectively). Therefore, considering that the battery sensors are fabricated manually; we can conclude that our self-powered conductivity sensor is able to measure the conductivity real sweat satisfactorily in the 79% of the cases.

Figure 28. Image of a sweat collector patch being attached to the lower back of a volunteer.

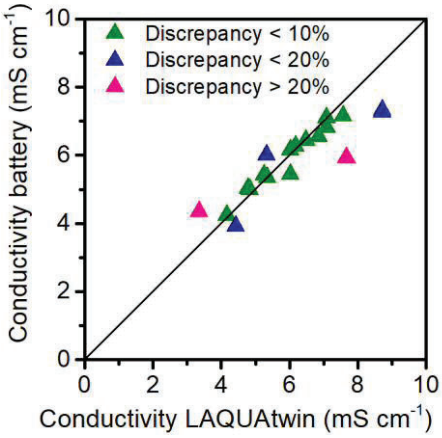

Figure 29. Comparison of the conductivity values obtained with the battery sensor and the commercial LAQUAtwin conductometer.

Conclusions

In this chapter, we have demonstrated the feasibility of developing different types of absorbent patches to collect sweat and measure its conductivity in a reproducible manner. Different structures of the paper-based conductivity battery sensor have been explored with the objective of maximizing the battery sensor dynamic range. The paper-based conductivity battery sensor has demonstrated to be able to measure the conductivity of real sweat with a high accuracy and precision with respect to a commercial portable conductometer. Further steps towards the integration of the self-powered capability inside the patch that allow obtaining in-vivo conductivity values of sweat and even continuous sweat monitoring are the natural steps to continue the research line started in this chapter.

Regarding the assessment of dehydration through the increase of sweat conductivity values, the obtained results have not yet been conclusive. Further experiments with more control of the liquid intake of the participants as well as the intensity of their physical activity are to be performed. However, the experiments allowed verifying the feasibility and efficiency of the sweat absorption patches as well as the validation of the methodology employed to obtain and measure sweat in volunteers in a real scenario. This clearly sets the basis to perform a more precise test with controlled individuals in the future.

References

(1) Wearable Technology Market Size | Industry Report, 2020-2027 https://www.grandviewresearch.com/industry-analysis/wearable-technology-market (accessed Nov 1, 2020).

(2) Sreenilayam, S. P.; Ahad, I. U.; Nicolosi, V.; Acinas Garzon, V.; Brabazon, D. Advanced Materials of Printed Wearables for Physiological Parameter Monitoring. *Materials Today*. January 1, 2020, pp. 147–177. https://doi.org/10.1016/j.mattod.2019.08.005.

(3) Svertoka, E.; Rusu-Casandra, A.; Marghescu, I. State-of-the-Art of Industrial Wearables: A Systematic Review. *International Conferencce on Communications.* July 16, 2020. pp. 411–415. https://doi.org/10.1109/comm48946.2020.9141982.

(4) Seneviratne, S.; Hu, Y.; Nguyen, T.; Lan, G.; Khalifa, S.; Thilakarathna, K.; Hassan, M.; Seneviratne, A. A Survey of Wearable Devices and Challenges. *IEEE Communications Surveys and Tutorials*. October 1, 2017. pp. 2573–2620. https://doi.org/10.1109/COMST.2017.2731979.

(5) John Dian, F.; Vahidnia, R.; Rahmati, A. Wearables and the Internet of Things (IoT), Applications, Opportunities, and Challenges: A Survey. *IEEE Access.* 2020, pp 69200–69211. https://doi.org/10.1109/ACCESS.2020.2986329.

(6) Brezulianu, A.; Geman, O.; Dan Zbancioc, M.; Hagan, M.; Aghion, C.; Hemanth, D. J.; Son, L. H. IoT Based Heart Activity Monitoring Using Inductive Sensors. *Sensors.* July 26, 2019. pp. 3284 (1-16). https://doi.org/10.3390/s19153284.

(7) Majumder, A. J. A.; Elsaadany, Y. A.; Young, R.; Ucci, D. R. An Energy Efficient Wearable Smart IoT System to Predict Cardiac Arrest. *Advances in Human-Computer Interaction.* February 12, 2019. pp. 1-21 https://doi.org/10.1155/2019/1507465.

(8) Yang, G.; Deng, J.; Pang, G.; Zhang, H.; Li, J.; Deng, B.; Pang, Z.; Xu, J.; Jiang, M.; Liljeberg, P.; et al. An IoT-Enabled Stroke Rehabilitation System Based on Smart Wearable Armband and Machine Learning. *IEEE Journal of Translational Engineering in Health and Medicine.* May 8, 2018, pp. 2100510 (1-10). https://doi.org/10.1109/JTEHM.2018.2822681.

(9) Sistema flash de monitorización de glucosa | FreeStyle Libre https://www.freestylelibre.es/libre/ (accessed Nov 1, 2020).

(10) Kim, J.; Imani, S.; de Araujo, W. R.; Warchall, J.; Valdés-Ramírez, G.; Paixão, T. R. L. C.; Mercier, P. P.; Wang, J. Wearable Salivary Uric Acid Mouthguard Biosensor with Integrated Wireless Electronics. *Biosensors and Bioelectronics.* December 15, 2015. pp. 1061–1068. https://doi.org/10.1016/j.bios.2015.07.039.

(11) Tseng, P.; Napier, B.; Garbarini, L.; Kaplan, D. L.; Omenetto, F. G. Functional, RF-Trilayer Sensors for Tooth-Mounted, Wireless Monitoring of the Oral Cavity and Food Consumption. *Advanced Materials.* March 23, 2018. pp. 1703257 (1-7). https://doi.org/10.1002/adma.201703257.

(12) Park, J.; Kim, J.; Kim, S. Y.; Cheong, W. H.; Jang, J.; Park, Y. G.; Na, K.; Kim, Y. T.; Heo, J. H.; Lee, C. Y.; et al. Soft, Smart Contact Lenses with Integrations of

Wireless Circuits, Glucose Sensors, and Displays. *Science Advances.* January 24, 2018. eaap9841. https://doi.org/10.1126/sciadv.aap9841.

(13) Sonner, Z.; Wilder, E.; Gaillard, T.; Kasting, G.; Heikenfeld, J. Integrated Sudomotor Axon Reflex Sweat Stimulation for Continuous Sweat Analyte Analysis with Individuals at Rest. *Lab on a Chip.* July 4, 2017. pp. 2550–2560. https://doi.org/10.1039/c7lc00364a.

(14) Reeder, J. T.; Choi, J.; Xue, Y.; Gutruf, P.; Hanson, J.; Liu, M.; Ray, T.; Bandodkar, A. J.; Avila, R.; Xia, W.; et al. Waterproof, Electronics-Enabled, Epidermal Microfluidic Devices for Sweat Collection, Biomarker Analysis, and Thermography in Aquatic Settings. *Science Advances.* January 25, 2019. eaau6356. https://doi.org/10.1126/sciadv.aau6356.

(15) Kim, S. B.; Koo, J.; Yoon, J.; Hourlier-Fargette, A.; Lee, B.; Chen, S.; Jo, S.; Choi, J.; Oh, Y. S.; Lee, G.; et al. Soft, Skin-Interfaced Microfluidic Systems with Integrated Enzymatic Assays for Measuring the Concentration of Ammonia and Ethanol in Sweat. *Lab on a Chip.* November 20, 2020. pp. 84–92. https://doi.org/10.1039/c9lc01045a.

(16) Emaminejad, S.; Gao, W.; Wu, E.; Davies, Z. A.; Nyein, H. Y. Y.; Challa, S.; Ryan, S. P.; Fahad, H. M.; Chen, K.; Shahpar, Z.; et al. Autonomous Sweat Extraction and Analysis Applied to Cystic Fibrosis and Glucose Monitoring Using a Fully Integrated Wearable Platform. *Proceedings of the National Academy of Sciences of the United States of America.* April 17, 2017. pp. 4625–4630. https://doi.org/10.1073/pnas.1701740114.

(17) Chen, Y.; Lu, S.; Zhang, S.; Li, Y.; Qu, Z.; Chen, Y.; Lu, B.; Wang, X.; Feng, X. Skin-like Biosensor System via Electrochemical Channels for Noninvasive Blood Glucose Monitoring. *Science Advances.* December 20, 2017. pp. e1701629. https://doi.org/10.1126/sciadv.1701629.

(18) Qiao, L.; Rose Benzigar, M.; Subramony, J. A.; Lovell, N. H.; Liu, G. Advances in Sweat Wearables: Sample Extraction, Real-Time Biosensing, and Flexible Platforms. *Applied Materials and Interfaces.* June 24, 2020. pp. 34361. https://doi.org/10.1021/acsami.0c07614.

(19) Barnes, K. A.; Anderson, M. L.; Stofan, J. R.; Dalrymple, K. J.; Reimel, A. J.; Roberts, T. J.; Randell, R. K.; Ungaro, C. T.; Baker, L. B. Normative Data for Sweating Rate, Sweat Sodium Concentration, and Sweat Sodium Loss in Athletes: An Update and Analysis by Sport. *Journal of Sports Sciences.* June 22, 2019. pp. 2356–2366. https://doi.org/10.1080/02640414.2019.1633159.

(20) Sawka, M. N.; Burke, L. M.; Eichner, E. R.; Maughan, R. J.; Montain, S. J.; Stachenfeld, N. S. Exercise and Fluid Replacement. *Medicine and Science in Sports and Exercise.* February 2007. pp. 377–390. https://doi.org/10.1249/mss.0b013e31802ca597.

(21) Cheuvront, S. N.; Kenefick, R. W. Dehydration: Physiology, Assessment, and Performance Effects. *Comprehensive Physiology.* January 10, 2014. pp. 257–285. https://doi.org/10.1002/cphy.c130017.

(22) Cheuvront, S. N.; Kenefick, R. W.; Charkoudian, N.; Sawka, M. N. Physiologic Basis for Understanding Quantitative Dehydration Assessment. *The American Journal of Clinical Nutrition.* January 23, 2013. pp. 455–462.

https://doi.org/10.3945/ajcn.112.044172.

(23) Baker, L. B. Physiology of Sweat Gland Function: The Roles of Sweating and Sweat Composition in Human Health. *Temperature.* July 17, 2019. pp. 211-259. https://doi.org/10.1080/23328940.2019.1632145.

(24) Baker, L. B. Sweating Rate and Sweat Sodium Concentration in Athletes: A Review of Methodology and Intra/Interindividual Variability. *Sports Medicine*. March 1, 2017, pp 111–128. https://doi.org/10.1007/s40279-017-0691-5.

(25) Lara, B.; Gallo-Salazar, C.; Puente, C.; Areces, F.; Salinero, J. J.; Del Coso, J. Interindividual Variability in Sweat Electrolyte Concentration in Marathoners. *Journal of the International Society of Sports Nutrition.* July 29, 2016. pp. 31. https://doi.org/10.1186/s12970-016-0141-z.

(26) Morgan, R. M.; Patterson, M. J.; Nimmo, M. A. Acute Effects of Dehydration on Sweat Composition in Men during Prolonged Exercise in the Heat. *Acta Physiologica Scandinavica.* August 26, 2004. pp. 37–43. https://doi.org/10.1111/j.1365-201X.2004.01305.x.

(27) Armstrong, L. E.; Hubbard, R. W.; Szlyk, P. C.; Matthew, W. T.; Sils, I. V. Voluntary Dehydration and Electrolyte Losses during Prolonged Exercise in the Heat. *Aviation, Space, and Environmental Medicine.* August 1, 1985. pp. 765–770.

(28) Walsh, R. M.; Noakes, T. D.; Hawley, J. A.; Dennis, S. C. Impaired High-Intensity Cycling Performance Time at Low Levels of Dehydration. *International Journal of Sports Medicine.* October 1994. pp. 392–398. https://doi.org/10.1055/s-2007-1021076.

(29) Havenith, G.; Fogarty, A.; Bartlett, R.; Smith, C. J.; Ventenat, V. Male and Female Upper Body Sweat Distribution during Running Measured with Technical Absorbents. *European Journal of Applied Physiology.* December 7, 2008. pp. 245–255. https://doi.org/10.1007/s00421-007-0636-z.

(30) Baker, L. B.; Barnes, K. A.; Anderson, M. L.; Passe, D. H.; Stofan, J. R. Normative Data for Regional Sweat Sodium Concentration and Whole-Body Sweating Rate in Athletes. *Journal of Sports Sciences.* May 22, 2015. pp. 358–368. https://doi.org/10.1080/02640414.2015.1055291.

(31) Ultra Pirineu 2020 https://ultrapirineu.com/es (accessed Nov 3, 2020).

(32) Tam, N.; Noakes, T. D. The Quantification of Body Fluid Allostasis During Exercise. *Sports Medicine.* August 18, 2013. pp. 1289–1299. https://doi.org/10.1007/s40279-013-0089-y.

(33) Shirreffs, S. M.; Sawka, M. N. Fluid and Electrolyte Needs for Training, Competition, and Recovery. *Journal of Sports Science.* 2011. pp. S39-S46. https://doi.org/10.1080/02640414.2011.614269.

(34) Fang, X.; Wei, S.; Kong, J. Paper-Based Microfluidics with High Resolution, Cut on a Glass Fiber Membrane for Bioassays. *Lab on a Chip.* January 8, 2014. pp. 911–915. https://doi.org/10.1039/c3lc51246k.

(35) Jones, K. FUSION 5: A New Platform For Lateral Flow Immunoassay Tests. In *Lateral Flow Immunoassay*. November 6, 2008. pp 1–15. https://doi.org/10.1007/978-1-59745-240-3_7.

(36) Nilghaz, A.; Ballerini, D. R.; Guan, L.; Li, L.; Shen, W. Red Blood Cell Transport Mechanisms in Polyester Thread-Based Blood Typing Devices. *Analytical and Bioanalytical Chemistry.* July 11, 2015. pp. 1365–1371. https://doi.org/10.1007/s00216-015-8845-5.

CONCLUSIONS

This thesis presents for the first time a method and a device that enable self-powered conductivity measurements. Although many self-powered electrochemical devices have been presented in last decade, all of them allowed determining analyte concentrations with amperometric techniques (i.e.oxidation or reduction reactions) in which such analytes acted as fuel. Here, the new approach is based on making use of the effect of the ionic conductivity of a battery electrolyte on its internal resistance. The internal resistance of a battery affects its power output. By applying this principle in fluid-activated batteries – where the fluid acts as electrolyte- a very simple operating device is derived.

Departing from this simple concept, the thesis focuses on the implementation of single use self-powered devices by relying on three technological drivers: printed electronics, paper microfluidics and the use of self-powering strategies. These three pillars allow demonstrating the feasibility of implementing reliable, robust and self-powered, but also ASSURED digital devices with high Technology Readiness Levels (TRLs). The devices have followed the whole development process from conception and design to the fabrication of Proof-of-Concept devices that are tested with laboratory calibrated samples and then, validated with artificial samples mimicking real fluids or with real biological samples in a relevant environment.

During the technological progress of the thesis, both the capacities and the limitations of the novel self-powered conductimetric devices have been identified and discussed. First, the technologies used for the development of the devices allow for the fabrication of rapid, low cost and reproducible prototypes but with a limited sensitivity, dynamic range of measurement (from 0.5 to 10 mS cm^{-1}) and resolution. Second, the chemistry used for the implementation of this paper-based conductivity battery-sensor turned to be unreliable to determine conductivity of natural waters or consumer drinks due to the interaction of the magnesium anode with certain salts like phosphate, sulphate, etc… However, it has proven to be very suitable for biological fluids, in which these interfering salts are present

in very small concentrations. Last, the developed self-powered operating devices have been all designed to use a very limited number of electronic components in order to minimize cost, printability and environmental impact. However, this choice has limited the information delivered by the devices to provide a digital semi-quantitative result, meaning that the results – although unambiguous in terms of interpretation - provides a result related to conductivity threshold (i.e. values under or above a pre-defined value set by design).

The outlook of this thesis remains open, since many modifications can be introduced, to solve the drawbacks found during the thesis execution or to tackle new applications:

1. The electrodes manufacturing processes and physical configuration could be modified in order to obtain better sensitivities in the whole range of conductivities of biological fluids (from 0.5 to 40 $mS \cdot cm^{-1}$).
2. The storing and wireless transmission of the output voltage of the paper-based conductivity battery-sensor during a continuous monitoring will allow the quantification and digitalization of the result in external memories or database, to finally build a health-related conductivity big data.
3. Other in-vitro applications were the conductivity needs to be measured in a very simple manner could be addressed, or due to the biocompatibility of the oxidising and reducing electrodes in the battery in-vivo conductivity determinations could be done.

In the future, some of the implemented self-powered ASSURED digital devices will be used in clinical trials, were subsequent improvements will be introduced inside the devices. Other applications such as the dry eye diagnosis will be tackled by the miniaturization of the conductivity battery sensor. Finally, more complex electronic modules will be studied in order to obtain the full capabilities of the paper-based conductivity battery-sensor to obtain more intelligent devices making steps towards digital health.

SCIENTIFIC CONTRIBUTIONS

Journal articles

- Ortega, L.; Llorella, A.; Esquivel, J. P.; Sabaté, N. Self-Powered Smart Patch for Sweat Conductivity Monitoring. *Microsystems Nanoeng.* 2019, *5* (1). https://doi.org/10.1038/s41378-018-0043-0.

- Ortega, L.; Llorella, A.; Esquivel, J. P.; Sabaté, N. Paper-Based Batteries as Conductivity Sensors for Single-Use Applications. *ACS Sensors* 2020, *5* (6), 1743–1749. https://doi.org/10.1021/acssensors.0c00405.

- Rodriguez-Villarreal, A. I.; Ortega-Tana, L.; Cid, J.; Hernandez-Machado, A.; Alarcon-Cor, T.; Miribel-Catala, P.; Colomer-Farrarons, J. An Integrated Detection Method for Flow Viscosity Measurements in Microdevices. *IEEE Trans. Biomed. Eng.* 2020, 1–1. https://doi.org/10.1109/tbme.2020.3013519.

Patent

- Ortega, Tañá Laura and Llorella, Bustins Anna and Esquivel, Bojorquez Juan Pablo and Sabaté, Vizcarra Neus. 2020. A DEVICE AND A METHOD FOR SENSING THE CONDUCTIVITY OF A FLUID. EP Patent 3676606, filed Mar 11, 2019, and issued Jul 08, 2020.

Workshops and Conferences

- Congress: Large Organic Printed Electronics Congress (LOPEC). Munich, Germany 2018.
  Type: Attendance.

- Congress: Large Organic Printed Electronics Congress (LOPEC). Munich, Germany 2019.
  Type: Oral.

Title: Self-powered smart patch for sweat conductivity monitoring.

- Congress: Smart Systems Integration (SSI). Barcelona, Spain 2019.
  Type: Poster.
  Title: Self-powered smart patch for sweat conductivity monitoring

- Congress: 2019 Spring Meeting European Materials Research Society (E-MRS). Nice, France 2019.
  Type: Oral.
  Title: Self-powered patch for sweat conductivity measurement.

- Congress: International Meeting on Chemical Sensors (MATRAFURED). Visegrád, Hungary.
  Type: Oral.
  Title: Paper Fuel Cells and Batteries as Enablers of Self-powered Diagnostic Devices.

SUMMARY

This thesis presents the development of different self-powered devices that allow the conductivity measurement of liquid samples, from different types of water samples to biological fluids. The devices have been developed with the aim of offering robust single-use systems following the criteria dictated by the WHO for Point of Care (PoC) devices, the ASSURED criteria (Affordable, Sensitive, Specific, User-friendly, Rapid and robust, without equipment and deliverable to end users). For the development of these devices, three technological drivers have been used, such as printed electronics, paper microfluidics and self-powered systems. With the combination of these three technologies, three very different prototypes have been developed for the conductivity analysis of different samples, proving a digital and unequivocal result.

In the first chapter, an introduction about the motivation for the development of ASSURED devices and how the use of the three technological drivers allows obtaining fully functional single-use devices is done. For this, the state of the art on the three technological drivers and their integration for the development of ASSURED self-powered digital devices is evaluated.

The second chapter delves into the basic unit that allows devices to be self-powered, a paper-based conductivity battery-sensor. This chapter explains the bases that allow this battery to be sensitive to the conductivity of the electrolyte introduced into its paper core and how a signal directly related to the conductivity of the electrolyte can be extracted from the battery. Finally, the battery is tested with different liquids, demonstrating its suitability for the analysis of biological samples.

In the third chapter, the first self-powered device for measuring different types of water is developed. It contains two interconnected conductivity battery-sensor that allow the measurement of the conductivity of the electrolyte, a hybrid circuit manufactured by inkjet

printing were discrete electronic components have been hybridized and an electrochromic indicator that shows the value of the conductivity of the electrolyte in a scale-bar.

In the fourth chapter, a medical device in the form of a skin patch is manufactured for the screening of Cystic Fibrosis. The patch has been designed following the standards dictated by the Cystic Fibrosis Foundation and the CLSI (Clinical and Laboratory Standards Institute) for the development of a screening device. The patch also contains two connected conductivity battery-sensor, a printed circuit hybridized with electronic components and two electrochromic indicators, which indicate whether or not the disease is present. The performance of the patch was validated using samples of artificial sweat samples at the threshold conductivity of Cystic Fibrosis patients and at -20% of the threshold conductivity.

Finally, the fifth chapter presents the first steps in the development of a patch capable of storing the sweat of athletes for the subsequent analysis with the conductivity battery-sensor. First, the design of the patch was validated in a local race where two patches were placed on different participants and then the conductivity was measured, obtaining very similar results (coefficient of variation of less than 10% in the 75% of the subjects). Next, different conductivity sensor battery structures were evaluated to obtain the best possible performance in terms of dynamic range of measurement, sensitivity and linearity. Once the best battery structure was decided, its performance was compared to that of a commercial conductivity meter using real sweat samples. From this study, it was observed that the conductivity values provided by the battery differ from the commercial conductometer in less than 10% in 68% of the cases, between 10 and 20% in 21% of the cases and more than 20% in 11% of cases, thus concluding the effectiveness of our battery measurement in 68%.

RESUMEN

Esta tesis presenta el desarrollo de diferentes dispositivos autoalimentados que permiten la medida de la conductividad de muestras líquidas, desde diferentes tipos de aguas a fluidos biológicos. Los dispositivos se han desarrollado con el objetivo de ofrecer sistemas robustos de un solo uso siguiendo los criterios dictados por la OMS para dispositivos Point of Care (PoC), los criterios de ASSURED (Affordable, Sensitive, Specific, User-friendly, Rapid and robust, Equipment-free and Deliverable to end-users). Para el desarrollo de estos dispositivos se han utilizado tres impulsores tecnológicos como son la utilización de la electrónica impresa, de la microfluídica en papel y de sistemas autoalimentados. Con la combinación de estas tres tecnologías se han desarrollado tres prototipos muy diferentes para el análisis de la conductividad de diferentes muestras, proporcionando un resultado digital e inequívoco.

En el primer capítulo se hace una introducción sobre la motivación del desarrollo dispositivos ASSURED y de cómo la utilización de los tres impulsores tecnológicos permite la obtención de dispositivos de un solo uso completamente funcionales. Para ello se evalúa el estado del arte sobre los tres impulsores tecnológicos y su integración para el desarrollo de dispositivos digitales autoalimentados ASSURED.

En el segundo capítulo se profundiza en la unidad básica que permite la autoalimentación de los dispositivos, una batería sensora de conductividad basada en papel. En este capítulo se explican las bases que permiten que esta batería sea sensible a la conductividad del electrolito introducido en su núcleo de papel y cómo se puede extraer de la batería una señal directamente relacionada con la conductividad del electrolito. Finalmente, la batería se prueba con diferentes líquidos, dejando patente su idoneidad para el análisis de muestras biológicas.

En el tercer capítulo se desarrolla el primer dispositivo autoalimentado para la medida de

diferentes tipos de aguas. Éste contiene dos baterías sensoras de conductividad interconectadas que permiten la medida de la conductividad del electrolito, un circuito híbrido fabricado por electrónica impresa y al que se le han hibridado componentes electrónicos discretos y un indicador electrocrómico que muestra el valor de la conductividad del electrolito en una escala de niveles.

En el cuarto capítulo se fabrica un dispositivo médico en forma de parche para la piel para el cribado de la Fibrosis Quística. El parche se ha diseñado siguiendo los estándares dictados por la Fundación de Fibrosis Quística y el CLSI (Clinical and Laboratory Standards Institute) para el desarrollo de un dispositivo de cribado. El parche contiene también dos baterías sensoras de conductividad conectadas entre ellas, un circuito impreso hibridado con componentes electrónicos y dos indicadores electrocrómicos, que indican si se tiene o no la enfermedad. El funcionamiento del parche se validó utilizando muestras de sudor artificial a la conductividad umbral que presentan los pacientes de Fibrosis Quística y a un -20% de la conductividad umbral.

Finalmente, en el quinto capítulo se presentan los primeros pasos del desarrollo de un parche capaz de almacenar el sudor de deportistas para su posterior análisis con la batería sensora de conductividad. Primero se validó el diseño del parche en una cursa local donde se colocaron dos parches a una serie de participantes de la cursa después se les midió la conductividad obteniendo resultados muy similares entre sí (con un coeficiente de variación de menos de un 10% en el 75% de los sujetos). Seguidamente, se evaluaron diferentes estructuras de baterías sensoras de conductividad para obtener el mejor rendimiento posible en términos de rango dinámico de medida, sensibilidad y linealidad. Una vez se decidió cual era la mejor estructura de la batería, se comparó su rendimiento con el de un conductímetro comercial utilizando muestras de sudor reales. De este estudio se observó que los valores de conductividad proporcionados por la batería distaban del comercial en menos de un 10% en el 68% de los casos, entre un 10 y un 20% en un 21% de los casos y más de un 20% en un 11% de los casos, concluyendo así la efectividad de la medida de nuestra batería en un 68%.

ANNEX 1: Approval of the Clinical Research Ethics Committee (CEIm) of Sant Joan de Déu Hospital

Dra. Neus Riba Garcia
Secretaria técnica del CEIm Fundació Sant Joan de Déu

CERTIFICA

1º. Que el CEIC Fundació Sant Joan de Déu en su reunión del día 27/02/2020, ha evaluado la propuesta del promotor referida al estudio:
Título: "POWERPATCH Parche cutáneo autónomo e inteligente para el diagnóstico de Fibrosis Quística".
Código Interno: PS-04-20
IP: María Cols Roig

Documentos con versiones:

- Protocolo, versión 1.0 13 de diciembre de 2019.
- Hoja de información al participante adulto y Hoja de Consentimiento de Participante adulto, versión 1.0 de 13 de diciembre de 2019.
- Hoja de información al progenitor o tutor legal del participante pediátrico y Hoja de Consentimiento de los padres o tutor legal del menor participante, versión 1.0 13 de diciembre de 2019.
- Hoja de información al participante pediátrico > 12 años, versión 1.0 13 de diciembre de 2019.

Considera que:

- El proyecto se plantea siguiendo los requisitos del RD 1591/2009, de 16 de octubre, por el que se regulan los productos sanitarios o el RD 1616/2009, de 26 de octubre, por el que se regulan los productos sanitarios implantables activos, según corresponda.
- Su realización es pertinente.
- Se cumplen los requisitos necesarios de idoneidad del protocolo en relación con los objetivos del estudio y están justificados los riesgos y molestias previsibles para el sujeto.
- Son adecuados tanto el procedimiento para obtener el consentimiento informado como la compensación prevista para los sujetos por daños que pudieran derivarse de su participación en el estudio.
- El alcance de las compensaciones económicas previstas no interfiere con el respeto a los postulados éticos.
- La capacidad de los Investigadores y los medios disponibles son apropiados para llevar a cabo el estudio.

1º. Por lo que este CEIm emite un **DICTAMEN FAVORABLE.**

2º. Este CEIm acepta que dicho estudio sea realizado en los siguientes CEIm/Centros por los Investigadores:
HOSPITAL SANT JOAN DE DÉU. María Cols Roig

y hace constar que:

1º En la reunión celebrada el día 27/02/2020, acta 05/2020 se decidió emitir el informe correspondiente al estudio de referencia.

2º El CEIm de la Fundació Sant Joan de Déu, tanto en su composición como en sus PNTs, cumple con las normas de BPC (CPMP/ICH/135/95)

Fundació privada per a la Recerca i la Docència Sant Joan de Déu NIF: G-62978689

Edifici Docent Sant Joan de Déu - c. Santa Rosa, 39-57, 3ª planta, 08950 Esplugues de Llobregat / Barcelona
Telèfon +34 93 600 97 51 - Fax +34 93 600 97 71 e-mail: info@fsjd.org web: www.fsjd.org

3º Listado de miembros:

Presidente	Dr. Jesús Pineda Sánchez (Medicina - Pediatría)
Vicepresidente	Dr. Bernabé Robles (Medicina – Neurología)
Secretaria técnica	Dra. Neus Riba García (Farmacología Clínica)
Vocales	Hno. Fernando Aguiló Martinez (Medicina Tropical)
	Sra. Clara Chamorro Pérez (Jurista)
	Dra. Ofelia Cruz Martínez (Medicina – Oncología)
	Sr. Ángel del Campo Escota (Representante de las asociaciones de pacientes)
	Dra. Beatriz del Pino Gaya (Farmacia hospitalaria)
	Dr. Pau Ferrer Salvans (Farmacología Clínica)
	Dr. Sabel Gabaldon Fraile (Medicina – Psiquiatría)
	Dra. Ana Maria Martin Ancel (Medicina – Neonatología)
	Dra. Laura Martínez Rodríguez (Profesora titular - Campus Docent SJD)
	Sr. Eduard Puig Vaquero (Jurista – Delegado protección de datos)
	Sra. María Eugenia Rey Abella (Farmacia AP)
	Dra. Marisa Serra Alacid (Medicina – Unidad Atención al Usuario)
	Dr. Joan Vinent Genestar (Farmacia hospitalaria)
	Dra. Cecilia Jiménez Mallebrera – (Bióloga, genetista y representante del CR)

En el caso de que se evalúe algún proyecto del que un miembro sea investigador/colaborador, este se ausenta de la reunión durante la discusión del proyecto.

Lo que firmo en Esplugues de Llobregat,

Fdo:

Dra. Neus Riba García
Secretaria técnica del CEIm Fundació Sant Joan de Déu

Fundació privada per a la Recerca i la Docència Sant Joan de Déu NIF: G-62978689

Edifici Docent Sant Joan de Déu - c. Santa Rosa, 39-57, 3ª planta, 08950 Esplugues de Llobregat / Barcelona
Telèfon +34 93 600 97 51 - Fax +34 93 600 97 71 e-mail: info@fsjd.org web: www.fsjd.org

ANNEX 2: Approval of the *Agencia Española del Medicamento y Productos Sanitarios* (AEMPS)

PS/CR

810/20/EC

AUTORIZACION DE INVESTIGACIONES CLINICAS

Visto el procedimiento iniciado por la Fundación Sant Joan de Déu, como promotor de la investigación clínica "POWERPATCH PARCHE CUTÁNEO AUTÓNOMO E INTELIGENTE PARA EL DIAGNÓSTICO DE LA FIBROSIS QUÍSTICA", nº expte. 810/20/EC, en solicitud de autorización de la misma.

Tramitado el procedimiento conforme a lo dispuesto en el Título IV de la Ley 39/2015, de 1 de octubre, del Procedimiento Administrativo Común de las Administraciones Públicas y, consideradas las disposiciones establecidas en el capítulo VIII del Real Decreto 1591/2009, de 16 de octubre, por el que se regulan los productos sanitarios y el Real Decreto 1275/2011, de 16 de septiembre, por el que se crea la Agencia estatal "Agencia Española de Medicamentos y Productos Sanitarios" y se aprueba su estatuto.

En su virtud, a propuesta del Departamento de Productos Sanitarios, y en el uso de las atribuciones que me están conferidas, he resuelto

AUTORIZAR la realización de la investigación clínica indicada en las condiciones y términos que figuran en el expediente, en el centro sanitario siguiente:

- Hospital Sant Joan de Déu (Esplugues de Llobregat - Barcelona)

Contra esta resolución que agota la vía administrativa puede interponerse potestativamente recurso de reposición ante la Directora de la Agencia Española de Medicamentos y Productos Sanitarios en el plazo de un mes, conforme a lo dispuesto en los artículos 123 y 124 de la Ley 39/2015, de 1 de octubre del Procedimiento Administrativo Común de las Administraciones Públicas, o interponerse recurso contencioso-administrativo ante el Juzgado Central de lo contencioso-administrativo de la Comunidad Autónoma de Madrid, en el plazo de dos meses a contar desde el día siguiente a la recepción de la presente notificación, conforme a lo dispuesto en la Ley reguladora de la Jurisdicción Contencioso-Administrativa de 13 de julio de 1998, y sin perjuicio de cualquier otro recurso que pudiera interponerse.

Mediante este documento se Notifica a Dª. Silvia Martínez Rabasa (Av. Meridiana 350, 9ºD; 08027 Barcelona), la presente resolución, según lo exigido en el artículo 40 de la mencionada Ley 39/2015, de 1 de octubre, del Procedimiento Administrativo Común de las Administraciones Públicas.

DIRECTORA DE LA AGENCIA ESPAÑOLA DE MEDICAMENTOS Y PRODUCTOS SANITARIOS

Mª Jesús Lamas Díaz

Agencia Española de Medicamentos y Productos Sanitarios
Fecha de la firma: 09/07/2020
Puede comprobar la autenticidad del documento en la sede de la AEMPS: https://sede.aemps.gob.es
Localizador: J 3 Q 3 L E D D 2 6

CORREO ELECTRÓNICO
psinvclinic@aemps.es

C/ CAMPEZO, 1 - EDIFICIO 8
28022 MADRID
Tel.: (+34) 91.822.54.99
Fax: (+34) 91.822.52.89

ANNEX 3: Approval of the Ethics Committee of the *Consejo Superior de Investigaciones Científicas* (CSIC)

INFORME DE EVALUACIÓN BIOÉTICA/BIOSEGURIDAD

Evaluados los aspectos de bioética de la investigación propuesta (Investigación con la participación de seres humanos, el manejo de sus muestras y/o datos que requieren protección) y, según los términos definidos en el proyecto, el Comité de Ética del CSIC declara que no existen objeciones que puedan constituir impedimento alguno para su desarrollo.

Para que conste a los efectos oportunos, se expide el presente informe de evaluación en Madrid, a diecisiete de agosto de dos mil veinte.

Datos del Investigador principal

Nombre	SABATÉ VIZCARRA, NEUS
Centro / Instituto	Instituto de Microelectrónica de Barcelona – IMB (Bellaterra, Barcelona)
Teléfono	935947700
Correo electrónico	neus.sabate@imb-cnm.csic.es;

Datos de la Investigación propuesta

Título	Actividad de título "Validación técnica de sensor de conductividad con muestras de sudor humana", contemplada en el proyecto "Digital and Disposable Patch for Dehydration Monitoring (D2PATCH)"
Convocatoria	AGAUR – Industria del Conocimiento – Producte 2018
Referencia	-

Evaluación

FAVORABLE

Código interno: 138/2020

CONSEJO SUPERIOR DE INVESTIGACIONES CIENTÍFICAS * COMITÉ DE ÉTICA CSIC

Lluís Montoliu José
Presidente del Comité de Ética del CSIC

Este informe solo tiene validez para la investigación propuesta y en las condiciones en ella descritas. Cualquier cambio que afecte a las implicaciones bioéticas y/o de bioseguridad de la misma, invalida este informe y deberá ser puesto en conocimiento del Comité de Ética del CSIC para su valoración.

C/ SERRANO, 117
28006 MADRID, ESPAÑA
TEL.: 91 5681494-91 5681554
comitedeetica@csic.es

ANNEX 4: Informed consent for sample donation and participation in an investigation

HOJA DE INFORMACIÓN AL PARTICIPANTE

TÍTULO DEL PROYECTO:	DIGITAL AND DISPOSABLE PATCH FOR DEHYDRATION MONITORING (D2PATCH)
PROMOTOR/FINANCIADOR:	AYUDA PRODUCTE – PROGRAMA INDUSTRIA DEL CONOCIMIENTO 2018 (AGAUR – GENERALITAT DE CATALUNYA)
INVESTIGADOR/ES RESPONSABLE/S:	NEUS SABATÉ VIZCARRA
CARGO:	INVESTIGADORA ICREA
DEPARTAMENTO/UNIDAD:	MICROENERGY SOURCES AND SENSORS
CENTRO DE ADSCRIPCIÓN:	INSTITUTO DE MICROELECTRÓNICA DE BARCELONA (IMB-CNM)
LUGAR DONDE SE REALIZARÁ EL ESTUDIO:	INSTITUTO DE MICROELECTRÓNICA DE BARCELONA (IMB-CNM)
TELÉFONO:	+34935947700
E-MAIL:	NEUS.SABATE@IMB-CNM.CSIC.ES

I. INTRODUCCIÓN

Le entregamos este documento para informarle sobre una actividad de investigación aprobada por el Comité de Ética del CSIC en la que se le invita a participar de forma voluntaria. Para ello, le rogamos que lea esta hoja informativa con atención y nos consulte cualquier mínima duda que le surja.

II. DESCRIPCIÓN GENERAL DE LA INVESTIGACIÓN

El objetivo del proyecto D2PATCH es desarrollar un parche para la monitorización de la deshidratación de un deportista a partir de la medida de la conductividad su sudor. Específicamente, esta investigación tiene como objetivo la validación del funcionamiento del sensor de conductividad de un sólo uso desarrollado en el proyecto D2PATCH con muestras de sudor humanas. Para ello, se precisa la participación de voluntarios a producir sudor en una prueba física de baja intensidad (caminar, saltar, agitar los brazos, carrera leve sin desplazamiento) durante un tiempo estimado de 5-15 minutos hasta que los parches muestren una saturación completa. El funcionamiento del parche se ha probado en laboratorio con muestras cuya composición se acerca mucho al sudor y con sudor artificial comercial. Esta investigación es de gran importancia ya que con ella se podrá obtener sudor real de los voluntarios y con ella comprobar el funcionamiento del dispositivo en condiciones más cercanas a la realidad.

III. NATURALEZA DE LA PARTICIPACIÓN

Su participación en esta investigación es totalmente voluntaria y por ello, usted puede decidir participar o no. De igual modo, puede cambiar su decisión y revocar su consentimiento en cualquier momento, sin que esto le afecte en modo alguno.

Para participar en la investigación, usted debe tener entre 25 y 60 años y declarar que practica deporte de una forma habitual (2 veces o más por semana).

Usted declara también que no tienen ninguna vinculación con la investigación ni el grupo que desarrolla la investigación.

BENEFICIOS

Los beneficios de la investigación incluyen el poder probar el parche de sudor desarrollado en el proyecto D2PATCH con sudor real, mejorando así el grado de madurez del dispositivo para su posterior comercialización. Por otro lado, le medida de conductividad realizada por el dispositivo en desarrollo se comparará con la obtenida con un dispositivo comercial (LAQUATWIN EC-33) validando así su correcto funcionamiento.

Usted no recibirá ninguna compensación económica ni otros beneficios materiales por el hecho de participar en la investigación ni por ceder las muestras.

RIESGOS

Por ser voluntario de la investigación, debe saber que incurre en diferentes riesgos o inconvenientes como podrían ser:

- Riesgo de alergia: El papel que se le enganchará en la piel es de grado médico y ha pasado diferentes certificaciones de biocompatibilidad pero podría causarle alguna alergia en la zona de aplicación.
- Riesgo físico: aunque la actividad que se contempla es de baja intensidad (caminar, saltar, agitar los brazos, carrera leve sin desplazamiento) podría sufrir molestias debido a la actividad como la fatiga o la sudoración excesiva.
- Inversión de tiempo: la actividad que se contempla en la investigación tendrá una duración total aproximada de entre 30 a 45 minutos que incluirá la cumplimentación de un formulario, la preparación de la prueba, la actividad física, la extracción de la muestra de sudor y finalmente la limpieza de la zona de absorción. También deberá considerar la posibilidad de que una vez finalizada la prueba, sea necesario contactar con usted a fin de recabar nuevos datos u obtener nuevas muestras; en tal caso usted tendrá la potestad de negarse a este nuevo requerimiento.

RESPONSABILIDAD DEL EQUIPO

Usted no recibirá ninguna compensación económica ni otros beneficios materiales por el hecho de participar en la investigación ni por ceder las muestras.

IV. PROCEDIMIENTOS

Los datos necesarios para la investigación se obtendrán a partir de la cumplimentación de un formulario previo a la actividad física. En este formulario se le requerirá la siguiente información: edad, estatura y peso.

Para obtener la muestra de sudor, se requerirá que siga un protocolo por el cual el equipo de investigación le guiará en todo momento. El protocolo para la obtención de la muestra se detalla a continuación con los tiempos aproximados para cada paso:

1. Limpieza de la parte baja de la espalda con alcohol (1 min)
2. Pegado del papel absorbente de grado médico en la zona limpia (1 min)
3. Realización de una fotografía de la zona para posterior análisis (30 seg)
4. Realización de la actividad física leve mientras el papel absorbente va colectando el sudor (5 – 15min)

5. Finalización de la actividad física leve
6. Despegado del papel absorbente (1 min)
7. Almacenamiento del sudor colectado en un recipiente estéril (1 min)
8. Limpieza de la zona de absorción con alcohol (1 min)

V. INFORMACIÓN RELATIVA A DATOS Y/O MUESTRAS

En materia de protección de datos, se dará cumplimiento a lo contemplado en el REGLAMENTO (UE) 2016/679 DEL PARLAMENTO EUROPEO Y DEL CONSEJO de 27 de abril de 2016 relativo a la protección de las personas físicas en lo que respecta al tratamiento de datos personales y a la libre circulación de estos datos y por el que se deroga la Directiva 95/46/CE (Reglamento general de protección de datos), así como en la Ley Orgánica 3/2018, de 5 de diciembre, de Protección de Datos Personales y garantía de los derechos digitales.

La información referente a sus datos y muestras será codificada asignando a cada voluntario un código generado aleatoriamente. Estos datos serán guardados en un fichero de datos protegido en el servidor del Instituto de Microelectrónica de Barcelona (IMB-CNM), cuyo acceso tendrán únicamente los responsables de los servicios informáticos del instituto y el personal investigador implicado en el estudio. El tratamiento de los datos de la investigación tendrá únicamente una finalidad técnica, para comprobar que el dispositivo en desarrollo funciona correctamente en condiciones de sudor real. Sus datos estarán disponibles en el fichero de datos protegido hasta la finalización del proyecto (Enero 2021). Las muestras de sudor, después de ser analizadas con los dos dispositivos de medida, serán descartadas en el contenedor de deshechos biológicos del instituto. La cesión de muestras biológicas será gratuita y voluntaria. Usted no tendrá derecho a participar en los potenciales beneficios que se deriven de la explotación comercial de los resultados de la investigación.

Solamente se le solicitarán aquellos datos estrictamente necesarios para la finalidad propuesta y no está contemplada la cesión a terceros, salvo por imperativo legal.

Usted tiene derecho a solicitar al investigador responsable el acceso a sus datos personales, así como a su rectificación y supresión, a la limitación de su tratamiento, a la portabilidad de los datos, o cualesquiera otros que pudieran corresponderles. Igualmente, se le hace constar la existencia en el CSIC de un Delegado de Protección de Datos, que es D. José López Calvo – Vocal Asesor de Asesoría Jurídica: delegadoprotecciondatos@csic.es; repd@csic.es; jose.lopez.calvo@csic.es

En el caso de que se detecte alguna anomalía en el valor de conductividad del sudor se le comunicará el resultado y se le indicará que acuda a un centro de referencia especializado en la enfermedad. En el caso de la afectación de la Fibrosis Quística, una conductividad equivalente a 60mM NaCl o superior indicaría la posibilidad de padecer la enfermedad, entonces se le indicará que acuda al Parc Taulí Hospital Universitari o al Hospital Vall d'Hebron que poseen una unidad de Fibrosis Quística especializada. No obstante, se respetará su derecho a que no se le comuniquen estos resultados y para ello, tiene la posibilidad de marcar una casilla en el formulario de consentimiento informado adjunto.

VI. PARA MÁS INFORMACIÓN

Usted tiene derecho a clarificar todas las dudas que se le presente en cualquier momento, pudiendo solicitar información más detallada sobre la investigación. Para ello, puede comunicarse con el investigador principal cuyos datos de contacto se relacionan al comienzo de este documento.

Durante el transcurso del reclutamiento de voluntarios existe la posibilidad de quedar excluido de la investigación, ya sea por motivos de seguridad, por cualquier acontecimiento adverso que se produzca y se considere relacionado con su participación en la investigación o porque se considere que no está cumpliendo con los procedimientos establecidos. En cualquiera de los casos, recibirá una explicación adecuada del motivo que ha ocasionado su retirada de la investigación.

Si considera que todas las dudas han sido aclaradas y tiene la convicción de participar en este estudio, a continuación, puede firmar la hoja de consentimiento informado.

MINISTERIO
DE CIENCIA
E INNOVACIÓN

CSIC
CONSEJO SUPERIOR DE INVESTIGACIONES CIENTÍFICAS
COMITÉ DE ÉTICA

HOJA DE CONSENTIMIENTO INFORMADO

TÍTULO DEL PROYECTO:
PROMOTOR/FINANCIADOR:
INVESTIGADOR/ES RESPONSABLE/S:
PERSONA QUE PROPORCIONA LA INFORMACIÓN
Y CONSENTIMIENTO INFORMADO:
PARTICIPANTE:

D/Dª. _____ , con **DNI** _____ y domicilio en _____ .

DECLARO que he leído la Hoja de Información al participante, de la cual se me ha entregado una copia, que he contado con el tiempo suficiente, que se me ha ofrecido la oportunidad de hacer preguntas y que he recibido suficiente información por parte del investigador D/Dª. _____ , quien me ha explicado convenientemente las condiciones de mi participación en esta investigación. Asimismo, se me ha asegurado el tratamiento confidencial de mis datos.

Declaro adicionalmente que comprendo que mi participación es voluntaria, por lo que puedo retirarme de la investigación libremente y revocar mi consentimiento, en cualquier momento y por cualquier razón.

DOY
NO DOY **Mi consentimiento para ser participe en el estudio propuesto**

DOY
NO DOY **Mi consentimiento para incorporar las muestras a una Colección/Biobanco** (si procede)

DOY
☐ **NO DOY** **Mi consentimiento para ser informado de datos concernientes a mi salud o a la de mis familiares**

Firmo por duplicado y guardo una copia:

Fecha y firma del participante.

Fecha y firma del asentimiento del menor (si es de aplicación).

D/Dª _____ , investigador responsable de la obtención de este consentimiento informado, con **DNI** _____ , **DECLARO** que he explicado las características

y alcance de la investigación al participante, atendiendo a sus capacidades, (con especial delicadeza si se trata de población sensible) y le he informado de los potenciales riesgos y beneficios directos derivados de la misma. Quien rubrica este documento fechado otorga voluntariamente su consentimiento o el del menor* para participar en la investigación descrita.

Fecha y firma de la persona responsable de la obtención del consentimiento informado.

*Con carácter general se deberá recoger la firma de ambos progenitores; en caso de que solo pudiera firmar uno, esto deberá ser justificado suficientemente.